

Pattern Formation in Thin One- and Two-layer Liquid Films

Von der Fakultät für Mathematik, Naturwissenschaften und Informatik
der Brandenburgischen Technischen Universität Cottbus

zur Erlangung des akademischen Grades eines
Doktors der Naturwissenschaften (Dr. rer. nat.)

genehmigte Dissertation

vorgelegt von

Diplom-Physiker

ANDRIY POTOTSKYY

geboren am 14.01.1979 in Bishkek (Kirgisien)

Gutachter: Prof. Dr. rer. nat. habil. Michael Bestehorn

Gutachter: Dr. rer. nat. habil. Uwe Thiele

Gutachter: Prof. Alexander Golovin

Tag der mündlichen Prüfung: 07. Dezember 2005

Contents

1	Introduction	5
2	Stokes equation and lubrication approximation	13
3	Intermolecular interaction	21
3.1	Long-range interaction	21
3.2	Short-range interaction	28
4	One-layer liquid films	31
4.1	Evolution equation	31
4.2	Large-scale Marangoni convection	32
4.2.1	Fluid parameters	35
4.2.2	Stationary Solutions: holes, drops and walls	36
4.2.3	Holes or Drops?	40
4.2.4	Normal form of the fully time dependent equation	42
4.2.5	The numerical method	43
4.2.6	The horizontal film	46
4.2.7	The inclined film	48
4.3	Influence of external disturbances	53

4.3.1	Ultrasound	54
4.3.2	Inhomogeneous wetting	60
5	Two-layer liquid films	65
5.1	Coupled evolution equations	65
5.2	The disjoining pressures	69
5.3	General stability of flat films	71
5.4	Long-range interaction only	74
5.4.1	Scaling and flat film stability	74
5.4.2	Flat film stability: one-layer vs. two-layer films	75
5.4.3	Different instability modes	76
5.4.4	Rupture acceleration	79
5.4.5	Two-mode behavior	80
5.4.6	Limiting cases	82
5.5	Long-range and short-range interactions	83
5.5.1	Flat film stability	83
5.5.2	Non-uniform stationary solutions	87
5.5.3	Mode-type transitions	88
5.5.4	Large-period stationary solutions	96
6	Conclusion	99
	References	105
A	Thermocapillary terms in nonisothermal liquid films	119

Chapter 1

Introduction

Instabilities of thin liquid films between a solid substrate and a gas atmosphere have attracted much scientific interest. The main focus lies thereby on front instabilities of moving contact lines [4, 12, 19] or on instabilities of the free liquid-gas interface of a flat film [97, 124, 130]. A recent review can be found in Ref. [80]. To analyze such instabilities a long-wave or lubrication approximation [80, 101, 116] is often used as a very powerful tool especially for low Reynolds number film flows. At present the basic behavior of one-layer films in the physically different thickness ranges is well understood. Several instability mechanisms exist that by means of different driving forces may destabilize an initially flat film. They are described, analyzed and modeled in a large number of experimental [48, 97, 98, 107, 114, 130, 131] and theoretical [3, 9, 27, 70, 80, 81, 103, 104, 110, 111, 112, 120, 123, 126, 127, 133, 135] works. For film thicknesses d less than about 100 nm, effective molecular interactions between the film surface and the substrate dominate all the other forces, like thermo- and soluto-capillarity or gravity, and thus determine the film stability. For heated films of thicknesses above 100 nm, eventually thermocapillary forces become the most important influence leading to an instability caused by large-scale Marangoni convection [9, 130]. It is dominant up to an upper limit of the film thickness determined by the competition between large-scale and small-scale convection modes [42]. For even thicker films with thicknesses above 100 μm also the gravity force be-

comes important. Depending on its direction it may stabilize the large-scale Marangoni instability or destabilize the film further (Rayleigh-Taylor instability) [81, 135]. The lubrication approximation is valid up to a limiting film thickness obtained by the requirement that the wave length of the dominant instability mode λ_m is much larger than the film thickness d , i.e. $\lambda_m \gg d$. For the Rayleigh-Taylor instability λ_m depends on the interfacial tension, the density of the liquid and the gravitational acceleration but not on the film thickness [80]. It is of the order of 10^3 to $10^4 \mu\text{m}$ implying an upper limit for the film thickness of 10^2 to $10^3 \mu\text{m}$. As a preface to the present work we give here a brief description of each of the above mentioned instability mechanisms.

Intermolecular forces. The stability and evolution of liquid films of thicknesses below 100 nm is determined by effective molecular interactions between substrate and film arising, for instance, from Van der Waals, electrostatic or entropic interactions [45, 47]. Such films are linearly unstable if the energy of the intermolecular interaction is a convex function of the film thickness. For film thicknesses above 10 nm the long-range Van der Waals forces dominate. They can be of different nature depending on the molecular properties of the involved media. One distinguishes interactions between two randomly orienting dipoles (orientation interaction), between a randomly orienting dipole and an induced dipole (induction interaction), and between a fluctuating dipole and an induced dipole (dispersion interaction). Between two parallel interfaces at a distance d , all these forces decay as A/d^3 where A is the Hamaker constant [47]. An unstable situation corresponds to a positive Hamaker constant. Note, however that different schools use different sign conventions. The dominant wave length of the instability λ_m increases monotonically with d as $\lambda \sim d^2$ (see Ref. [80]). The stability of a film may change dramatically for a substrate coated with a layer of different dielectric properties as, for instance, a silicon substrate (Si) coated with an silicon oxide layer (SiO) [108]. There, for an oxide layer of about 2 nm only ultrathin polystyrene (PS) films below 4 nm thickness are linearly unstable. Increasing the film thickness in the linearly unstable range, the wave length λ increases rapidly and diverges at the critical thickness d_c . For

$d > d_c$ the film is linearly stable, but may rupture due to finite disturbances.

Marangoni effect. Due to the variation of the surface tension with temperature tangential forces appear if the fluid is heated (cooled) from below. Typically, these forces act stabilizing if the fluid is cooled from below. When heating from below, the stationary conducting state of the fluid becomes unstable if a critical vertical temperature gradient is exceeded. This instability is referred as Marangoni instability. There are two types of Marangoni instability, the long wave and the short wave. While the long wave instability is accompanied by large amplitude deformations of the liquid-gas interface, the short wave instability leads to the appearance of the convection cells under almost flat film surface [5, 6, 8, 43, 87, 115, 119]. A slightly depressed piece of the surface comes closer to the hot bottom plate, heats up and consequently gets a lower surface tension than its surrounding. The resulting surface tension gradient causes a flow away from the depressed piece pulling out even more liquid from this region thereby deepening the depression further. This positive feedback corresponds to an unstable situation.

The evolution in time and space of the instability is often described by a simplified equation for the profile of the free surface. It can be derived from the Stokes equation using the lubrication approximation [80]. For the thin film on a heated horizontal substrate this was done for a linear dependence of surface tension on temperature in Ref. [15]. The effects of a quadratic dependence of surface tension on temperature were studied in Ref. [82] for liquid films on a horizontal substrates and in Ref. [81] on an inclined substrate. In the latter case the evolution equation loses its variational structure allowing for a richer bifurcation structure, as studied recently in some detail in Ref. [122]. All the mentioned work focused on the structure formation in two spatial dimensions, i.e. the object of study is a film thickness profile that depends on one spatial coordinate. Pattern formation in three dimensions, i.e. the evolution of a film thickness profile that depends on two spatial coordinates was studied for a film on the underside of a cooled horizontal plate where now gravitation acts destabilizing and the surface tension gradient acts stabilizing [29]. Corresponding results for a film on top of a heated plate were given in Ref. [78].

Extensive experiments on the long wave surface-tension-driven convection were performed for heated horizontal films below a gas layer of finite thickness [131]. The formation of depressions (dry spots) and elevations were observed depending on the used gas. The evolution equation for the film thickness for the used two-layer geometry was also derived. It has a similar form as the equation for the one-layer system but leads to a different definition of the Biot number.

In a different approach the evolution of a film profile was followed numerically towards rupture using the full Stokes equation in combination with a linear temperature field [11]. Cascades of consecutive “structuring events” pointing towards the formation of a set of drops as the final state of the system were found. Due to a slowing down of the numerical scheme once the minimum film thickness becomes very small the final state of the system could not be reached. However, the qualitative agreement between these results and those obtained from long wave approximation [78] indicates that the main features of the physical system are well captured by this approximation, as already noted for falling liquid films [80, 95].

In the last few years some theoretical and numerical work was dedicated to pattern formation and instabilities of liquid films in three spatial dimensions [7, 31, 78, 79, 112, 113]. Especially [78] deals with films unstable due to the Marangoni effect. There, the temporal evolution was restricted due to rupture which occurred when the thickness of the film achieved unphysical negative values. Therefore no results in the long time limit are known up to now. To examine a fluid film in the long time in three dimensions under a vertical temperature gradient one needs to include a stabilizing effect which is obtained by introducing a disjoining pressure which becomes effective for very small film thickness. This was done in Ref. [9]. Instead of rupture and completely dry domains the solid support is always covered by a thin precursor film of thickness of some 10 nm. The spatio-temporal evolution of the film surface was analyzed when a horizontal force is applied externally [9]. This situation is found when the fluid layer is inclined with respect to the vertical. The formation of periodic structures perpendicular to the slope as well as the instability of fronts moving downwards the inclined plane were

discussed.

External disturbance. The creation of well defined micro- or nanostructured thin films of soft matter attracted much interest over the last years. Unstable films on solid substrates are used in several ways to produce such patterns with defined length scale and structure. (i) One may directly employ the surface instability by choosing the initial film thickness such that the predominant mode gives exactly the wanted length scale. However, the pattern has only a short-range order and the structure cannot be chosen independently but is also determined by the film thickness (holes, drops or labyrinths [7, 9]). The evolution has to be stopped before coarsening sets in, for instance by evaporation [124] or freezing [10].

One can also use a structured substrate forcing the thin film to image it [96, 102]. Contrary to (i) one needs to know the instability length scale only approximately because ideal imaging is possible in a range around it [14, 51].

Desired patterns can also be obtained by manipulating the flow on the microscopic scale. This can be done by means of electrohydrodynamic pumping, electro-osmotic flow, electrowetting, thermocapillary pumping and simultaneous action of shear stress at liquid-gas interface and a variable surface energy pattern at the liquid-solid interface [52].

Two-layer films. By replacing the (solid) coating layer by a liquid layer one transforms the system into a two-layer liquid film. Some of the results obtained for a solid coating can be directly transferred to the new situation. The stability of the (now) upper layer still depends on the (now liquid) coating layer. However, additionally the liquid coating layer itself may be unstable making a re-evaluation of the stability necessary. This gedankenexperiment leads quite naturally to the extension of the well studied one-layer systems to two-layer systems. In general, there exist two possible two-layer geometries. On the one hand the two liquid layers can be situated between two solid plates leaving only the interface between the two liquids free to move. In consequence such a system can be described by a single evolution equation [61, 62, 69]. On the other hand the two layers can be situated between a solid substrate and a gas atmosphere. Then both, the

liquid-liquid and the liquid-gas interface are free to move and their evolution has to be described by coupled evolution equations. Models were derived, for instance, assuming a lower liquid layer that is much thicker than the upper layer [13], and for two-layer systems with surfactants (and non-Newtonian behavior) [21, 67, 137] or including evaporation [23, 24, 86]. A two-layer system under the solely influence of molecular interactions is studied in Ref. [1, 2]. In Ref. [91] a similar system is studied, however, the evolution equations are given in terms of variations of an energy functional.

The experimental interest in two-layer liquid films is up to now mainly focused on the dewetting of a liquid layer from a very thick layer, i.e. a liquid bulk substrate [37, 57, 72, 84, 134]. In contrast Ref. [99] studies the dewetting of a polystyrene (PS) layer of 15 to 68 nm thickness from a 46 nm thick polyamide (PA) layer. The substrate is a silicon (Si) wafer covered with a layer of native oxide. At high temperature (195°C) and small thicknesses (15...35 nm) the PS layer is unstable and dewets exhibiting typical spinodal patterns. At low temperature (115°C) the PA layer is solid resulting in a stable PS layer, independent of its thickness.

Ref. [66] studies relatively thick layers (100 nm to 1 μ m thickness) of poly(dimethylsiloxane) (PDMS) layers on a liquid substrate of fluorinated PDMS. They show that the PDMS films are metastable and may dewet by nucleation of holes. The velocity of the growth of holes depends on the viscosity and thickness of the substrate. In another system (PS layer on poly(methylmethacrylate) (PMMA) layer, both with thicknesses of about 100 nm) the dewetting velocity was found to exhibit a minimum as a function of the viscosity of the lower layer [57]. Furthermore, for a polycarbonate (PC) layer on a poly(styrene-*co*-acrylonitrile) (SAN) layer Ref. [84] reports a non-trivial dependence of the dewetting velocity on both layer thicknesses.

Starting from the Stokes equation in each layer and using appropriate boundary conditions, the coupled evolution equations for two-layer liquid films were derived in Ref. [91]. If only the long-range Van der Waals interactions are included one can study different pathways of dewetting towards rupture but can not describe the long-time evolution of such films as, for instance,

necessary for the description of the above mentioned experiments. To prevent the film rupture the simultaneous action of the short-range stabilizing and the long-range destabilizing interactions is important. The derivation of the system of evolution equations for a general interaction energy and a non-isothermal situation was done in Ref. [92]. Thereby the main focus lies on ultrathin layers with respective thicknesses below 100 nm for which the effective molecular interactions between the four media are the dominant influence.

The present work is structured as follows. The introductory part starts with the historical overview of the basic hydrodynamic equations and continues with the derivation of the one-layer thin film equation in the lubrication approximation (Chapter 2). The detailed analysis of the long-range as well as short-range intermolecular interactions is given in Chapter 3. The main part of the work is divided into two large sections. Chapter 4 is devoted to one-layer films and Chapter 5 presents the analysis of the time evolution of two-layer films.

In Chapter 4 we first discuss the 3D large-scale Marangoni convection in one-layer films with stabilizing long-range interaction. Linear stability analysis, nonlinear stationary solutions, as well as 3D time dependent numerical solutions in plane and inclined layers are presented. In the second part of Chapter 4 the influence of an external disturbance on the time evolution of one-layer films is investigated. In the case of a non-contact method, an external disturbance can be used to move a single drop, front or hole in a certain direction [93]. The principle is illustrated by incorporating a sonic disturbance in a thin film equation to study the evolution of ultrathin films unstable due to their wetting properties. The second method is based on inhomogeneous templating of the substrate. Here we study the influence of periodic modulation on coarsening in the long time limit. Finally, the fully nonlinear evolution of a 3D system is presented by numerical integration.

Chapter 5 begins with the derivation of the long wave evolution equations for a two-layer film in the general non-isothermal case allowing also for slip at the substrate [92]. Focusing on the isothermal case without slip

these equations are analyzed and integrated numerically in the subsequent sections. Concluding remarks on both one-layer and two-layer films are presented in Chapter 6.

Finally, the expressions for the surface tension gradients in terms of gradients of the layer thicknesses are discussed in the Appendix.

Chapter 2

Stokes equation and lubrication approximation

The laws of liquid motion have attracted the interest of scientists for many centuries. Already NEWTON [75] and later PLATEAU [89] investigated the static properties of soap films. Probably the most prominent and earliest result on the dynamics of liquids is the equation by EULER [36]

$$\rho [\partial_t \mathbf{v} + (\mathbf{v} \nabla) \mathbf{v}] = -\nabla p, \quad (2.1)$$

where \mathbf{v} , ρ and p denote the velocity field, density and pressure of the liquid, respectively. Although NEWTON and BERNOULLI considered isolated problems involving fluids, it was EULER who laid down the foundations of hydrodynamics through a systematic investigation of its basic equations. Hence it is only appropriate that the inviscid equation of motion is named after Euler often regarded as the originator of modern hydrodynamics. Later NAVIER (1822) and STOKES (1842) modified Euler's equation to describe the motion of viscous fluids

$$\rho [\partial_t \mathbf{v} + (\mathbf{v} \nabla) \mathbf{v}] = -\nabla p + \nu \Delta \mathbf{v}, \quad (2.2)$$

where ν denotes the dynamic viscosity of the liquid. Since that time the Navier-Stokes equation is the basic governing equation which is used to solve both theoretical and purely engineering problems of fluid dynamics, aeronautics.

Unfortunately, the solutions of the full Navier-Stokes equation are numerically expensive. The convection term $(\mathbf{v}\nabla)\mathbf{v}$ and the dissipation term $\nu\Delta\mathbf{v}$ make the equations highly nonlinear of the second order in space. Analytical solutions are possible only for few special cases of simple geometry [58].

This enhanced in the beginning of the last century the development of different simplifications of the Navier-Stokes equation. Such simplifications (approximations) are valid for certain flow regimes. Thus, fluid friction, i.e. the interaction between the molecules of the liquid, can be neglected if the dynamic effects prevail. In this case (also called inviscid or ideal flows) the Navier-Stokes equations Eq. (2.2) reduce to the Euler ones Eq. (2.1). Strictly speaking, inviscid flows are those for which the Reynolds number $Re = \rho UL/\nu$ is large. Here U is a measure of the flow speed and L is a measure of the length scales associated with the velocity gradients in the flow or with the geometry of the flow. To ensure the consistency and solvability of the inviscid flow equations, one also has to ignore the no-slip and heat flux boundary conditions. The ideal flows solution obtained with such boundary conditions failed to predict phenomena such as drag or the onset of vorticity.

It was PRANDTL [94] who justified the use of the ideal flow approximation and combined it with the viscous flows equation. He noted that, far away from a solid wall, viscous interactions are not significant in determining the flow field. However, in a thin region near a solid boundary, the viscous interactions has a significant effect on fluid motion. Prandtl's idea of a boundary layer, a thin region near a surface where all of the viscous effects reside, made tractable the flow calculations that take viscosity into account. This led to yet another approximation of the Navier-Stokes equation Eq. (2.2), known as the boundary layer equations [94].

The opposite case to the ideal flows is the Stokes approximation. It is valid only for small Reynolds numbers, when the viscous friction plays a significant role

$$\nabla(p + \phi) = \nu\Delta\mathbf{v}. \quad (2.3)$$

Here ϕ stands for the volume density of the potential of the external bulk

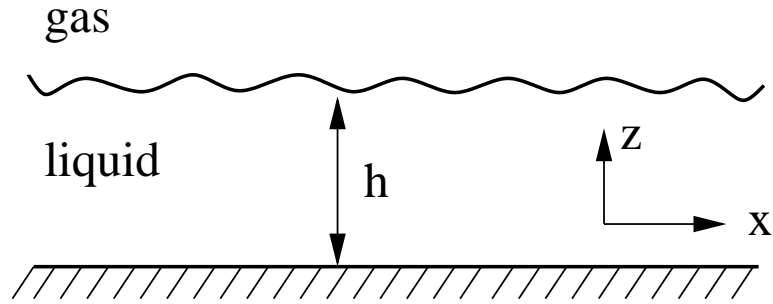


Figure 2.1: *Sketch of the problem in two dimensions. The local film thickness is h . In the non-evaporating case the volume of the liquid does not change with time, i.e. $\int h dx = \text{const}$.*

forces. In the present thesis the Stokes equation Eq. (2.3) together with the continuity equation for incompressible liquids ($\text{div } \mathbf{v} = 0$) are the starting point for all calculations. In the following we consider the time evolution of a thin liquid film on a solid support with free liquid-gas interface, as shown in Fig. 2.1. The flows within thin liquid films are slow due to the no-slip condition at the substrate. The horizontal component of the velocity field can not increase significantly within the length scale given by the film thickness. This is true only if not taking into account slopes with large inclinations or considering strong external shear stresses.

To proceed we also need boundary conditions at the free liquid-gas interface of the film. These are the kinematic condition and the boundary condition for the liquid stress tensor

$$w = \partial_t h + u \partial_x h, \quad \mathbf{T} \cdot \mathbf{n} = -k \sigma \mathbf{n} + \frac{\partial \sigma}{\partial s} \mathbf{t} + \mathbf{f}, \quad (2.4)$$

respectively. Here w and u are the vertical and horizontal components of the velocity field, respectively, and h is the local film thickness. \mathbf{T} is the stress tensor of the liquid, \mathbf{n} is the unit outward vector normal to the interface, \mathbf{t} is the unit vector tangential to the interface, σ is the surface tension, \mathbf{f} is the prescribed forcing at the interface, whose normal and tangential components are p_0 and $\boldsymbol{\tau}$, respectively, k is the local curvature of the interface, and s is

the arc length along the interface, such that

$$\mathbf{n} = \frac{(-\partial_x h, 1)}{(1 + (\partial_x h)^2)^{1/2}}, \quad \mathbf{t} = \frac{(1, \partial_x h)}{(1 + (\partial_x h)^2)^{1/2}}, \quad k = \frac{\partial_x^2 h}{(1 + (\partial_x h)^2)^{3/2}}. \quad (2.5)$$

At the substrate we use the Navier slip condition

$$w = 0, \quad u - \beta \partial_z u = 0, \quad (2.6)$$

where the slip length β is assumed to be small.

The issue of free interfaces is a big problem in fluid dynamics. Even considering the low Reynolds number flows, when the linear Stokes equation Eq. (2.3) is applicable, one has to incorporate the boundary conditions Eq. (2.4) to obtain a closed system of equations for \mathbf{v} and h . This free interface problem can be handled only numerically. Analytical results are possible only for small deviations of the film thickness from a mean value [42, 74, 73].

Fortunately, for a special class of problems one can use a lubrication (or long-wave) approximation (REYNOLDS 1883 [100]) to further simplify the Stokes equations Eq. (2.3) and the boundary conditions Eq. (2.4). The lubrication approximation accounts only for those disturbances of the film thickness whose lateral wave length λ is much larger than the mean film thickness d . Thus, the appropriate dimensionless parameter $\epsilon = d/\lambda \ll 1$ is used to introduce the scaling of the lubrication approximation [80]. The vertical and the horizontal coordinates and velocities are scaled as

$$Z = \frac{z}{d}, \quad X = \frac{\epsilon x}{d} \quad \text{and} \quad W = \frac{w}{\epsilon U_0}, \quad U = \frac{u}{U_0}, \quad (2.7)$$

respectively. Here U_0 is the characteristic velocity of the problem. The dimensionless time, stresses, normal component of the liquid stress tensor and the density of the potential of the bulk forces are

$$T = \frac{\epsilon U_0}{d} t, \quad S = \frac{d}{\nu U_0} \tau, \quad P_0 = \frac{\epsilon d}{\nu U_0} p_0, \quad \Phi = \frac{\epsilon d}{\nu U_0} \phi. \quad (2.8)$$

Using these scales we nondimensionalize the Stokes equations Eq. (2.3) and obtain to leading order in the lubrication parameter ϵ

$$\partial_Z^2 U = \partial_X P + \partial_X \Phi, \quad \partial_Z (P + \Phi) = 0. \quad (2.9)$$

As it can be extracted from Eq. (2.4), the surface tension terms are measured by $C^{-1}\epsilon^3$, where $C = U_0\nu/\sigma$ denotes the capillary number. It will turn out to be essential to retain surface tension effects at leading order, so that one takes $C^{-1}\epsilon^3 = \bar{C}^{-1}$ to be of order one. Hence, the boundary conditions Eq. (2.6) and Eq. (2.4) read

$$U - \beta_0(\partial_Z U) = 0, \quad (Z = 0), \quad (2.10)$$

and

$$\begin{aligned} \partial_Z U &= S + \partial_X \Sigma, \\ -P_0 - P &= \bar{C}^{-1} \partial_X^2 H, \quad (Z = H), \end{aligned} \quad (2.11)$$

respectively. Here $\beta_0 = \beta/d$ is the dimensionless slip coefficient, $\Sigma = \epsilon\sigma/\nu U_0$ is the dimensionless surface tension, H is the scaled film thickness and P_0 is the dimensionless pressure in the gas layer.

The first equation in Eq. (2.9) can now be integrated to yield the velocity profile $U(Z)$

$$U(Z) = \partial_X(P + \Phi) \frac{Z^2}{2} + KZ + B, \quad (2.12)$$

where the integration parameters K and B depend only on X . Using the boundary conditions Eq. (2.10) and Eq. (2.11) they are specified to $B = \beta_0 K$, $K = S + \partial_X \Sigma - H \partial_X(P + \Phi)$.

Integrating the equation Eq. (2.12) again over Z we obtain the stream function $\Psi(Z, X)$ which is defined by $\partial_X \Psi = -W$, $\partial_Z \Psi = U$. With the help of the stream function the kinematic condition in Eq. (2.4) can be written as

$$\partial_T H + \partial_X[\Psi(H)] = 0, \quad (2.13)$$

which is the evolution equation of the local film thickness $H(X, T)$.

Finally, using the second equation in Eq. (2.11) to determine the pressure P

and scaling back to the dimensional variables, the equation Eq. (2.13) reads

$$\begin{aligned} \nu \partial_t h - \partial_x \left[\left(\frac{h^3}{3} + \beta h^2 \right) \partial_x (\phi(h) - \sigma \partial_x^2 h - p_0) \right] \\ + \partial_x \left[(\tau + \partial_x \sigma) \left(\frac{h^2}{2} + \beta h \right) \right] = 0. \end{aligned} \quad (2.14)$$

This is the most general film thickness evolution equation which accounts for the bulk forces (ϕ), for the thermo(solut)ocapillarity ($\partial_x \sigma$) and for external stresses (τ). As we already mentioned in Section 1, if the film thickness is in the range of 100 nm, the intermolecular forces become important. The action of these forces on the evolution of a liquid film can be modeled by specifically choosing the potential ϕ in Eq. (2.14). In this case the function ϕ is referred to as the “disjoining pressure”. Further on we will denote the disjoining pressure by Π . It enters the thin film equation Eq. (2.14) with the sign, opposite to that of the Laplace term $\sigma \partial_x^2 h$. Depending on the interaction type, the disjoining pressure can stabilize or destabilize the flat film.

To find out what condition the disjoining pressure Π should satisfy to destabilize (stabilize) a flat film, we linearize the evolution equation Eq. (2.14) around $h = h_0$ with h_0 representing the mean film thickness. For simplicity we put $\tau = \partial_x \sigma = 0$ and introduce a small disturbance of the film thickness $\delta h \sim \exp(\gamma t + ikx)$, where γ is the growth rate of the disturbance and k is its wave number. In the first order in δh we have

$$\gamma = \frac{1}{\nu} \left(\frac{h_0^3}{3} + \beta h_0^2 \right) (-\sigma k^4 - \partial_h \Pi(h_0) k^2). \quad (2.15)$$

Dispersion relation Eq. (2.15) represents the so-called type- II_s instability [22] when $\partial_h \Pi(h_0) < 0$. Thus $\Pi(h)$ acts destabilizing if $\partial_h \Pi(h_0) < 0$ and stabilizing if $\partial_h \Pi(h_0) > 0$.

Heat equation. To study the non-isothermal liquid films one needs to couple the temperature field ζ to the evolution of the local film thickness h . The temperature equation read

$$\rho c (\partial_t \zeta + (\mathbf{v} \nabla) \zeta) = \kappa_{th} \Delta \zeta, \quad (2.16)$$

where c is the specific heat of the fluid and κ_{th} is its thermal conductivity. At the free liquid-gas interface the continuity of the heat flux has to be imposed

$$\kappa_{th} \nabla \zeta \cdot \mathbf{n} = \kappa_g \nabla \zeta_g \cdot \mathbf{n}. \quad (2.17)$$

Here κ_g and ζ_g denote the thermal conductivity and the temperature in the gas layer. In the zeroth order of the lubrication parameter the heat equation and the heat flux equation become

$$\begin{aligned} \Delta \zeta &= 0 \\ \kappa_{th} \partial_z \zeta &= \kappa_g \partial_z \zeta_g. \end{aligned} \quad (2.18)$$

The last equations are used to derive the surface temperature $\zeta(h)$ in the case of one- and two-layer liquid films. This is done in the Appendix.

In the next section we specify the potential Π for long-range apolar and short-range polar interaction.

Chapter 3

Intermolecular interaction

3.1 Long-range interaction

Intermolecular interaction plays a decisive role in the stability and time evolution of liquid films with film thicknesses of 100 nm or less. As a matter of fact, the energy of interaction between the molecules of the ambient gas layer and those of the substrate across the liquid layer E_{int} changes the total spreading coefficient S which is the energy difference between the solid substrate with the contacting gas and liquid phases $S = E_{\text{sg}} - E_{\text{sl}} - E_{\text{lg}}$. If E_{int} may not be neglected, it should be added to S . In the thin film community (see for instance [54, 110, 111]) the constant part $E_{\text{sg}} - E_{\text{sl}} - E_{\text{lg}}$ of the spreading coefficient S is omitted and the latter is given only by E_{int} . In this Chapter we describe in detail the interaction term E_{int} which is often divided into polar and non-polar parts. The non-polar part is associated with the long-range interaction whereas the polar part with the short-range one.

Consider two parallel interfaces which separate different media as shown in Fig. (3.1). The interaction between single molecules of the media (1) and (4) leads to an effective force which acts on the interfaces (1 – 2) and (3 – 4). The value of this force per unit area, as well as its dependence on the distance between the interfaces D depends in a crucial way on the type of

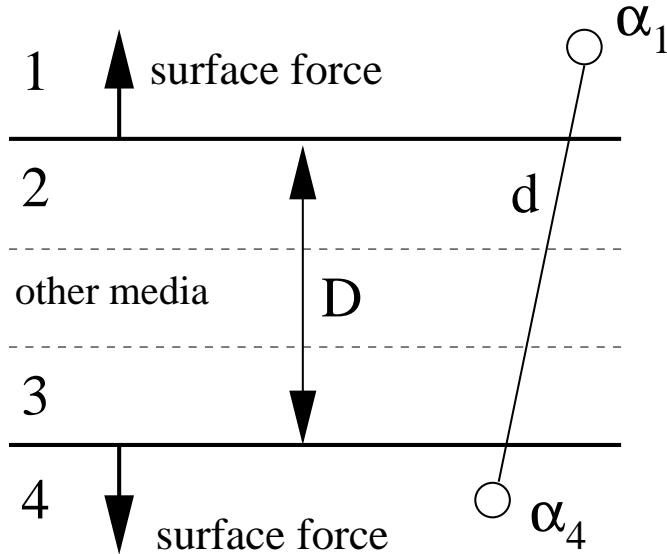


Figure 3.1: Two parallel interfaces (1–2) and (3–4) a distance D apart, separating media with different dielectric properties. Two atoms with polarizabilities α_1 and α_4 a distance d apart are shown schematically.

the molecules the media are made of. Moreover, even for the media with determined molecular properties, the effective surface force can change its functional dependence on D , when going to extremely small distances between the interfaces. This is similar to the Lenard-Jones potential, where the long-range term $1/d^6$ prevails for large distances d between the molecules, whereas the short-range term $1/d^{12}$ becomes important for distances comparable to the molecular size.

To derive the functional dependence of the surface force on D we start with the interaction energy between single molecules, which depends on the charge as well as on the dipole moment of the molecules. Speaking only about simple homogeneous liquids, two important facts can be recalled to simplify further the problem. First, the molecules of homogeneous liquids are not charged and can be either polar or neutral. And second, the molecules are not bounded in the liquids by any bonding force (hydrogen bonding, lattice bonding) and thus can freely rotate around their symmetry axis. This allows to exclude the charge-charge and the charge-induced dipole inter-

actions from the discussion and concentrate on interactions which include permanent freely rotating dipoles and neutral molecules. Thus only three possibilities remain:

- rotating dipole-dipole interaction (KEESOM [53])
- rotating dipole- induced dipole interaction (DEBYE [28])
- fluctuating dipole- induced dipole interaction (LONDON [63])

Interestingly, the interaction energy between two molecules decays as $1/d^6$ with distance d between the molecules for all three interaction types. The corresponding forces are usually referred to as long-range in contrast to short-range forces which decay exponentially with d (see Section 3.2).

The mechanism of the fluctuating interaction was first proposed by London in 1920. According to London, the charge density of the electrons in the non-polar molecules admits fast temporal fluctuations, resulting in a time dependent dipole moment. The fluctuating dipoles polarize the neighboring non-polar molecules, leading to dipole-dipole interaction. If the distance between the molecules becomes larger, the retardation effects lead to $1/d^7$ dependence of the interaction energy.

More precisely, the non-retarded dispersion energy of two molecules at distance d embedded in a medium with dielectric constant ϵ (see Fig. 3.1) is given by the McLachlan's formula [68]

$$U = -\frac{3\hbar}{\pi d^6} \int_0^\infty \frac{\alpha_1(i\xi)\alpha_4(i\xi)}{\epsilon^2(i\xi)} d\xi, \quad (3.1)$$

where $\alpha_1(i\xi)$ and $\alpha_4(i\xi)$ are the polarizabilities of the atoms as functions of the imaginary frequency. The retarded interaction energy reads

$$U = -\frac{23\hbar c}{4\pi d^7} \frac{\alpha_1(0)\alpha_4(0)}{\epsilon^{5/2}(0)}. \quad (3.2)$$

Note that the existence of the dispersive force between two interfaces which separate different media resembles the well known Casimir effect (CASIMIR, 1948 [18]), when two parallel conducting plates in vacuum experience an attractive force. The attractive force is explained by vacuum fluctuations

of the electromagnetic field which are confined in the gap between the conducting plates. Only the frequencies (gap resonances) are allowed for which the integer multiples of half a wavelength can fit exactly the gap length D . Thus, the total energy of the system per unit area depends on D . It turns out that the energy decreases with decreasing gap distance D , leading to an attractive force between the conducting plates.

The fluctuating interaction is the most universal one, because it exists between polar as well as between non-polar molecules. Beside this, the fluctuating part of the total force is the only significant term in polar condensed media [83]. This is the main reason for taking into account only dispersive force to explain the stability of thin liquid films.

Now we sketch the derivation of the dispersive interaction energy between two parallel interfaces, separated by an arbitrary number of media (see Fig. 3.1). There exist two alternative approaches which both lead to the same result. Historically the first approach was proposed by Lifshitz in 1955 [60]. His main idea was to incorporate the fast temporal fluctuations of the electromagnetic field in the Maxwell equations. The boundary conditions at the interfaces reduce the number of allowed frequencies. The dispersive force per unit area is then obtained by integration of the Fourier transform of the normal component of Maxwell's stress tensor over all allowed frequencies. For non-retarded potential, the resulting surface force (disjoining pressure) is given by

$$\Pi = \frac{A}{6\pi D^3}, \quad (3.3)$$

where A is the Hamaker constant which depends, in general, in a complex way on the dielectric properties of the media.

Using the equation Eq. (2.15) of Chapter 2 and equation Eq. (3.3) we conclude that the positive sign of A corresponds to the attraction (destabilizing effect), whereas the negative sign of A corresponds to the repulsion (stabilizing effect). We note here that there is no common convention about the sign of the Hamaker constant. To describe attraction between the interfaces some schools use positive sign of A , whereas other schools use negative sign of A and a different definition of the disjoining pressure: ($\Pi \rightarrow -\Pi$).

Later, Dzyaloshinskii, Lifshitz and Pitaevskii showed that Lifshitz's formula can also be derived in the frame of quantum electrodynamics [35].

The second approach for calculating the dispersive force was proposed by Israelachvili in 1972 [46]. This approach is often referred to as method of images. In the rest of this section we will focus on the method of images due to its transparency as compared to Lifshitz approach.

The functional dependence of the surface force on the distance D between the interfaces is obtained by simply integrating the force between single molecules, whose potential is given by Eq. (3.1) (or by Eq. (3.2) for retarded forces), over the half spaces (1) and (4). Such space integration is validated due to Hamaker (1937), who showed the additivity of the dispersive forces and developed the theory of London-Van der Waals interaction between macroscopic bodies.

First, we consider a one-layer case, when the media (2) and (3) are equal and there are no other media in between. The integration of Eq. (3.1) yields the non-retarded force per unit area

$$f = \frac{\hbar N_1 N_4}{2D^3} \int_0^\infty \frac{\alpha_1(i\xi)\alpha_4(i\xi)}{\epsilon^2(i\xi)} d\xi, \quad (3.4)$$

where N_1 and N_4 are the number of atoms per unit volume in medium (1) and (4), respectively.

The main goal of the method of images is to calculate the volume excess polarizabilities $N_i\alpha_i(i\xi)$ of each medium. Fig. 3.2 shows schematically the process of the reflexion of the initial electric field E from the interfaces (1–2) and (2–4). From the elementary course of electrodynamics it is known that after the reflexion from the interface ($i-k$) into the medium k , the reflected field E' is proportional to the incoming field E with the reflexion coefficient $\Delta_{ik} = (\epsilon_i - \epsilon_k)/(\epsilon_i + \epsilon_k)$. The image field is due to the surface charge density σ_s , or excess volume polarization $P_i = N_i\alpha_i E$ in medium i . The latter is given by

$$P_i = \frac{\epsilon_k}{2\pi} \left(\frac{\epsilon_i - \epsilon_k}{\epsilon_i + \epsilon_k} \right) E. \quad (3.5)$$

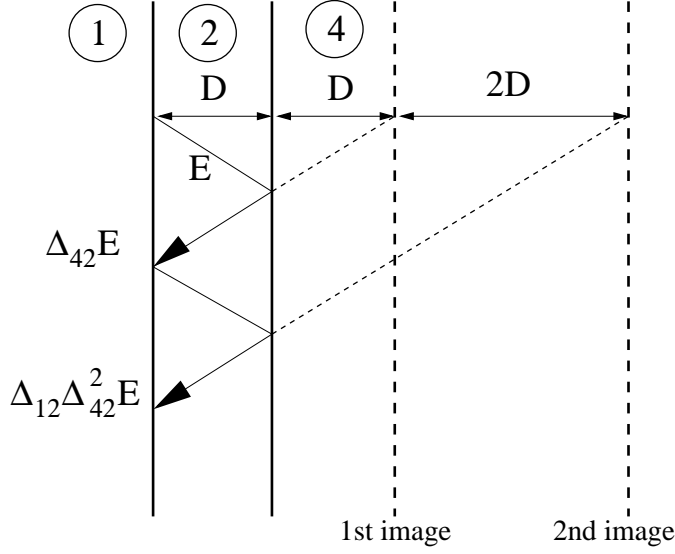


Figure 3.2: One-layer system: reflexions of the electric field in the gap between the interfaces (1 – 2) and (2 – 4).

Comparing the last two equations one finds the volume excess polarizability of the first image of the interface (1 – 2) after the reflexion off (2 – 4)

$$(N_4\alpha_4)_1 = \frac{\epsilon_2}{2\pi} \left(\frac{\epsilon_4 - \epsilon_2}{\epsilon_4 + \epsilon_2} \right). \quad (3.6)$$

The second image of the interface (1 – 2) a distance $4D$ apart from (1 – 2) acts as if there were a real surface at half that distance $2D$ (see Fig. 3.2) for which the volume excess polarizability is $(N_4\alpha_4)_2 = [\epsilon_2/(2\pi)]\Delta_{42}^2\Delta_{12}$. Further reflexion give rise to an infinite series for the total dispersive force

$$f = \frac{\hbar}{8\pi^2 D^3} \int_0^\infty \sum_{n=1}^\infty \frac{1}{n^3} \left(\frac{\epsilon_1 - \epsilon_2}{\epsilon_1 + \epsilon_2} \right)^n \left(\frac{\epsilon_4 - \epsilon_2}{\epsilon_4 + \epsilon_2} \right)^n d\xi. \quad (3.7)$$

Comparing Eq. (3.7) with $f = A/(6\pi D^3)$, one finds for the Hamaker constant

$$A = \frac{3\hbar}{4\pi} \int_0^\infty \sum_{n=1}^\infty \frac{1}{n^3} \left(\frac{\epsilon_1 - \epsilon_2}{\epsilon_1 + \epsilon_2} \right)^n \left(\frac{\epsilon_4 - \epsilon_2}{\epsilon_4 + \epsilon_2} \right)^n d\xi. \quad (3.8)$$

The last equation is not applicable for practical purposes because of its complexity. Indeed, to perform the integration in Eq. (3.8), one needs to

know for each medium the total spectrum $\epsilon_i(i\xi)$. Experimental data on $\epsilon_i(i\xi)$ are available only for a narrow interval of frequencies and typically show a peak at a resonant frequency. This allows to treat all the media as composed of oscillators with only one resonant (absorption) frequency. Thus, following [46], we write the expression for the dielectric constant ϵ_i with one absorption frequency ω_i

$$\epsilon_i(i\xi) = 1 + \frac{\omega_i^2(\epsilon_i(0) - 1)}{\omega_i^2 + \xi^2}. \quad (3.9)$$

It is also known that many dielectrics absorb strongly at about the same frequency in the ultra violet region around 100 nm. Hence, the absorption frequencies of all the media can be put to be equal $\nu_e = 3 \times 10^{15}$ Hz.

To further simplify Eq. (3.8), we neglect the multiple reflexions of the electric field in the gap between the interfaces (1 – 2) and (2 – 4). This is justified because the reflexion coefficients $\Delta_{ik} = (\epsilon_i - \epsilon_k)/(\epsilon_i + \epsilon_k)$ are always less than one.

With all these simplifications we perform the integration in Eq. (3.8) and obtain the one-layer Hamaker constant

$$A_{124} = \frac{3h\nu_e}{8\sqrt{2}} \frac{(n_1^2 - n_2^2)(n_4^2 - n_2^2)}{(n_1^2 + n_2^2)^{1/2}(n_4^2 + n_2^2)^{1/2}[(n_1^2 + n_2^2)^{1/2} + (n_2^2 + n_4^2)^{1/2}]}. \quad (3.10)$$

From now on we will denote by A_{ijk} the Hamaker constant which describes the interaction between the half spaces i and k through the medium j . In the last equation we replaced the dielectric constants ϵ_i of the medium i by the corresponding refractive index $n_i = \epsilon_i^2$.

In an analogous way, neglecting the multiple reflexions, one can derive the four-indices Hamaker constant A_{1234} which describes the interaction between the interfaces (1 – 2) and (3 – 4) (see Fig. 3.1). The integration yields

$$A_{1234} = \frac{3h\nu_e}{8\sqrt{2}} \frac{(n_1^2 - n_2^2)(n_4^2 - n_3^2)}{(n_1^2 + n_2^2)^{1/2}(n_4^2 + n_3^2)^{1/2}[(n_1^2 + n_2^2)^{1/2} + (n_3^2 + n_4^2)^{1/2}]}. \quad (3.11)$$

Note that Eq. (3.11) coincides with the result obtained in [76] in the frame of the Lifshitz theory.

The three-indices Hamaker constant A_{ijk} can be obtained from the four-indices constant A_{ijkl} by putting $j = l$. This corresponds to the fact that the media j and l have the same optical properties.

As we see, in the second order of the reflexion coefficients Δ_{ik} , the Hamaker constant A_{1234} depends only on reflexions at the interfaces (1–2) and (3–4) and does not depend on dielectric properties of the media which are located between the media 2 and 3 (see Fig. 3.1). There also exists an alternative approach that accounts for the dielectric properties of all the media lying in-between the interfaces (1–2) and (3–4) [41]. This approach is described in [38]. According to [38], the four-index Hamaker constant is given by a linear combination of the products $\Delta_{ij}\Delta_{kl}$. Each such a product corresponds to the reflexion between some pair of interfaces which are located between (1–2) and (3–4).

3.2 Short-range interaction

The short-range forces which can be of an electrostatic or structural nature [27, 118] decay exponentially with h . The electrostatic part Π_e results from the formation of diffuse electric double-layers in the vicinity of interfaces involving polar liquids [30, 77, 132]. The potential of such double-layers is given by the Poisson-Boltzmann equation. In the frame of the Gouy-Chapman-Theory one derives the characteristic decay length $1/\kappa$ (Debye length) of the double-layer potential [20] with

$$\kappa = \sqrt{\frac{8\pi e^2 n_0}{\epsilon k T}}. \quad (3.12)$$

In the previous equation k is the Boltzmann constant, T the absolute temperature, e the unit charge, ϵ the dielectric constant of the liquid and n_0 the volume ion concentration.

For large film thicknesses there exist two independent double-layers at the two interfaces. For small film thicknesses these two double-layers overlap resulting in an effective force between the interfaces. This force can in general be attractive or repulsive. In the symmetrical case of two identical

interfaces and small interfacial potentials ψ_s , or for $h \gg 1/\kappa$ the disjoining pressure reads

$$\Pi_e = -kTn_0 \left[4 \tanh \left(\frac{e\psi_s}{4kT} \right) \right]^2 \exp(-\kappa h) \quad (3.13)$$

$\partial_h \Pi_e$ is always positive and according to Eq. (2.15) the disjoining pressure Π_e acts stabilizing. For different interfacial potentials ψ_1 and ψ_2 the resulting force can be either attractive or repulsive [118, 45].

The structural part of the total force Π_s consists of all the influences of the molecular structure which can not be explained by the concept of the diffuse double-layers. These are the sterical and entropic interactions and hydration forces [85, 118].

The evidence of these forces was provided for apolar liquids with film thicknesses up to 10-15 molecular layers. In water films, however, the structural effects can be seen in films with thicknesses up to 80 nm.

In the present work we will not distinguish between the electrostatic and the structural part of the disjoining pressure. Referring to the short-range forces we will assume that they decay exponentially with the film thickness. The corresponding interaction energy between the interfaces (1-2) and (3-4) is proportional to $\exp[(l_0 - D)/l]$, where $l_0 = 0.158$ nm is the Born repulsion length, and $l = 1/\kappa \sim 1.10$ nm is the interaction length of the short-range interactions.

Chapter 4

One-layer liquid films

4.1 Evolution equation

As shown in previous Chapters, the spatiotemporal behavior of a one-layer film of incompressible liquid with a free surface on a solid smooth substrate without slippage is described by an evolution equation for the film thickness $h(x, y, t)$

$$\nu \partial_t h = -\nabla \left[\frac{h^3}{3} \nabla (\sigma \Delta h - \partial_h f(h) - P_0) - \frac{h^2}{2} \partial_x \sigma \right]. \quad (4.1)$$

Here, $\partial_h f(h)$ denotes the disjoining pressure with the potential $f(h)$. ν and σ are the dynamic viscosity and surface tension of the liquid, respectively. The Laplace pressure is given by $\sigma \Delta h$, P_0 is the gas pressure at the surface (normally assumed to be constant).

For small surface deformation and near the critical point, the free energy $f(h)$ may be expanded with respect to h in the sense of Landau. Then, Eq.(4.1) has the same form as the Cahn-Hilliard equation describing the decomposition of a binary mixture [17, 16]. It corresponds to the simplest possible equation for the dynamics of a conserved order parameter field [59]. The choice of the free energy $f(h)$ and of the Marangoni term $\partial_x \sigma$ determine the particular physical system under consideration. It can be dewetting due to effective molecular interactions between film and substrate. Then $\partial_h f$ accounts for the wetting properties of the system [7, 79, 103, 112, 120, 127].

Or it may describe a long wave Marangoni instability. Then $\partial_x \sigma$ has to be expressed in terms of the local film thickness and its gradient [81, 122, 131]. For inclusion of other effects see the review Ref. [80].

In this chapter we describe the liquid films driven by large-scale Marangoni convection (Section 4.2) and ultra thin films under the influence of an external disturbance (Section 4.3).

4.2 Large-scale Marangoni convection

In the past years many theoretical and numerical work was dedicated to pattern formation and instabilities of liquid films. The commonly used description is based on the hydrodynamic equations with appropriate boundary conditions. We assume a liquid film with thickness d , viscosity ν , density ρ , thermal diffusivity κ , and heat conductivity α . On its free upper surface it is in contact with the ambient air having the heat conductivity α_a and thickness d_a . In zero order of the lubrication approximation, the surface temperature is coupled to the local film thickness $h(x, y, t)$ (see Eq.(2.18) and the Appendix). Tangential surface stresses comes into play if the surface tension Γ is assumed to be proportional to the surface temperature T_s :

$$\Gamma = \gamma_0 - \gamma(T_s - T_0)$$

where T_0 acts as a reference temperature. The non-dimensionalized evolution equation describing the height of the film then reads

$$\partial_t h = \nabla \cdot \left\{ h^3 \nabla (B_o h + \partial_h f(h) - \Delta h) - \frac{3}{2} h^2 \frac{CM(B+1)}{(1+Bh)^2} \nabla h \right\} \quad (4.2)$$

where

$$M = \frac{\gamma \Delta T d}{\rho \nu \kappa}, \quad B = \frac{d \alpha_a}{d_a \alpha}, \quad C = \frac{\rho \nu \kappa}{\gamma_0 d}, \quad B_o = \frac{g \rho d^2}{\gamma_0}$$

denote the Marangoni number, the Biot number, the Chrispation number, and the static Bond number respectively. We adopted the scaling of [79], where h and x, y is in units of d and time scales with $3\rho\nu d/\gamma_0$. The temperature ΔT is defined as the difference between the temperature at the bottom

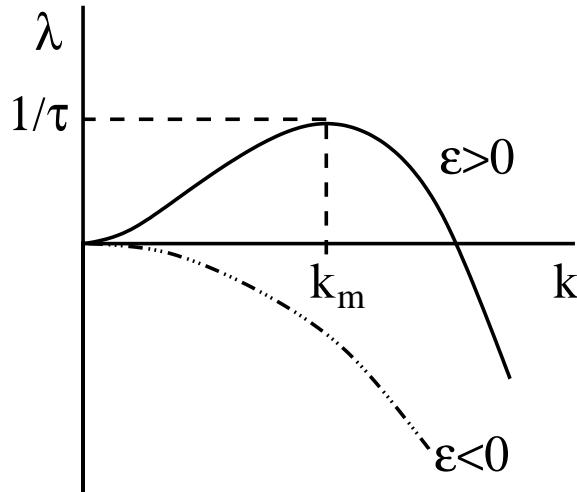


Figure 4.1: Sketch of the linear growth rate $\lambda = \varepsilon k^2 - k^4$ in the case of a type- II_s instability. The solid line is above threshold, and dotted-dashed below. Above threshold patterns with the typical length scale $\ell = 2\pi/k_m = 2\pi/\sqrt{\varepsilon/2}$ grow in the linear stage on the time scale $\tau = 4/\varepsilon^2$.

and that of the free film surface in the non-convective case. In Eq. (4.2) the disjoining pressure is taken into account by the general potential $f(h)$. A linear stability analysis of the flat film is performed by giving a small amplitude perturbation $\eta \exp(\lambda t + ikx)$ to the flat film surface and linearizing the evolution equation Eq. (4.2) with respect to the amplitude of the perturbation η . This gives the relation between the growth rate λ and the wave number k (see Fig. 4.1). Linear stability analysis for films without disjoining pressure ($f = 0$) shows that it gets unstable if M exceeds a certain critical value

$$M_c = \frac{2}{3} \frac{B_o}{C} (1 + B) = \frac{2}{3} G (1 + B) \quad (4.3)$$

where $G = B_o/C$ is the Galileo number. If M exceeds M_c , a so-called type- II_s [22] instability occurs (Fig. 4.1) and on the linear (short time) regime one expects patterns with the typical length scale

$$\ell = 2\pi/\sqrt{\varepsilon B_o} \quad (4.4)$$

where ε is defined as the reduced distance from threshold

$$\varepsilon = (M - M_c)/M_c \quad (4.5)$$

water 60 ⁰ C		silicone oil 50cS, 25 ⁰ C		
$\rho = 983 \text{Kg/m}^3, \nu = 4.7 \cdot 10^{-7} \text{m}^2/\text{s}, \kappa = 1.6 \cdot 10^{-7} \text{m}^2/\text{s}$		$\rho = 960 \text{Kg/m}^3, \nu = 5 \cdot 10^{-5} \text{m}^2/\text{s}, \kappa = 10^{-7} \text{m}^2/\text{s}$		
$\gamma_0 = 6.6 \cdot 10^{-2} \text{N/m}, \gamma = 1.74 \cdot 10^{-4} \text{N/mK}$		$\gamma_0 = 2.08 \cdot 10^{-2} \text{N/m}, \gamma = 6.8 \cdot 10^{-5} \text{N/mK}$		
	$d = 10^{-3} \text{m}$	$d = 10^{-6} \text{m}$	$d = 10^{-3} \text{m}$	$d = 10^{-6} \text{m}$
ΔT_c	37 ⁰ C	$4.3 \cdot 10^{-5} \text{ }^0\text{C}$	92 ⁰ C	$1.07 \cdot 10^{-4} \text{ }^0\text{C}$
M_c	86970	$1.01 \cdot 10^{-4}$	1308	$1.53 \cdot 10^{-6}$
B_o	0.146	$1.46 \cdot 10^{-7}$	0.453	$4.53 \cdot 10^{-7}$
C	$1.12 \cdot 10^{-6}$	$1.12 \cdot 10^{-3}$	$2.31 \cdot 10^{-4}$	0.23
A	$8.0 \cdot 10^{-15}$	$8.0 \cdot 10^{-9}$	$2.6 \cdot 10^{-14}$	$2.6 \cdot 10^{-8}$
A/B_o	$5.5 \cdot 10^{-14}$	$5.5 \cdot 10^{-2}$	$5.6 \cdot 10^{-14}$	$5.6 \cdot 10^{-2}$
$\ell \cdot d$	$1.6 \cdot 10^{-2} \text{m}$	$1.64 \cdot 10^{-2} \text{m}$	$9.3 \cdot 10^{-3} \text{m}$	$9.3 \cdot 10^{-3} \text{m}$
$h_c^b \cdot d$	$5.5 \cdot 10^{-8} \text{m}$	$7.1 \cdot 10^{-7} \text{m}$	$5.5 \cdot 10^{-8} \text{m}$	$7.3 \cdot 10^{-7} \text{m}$

Table 4.1: *Used values of the adimensional parameters.*

Previous work shows that above the onset of the instability holes are formed and film rupture occurs after a finite evolution time [79]. Thereby rupture is defined by the occurrence of zero film thickness values. Then equation Eq. (4.2) is no longer applicable.

However, the possible stationary two-dimensional solutions of equation Eq. (4.2) with $f = 0$ can be determined directly [81] independently of the fact that they cannot be reached from the initial condition of a flat film by integration in time. The stationary solutions consist of a vast family of drop solutions separated by dry regions of different lengths. All of these solutions are nominally linearly stable since drops separated by dry regions do not interact if no non-hydrodynamic interaction is included. In the formulation without disjoining pressure the solutions with zero microscopic contact angle are energetically favored. However, the inclusion of a disjoining pressure would select a certain contact angle and remove the degeneracy as discussed in [81].

Now we extend the evolution equation by a disjoining pressure that is of repelling character. It therefore stabilizes a very thin film and avoids the film rupture that restricted the simulations in time to investigations of the

short-time behavior. With this extended model we are able to study pattern formation in three dimensions in the long-time limit.

If Van der Waals forces are responsible for the stabilization, the disjoining pressure $\partial_h f(h)$ has the form

$$\partial_h f(h) = -\frac{A}{h^3} \quad (4.6)$$

where A is a dimensionless positive constant which is related to the three index Hamaker constant A_{slg} (see Chapter 3) in the scaling used here by

$$A = -\frac{A_{slg}}{6\pi\gamma_0 d^2} \quad (4.7)$$

With Eq. (4.6) the range of unstable flat films is also bounded from below, i.e. flat films with the height $h = 1$ are unstable if

$$h_c^b \leq 1 \leq h_c^t \quad (4.8)$$

The two values h_c^b and h_c^t are named *spinodals*. For thick films in the range of mm, one finds the scaling $h_c^b \propto d^{-1/3}$. The values of h_c^b are very small in the size of $10^{-7} \dots 10^{-8}$ m (see Tab. 4.1). Approximately flat parts of the film profile which have a thickness in the stable region below h_c^b can be considered as a precursor film. This means that even in regions where dry spots occur the solid support is still covered by this thin precursor film with the height in the range of some 10 to 100 nm.

We note that the inclusion of the disjoining pressure changes the value for M_c to

$$M_c = \frac{2}{3} \frac{B_o}{C} + 2 \frac{A}{C} \quad (4.9)$$

Here we approximated $(1+B)^2$ and $(1+B)$ by 1, which is good for small Biot number, *i.e.* for thermally almost insulating upper boundary. We shall use this approximation for the rest of the Chapter.

4.2.1 Fluid parameters

To compare with the experiments we show in Table 4.1 the values of the adimensional parameters introduced above as well as those of some important properties of the fluid film. To demonstrate also the dependence on

the film thickness, we chose the four cases water and silicone oil, each with layer thicknesses of 1mm and 1 μ m. For the Hamaker constant we took the value $A_{slg} = 10^{-20} J$ from [117]. The typical length scale ℓd is computed from Eq. (4.4) for $\varepsilon = 1$. It is remarkable that for thin films the Marangoni number as well as the applied temperature gradients seem to be very small. This means in real experiments one would usually exceed the critical point by a factor of some thousands. However, in a film of 1mm depth, the value of M_c in silicone oil is already much larger than that for small scale convection (about 80..100). Consequently to obtain a pure surface instability without small convective cells (hexagons) the liquid depth should be below 1 mm. We note that in the case of a fluid depth where both instabilities may occur, pattern formation is expected to be much more involved and the small scale structure cannot longer be eliminated using the lubrication approximation. In this case the full system including Navier-Stokes as well as heat equation has to be considered. A detailed linear analysis was done in Ref. [42].

4.2.2 Stationary Solutions: holes, drops and walls

In the case of stationary solutions equation Eq. (4.2) can be integrated twice which yields

$$\frac{1}{B_o} \Delta h = -d_h V(h) - \mu \quad (4.10)$$

with

$$V(h) = -\frac{1}{2}h^2 - \frac{\alpha}{6} \frac{1}{h^2} + (1 + \varepsilon)(1 + \alpha)h(\ln h - 1) \quad (4.11)$$

beyond the small bifurcation parameter ε defined in Eq. (4.5) we have introduced the reduced Hamaker constant α

$$\alpha = \frac{3A}{B_o}$$

which enters the equation as the only parameter that depends on the material. The integration constant μ is fixed by the mean value of dV/dh which follows from Eq. (4.10) by integration over the spatial domain S (periodic lateral b.c.)

$$\mu = -\frac{1}{S} \int_S dx dy \frac{dV(h)}{dh}$$

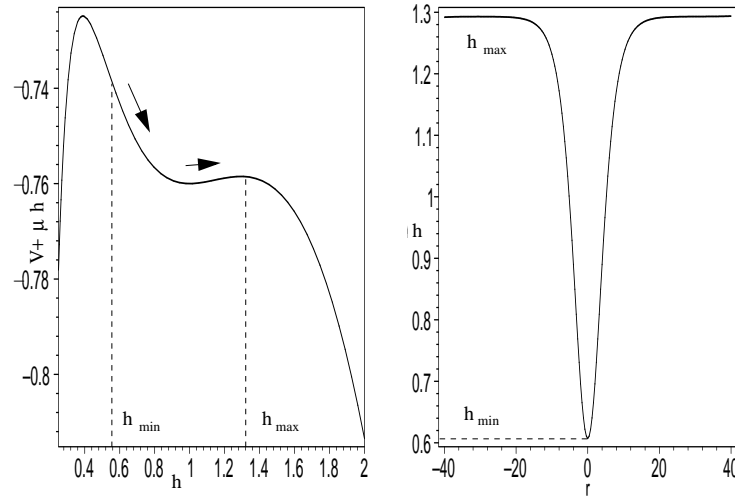


Figure 4.2: *Hole solution in the case of radial symmetry. The effective energy $V(h) + \mu h$ is shown on the left image. The hole solution corresponds to the classical motion of a particle in the potential: trajectory starts at point $r = 0$ with the height $h(r = 0) = h_{\min}$, this is between the left maxima and the minima of the effective energy. The height of the film increases monotonically to the value corresponding to the right maxima of the effective energy. The period of such a solution is infinitely large.*

In the 2D-case the similar problem was studied extensively in the case of dewetting [127].

There the disjoining pressure contributes to both, the destabilizing long-range and the stabilizing short-range components [126, 127], whereas here they are given by the Marangoni effect and the stabilizing disjoining pressure, respectively. The 3D-case is, however, qualitatively different from the two-dimensional one. First, it is not so simple any more to solve Eq. (4.10) by reducing it to an ordinary differential equation. Second, even if we have found some numerical solutions, we still can not say anything about all the other solutions, since the function space in 3D is much more complicated than in 2D. Such numerical solutions were found by Oron for the Rayleigh-Taylor instability of a thin film on the heated substrate without disjoining pressure [81].

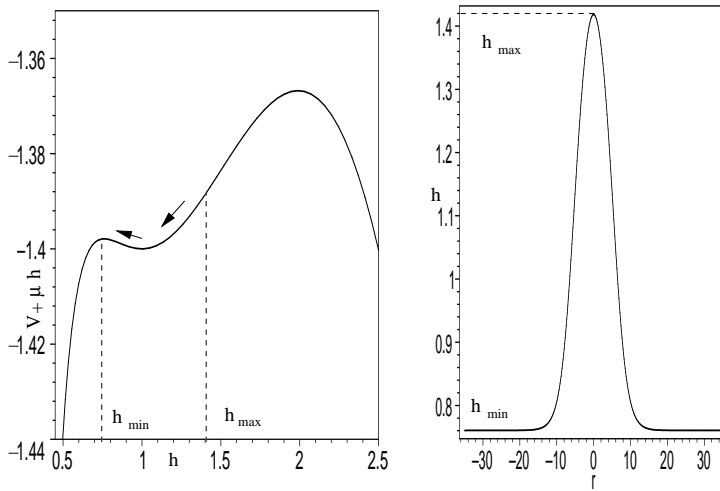


Figure 4.3: *Drop solution.* As in Fig. 4.2, the curve starts at $r = 0$ between the right maxima and the minima of the effective energy. The height of the film decreases monotonically to the left maxima.

In this section we wish to focus on radial symmetric solutions reducing again the spatial dimension by one and state conditions where the types known from the 2D computations may occur. To obtain an effective one-dimensional equation we use polar coordinates in Eq. (4.10). For such radial-symmetrical function $h(r)$ we have the following equation (see also the discussion in [29]):

$$\frac{d^2 h}{dr^2} + \frac{1}{r} \frac{dh}{dr} = -d_h V(h) - \mu \quad (4.12)$$

In the 2D-case it was possible to rewrite Eq. (4.10) in the “energy-conservation” form [126, 122]:

$$\frac{1}{2} \left(\frac{dh}{dx} \right)^2 + V(h) + \mu(h - h_0) = E \quad (4.13)$$

Using the formal equivalence of this equation to the equation of motion for a particle in a potential V , when seeing x as time one could find all main features of stationary solutions by studying the effective potential energy $V(h) + \mu h$. Equation Eq. (4.12), however, contains an additional term that

explicitly depends on r . This leads to the fact that the “energy” is no longer conserved along the “trajectory”. Equation Eq. (4.12) may describe some mechanical system with “time”-dependent friction $\frac{1}{r} \frac{dh}{dr}$. It is still possible to analyze the behavior of such a “mechanical” system by studying its effective energy. The function $V(h) + \mu h$ with V given as Eq. (4.11) is shown on the left images of Figs. (4.2 -4.3) for different values of μ . In all cases this function has two maxima and one minima, but on Fig. 4.2 the left maxima is higher than the right one, on Fig. 4.3 the left one is lower than the right one. Further we are looking for the solutions of Eq. (4.12)

with the initial condition: $(\frac{dh}{dr})_{r=0} = 0$. Each value of $h(r)$ corresponds to a point on the effective energy. The real film profile is given by the motion of such a point along the curve $V(h) + \mu h$. If equation Eq. (4.12) describes a mechanical system with “time”- dependent friction, we can say the following about possible stationary states:

In the wide range of initial height of the film between the binodals (see Fig. 4.4) $h_{min} < h(0) < h_{max}$ there exist damped periodical or even unbounded solutions, that obviously have no physical meaning. However, if rotational symmetry is broken the damped oscillations in r may be associated with satellite holes observed for dewetting in [50]. But among such solutions, there exist three solutions with infinitely large period. These are similar to the drop- hole- and wall-solutions from [70, 126, 129].

1). Hole-solution: the initial height is somewhere between the left maximum and the minimum of the effective energy (see Fig. 4.2), the “mechanical” system starts to move to the right along the curve of effective energy, passes the minimum with the highest “velocity” $\frac{dh}{dr}$, and continues to the right maximum $h = h_{max}$. This process takes an infinitely long “time” $r \rightarrow \infty$. In order to proof that we linearize $d_h V(h)$ at $h = h_{max}$. Since $-d_h V(h = h_{max}) - \mu = 0$ and since $-d_{hh} V(h = h_{max}) > 0$, we have instead of Eq. (4.12):

$$\frac{d^2 h}{dr^2} + \frac{1}{r} \frac{dh}{dr} - \omega^2 (h - h_{max}) = 0 \quad (4.14)$$

here is $\omega^2 = -d_{hh} V(h = h_{max})$.

The solution of the last equation is the first Bessel function ($m = 0$): $h(r) = h_{max} - K_0(\omega r)$. Since K_0 has the property: $\lim_{r \rightarrow \infty} K_0(r) = 0$, it is clear

that only for $r \rightarrow \infty$ the hole-solution reaches h_{max} .

2) Drop-solution: the initial height is somewhere between the right maximum and the minimum (Fig. 4.3). This case is similar to the hole-solution. The only difference is that $h(r)$ decreases monotonically to h_{min} . The proof that drop-solution has infinitely large period is similar to the case of hole-solution.

3) Wall-solution: the values of two maxima of the effective energy are equal (not shown). The initial height of the film is $h = h_{min}$. Let the motion start at the left maximum. But now it takes infinitely long to leave the initial point and the “damping” plays no role for this type of motion. For $r = \infty$ the height h passes through the minimum of the effective energy, and continues to the right maximum. The film profile in this case is similar to the hole-profile, with the difference that the size of the hole is now infinitely large. This corresponds to a zero curvature of the whole, i.e. a plane front.

4.2.3 Holes or Drops?

For the experiment as well as for the numerical solutions of the next paragraph it is important to know whether drops or holes are formed in the unstable range of the flat film $\varepsilon > 0$. Assuming that the flat film has the height $h_0 = 1$ this can depend only on the values of ε and α . Fig. 4.4 shows plots of the pressure $d_h V(h)$ for several values of these parameters. If $h_0 = 1$ lies on the left-hand-side of the Maxwell point $h = h_c$, drops are energetically preferred, in the other case holes are expected. The condition that $h_0 = 1$ coincides with the Maxwell point allows to compute α as a function of ε , as done in Fig. 4.5. From that figure it is clear that for small values of the reduced Hamaker constant holes should be observed. But it is interesting that for $\alpha > 1/3$ only drops are the possible structures. Since $\alpha \propto d^{-4}$ this means that on very thin films always drops evolve, whereas on thicker ones the pattern at onset consists of holes but turns to drops for larger temperature gradients far from threshold. From this calculations one would expect drops even in rather thick films, but farther from threshold as a kind of secondary instability. However, the depth of the precursor film

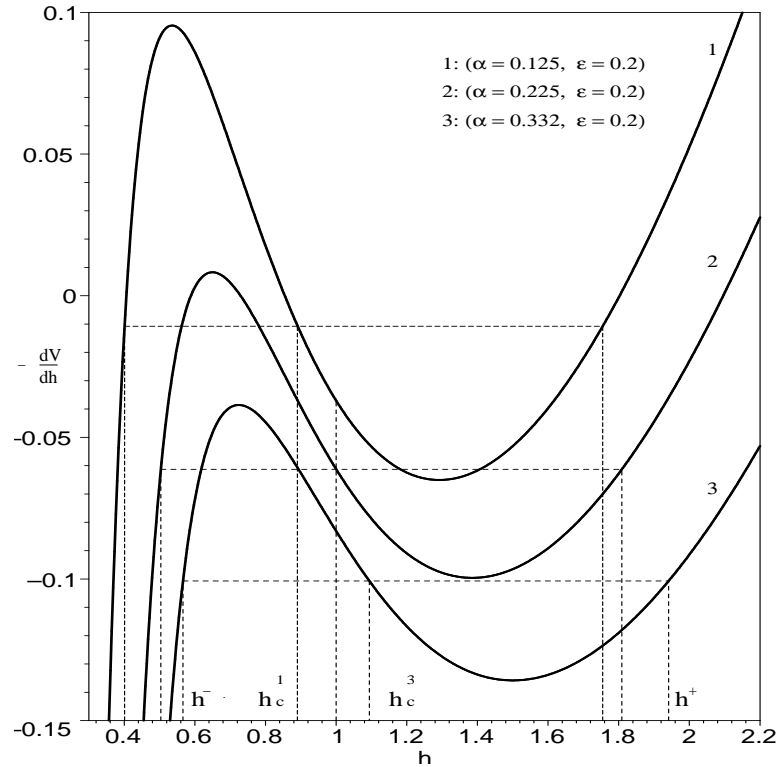


Figure 4.4: The disjoining pressure $d_h V(h)$ according to Eq. (4.11) for different values of α and $\varepsilon = 0.2$. The critical film depth h_c is obtained by a Maxwell-equal-area construction for each potential. If $h_c < 1$ (thick film) holes are energetically preferred, otherwise drops will be formed in the nonlinear stage. Between the two extrema (the spinodals) the film is absolutely unstable, between h^- and h^+ (the binodals) it is bistable.

may decrease to unphysically small values if the thickness of the flat film is very large. In this region the validity of Eq. (4.2) seems not longer justified and one cannot say from the present theory if rupture evolves or not. But even for a thick film with $d = 1\text{mm}$ we compute the height of the precursor film to 10nm. We finally note that drops, or at least one big drop on a rather thick film was found in the experiment by Van Hook et al for an air layer, instead of holes for an helium gas layer above the silicone film. The thermal properties of the gas layer influences the Biot number and also the Marangoni number. It seems possible that the Helium experiment was performed closer to threshold than the one with the air layer. According to

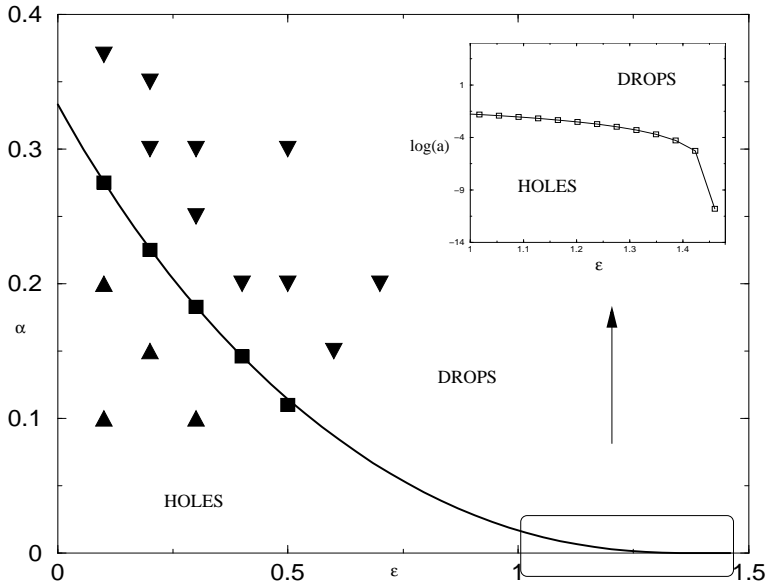


Figure 4.5: *Phase diagram in the parameter plane. The codimension-one line results from the condition $h_c = h_0$ (cf. Fig. 4.4 and text). Solving the fully time dependent Eq. (4.15) numerically, one obtains mazes (squares), holes (up-triangles) and drops (down-triangles) in excellent agreement with the theory. The inset shows that there is a finite $\varepsilon \approx 1.47$ above which drops mathematically exist even at $\alpha = 0$.*

Fig. 4.5 this would explain the patterns observed.

4.2.4 Normal form of the fully time dependent equation

To obtain numerical results in three dimensions, we first transform Eq. (4.2) into a more convenient form. Introducing the reduced control parameter ε according to Eq. (4.5) and after rescaling of space and time variables, it takes the form

$$\partial_t u = -\varepsilon \Delta u - \Delta^2 u + \nabla \cdot [f(u, \Delta) \nabla u] \quad (4.15)$$

here,

$$u(x, y, t) = h(x, y, t) - 1$$

is the normalized, shifted height with vanishing mean value and space and time are scaled to (the primes are omitted in Eq. (4.15))

$$x = x'(B_o + 3A)^{-1/2}, \quad t = t'h_0^3(B_o + 3A)^{-2}$$

in Eq. (4.15), $f(u, \Delta)$ stands for the operator function

$$f(u, \Delta) = \frac{1}{1 + \alpha} \left[(1 + u)^3 - 1 - \frac{\alpha u}{1 + u} \right] - (1 + \varepsilon) [(1 + u)^2 - 1] - \frac{[(1 + u)^3 - 1] \Delta}{(1 + u)^3 - 1} \quad (4.16)$$

which vanishes with u . Note that this form contains only one material parameter, namely α . Eq. (4.15) can be considered as a kind of normal form for pattern formation, at least its linear part. The dispersion relation shown in Fig. 4.1 is obvious, the linearly fastest growing mode has the wave vector $k_m = \sqrt{\varepsilon/2}$ and grows with the typical rate $\tau = 4/\varepsilon^2$. The nonlinear part (as well as the linear one) has the form of the divergence of a flux and clearly conserves the mean value of u to zero. We note in passing that the lowest order truncation $O(\varepsilon^3)$ of Eq. (4.15) reads

$$\partial_t u = -\varepsilon \Delta u - \Delta^2 u + \nabla(u \nabla u) \quad (4.17)$$

and coincides with the lowest order truncation of the Knobloch equation [55].

4.2.5 The numerical method

To solve Eq. (4.15) numerically, it is of advantage to use a semi-implicit time integration scheme. The linear parts of Eq. (4.15) are therefore taken at the new time step $t + \delta t$, the nonlinearities at t . This allows for a much larger time step than a fully explicit method. Approximation of the time derivative by the first order differential quotient leads to the relation

$$\left[\frac{1}{\delta t} + \varepsilon \Delta + \Delta^2 \right] u(t + \delta t) = \frac{1}{\delta t} u(t) + \nabla(f \nabla u(t)) \quad (4.18)$$

To solve for $u(t + \delta t)$ one has to invert the linear differential operator in square brackets on the left hand side of Eq. (4.18). Assuming periodic lateral boundary conditions in real space, this can be done best in Fourier space:

$$\tilde{u}_k(t + \delta t) = \left[\frac{1}{\delta t} - \varepsilon k^2 + k^4 \right]^{-1} \tilde{\Phi}_k(t) \quad (4.19)$$

where \tilde{u}_k denotes the Fourier transform of u and $\tilde{\Phi}_k$ that of

$$\Phi(t) = \frac{1}{\delta t} u(t) + \nabla(f \nabla u(t)) \quad (4.20)$$

To avoid singularities, the expression in the square bracket in Eq. (4.19) must be positive for all k , yielding an upper bound of the time step

$$\delta t_{\max} = 4/\varepsilon^2$$

which is rather big since ε is usually in the order of 0.1. We note that numerical stability is already lost for much smaller time steps than δt_{\max} due to the explicit terms on the right hand side of Eq. (4.18). In our runs following in the next paragraph we usually fix the time step in the region $0.1 < \delta t < 1$. The numerical scheme must fulfill the conservation of the mean height, i.e.

$$\int dx dy u(t) = 0$$

must hold for all times. In Fourier space this is equivalent to

$$\tilde{u}_0(t) = 0$$

which is fulfilled for all time steps if $\tilde{\Phi}_0 = 0$. From Eq. (4.20) it follows that

$$\int dx dy \nabla(f \nabla u(t)) = 0, \quad (4.21)$$

which is obvious for periodic boundary conditions. Numerically, the validity of Eq. (4.21) may depend on the way how the derivatives of u in real space are computed. We use a centered space finite difference method which clearly satisfies Eq. (4.21). This ensures us conservation of $\int dx dy u(t)$ up to the numerical precision which is of order 10^{-8} .

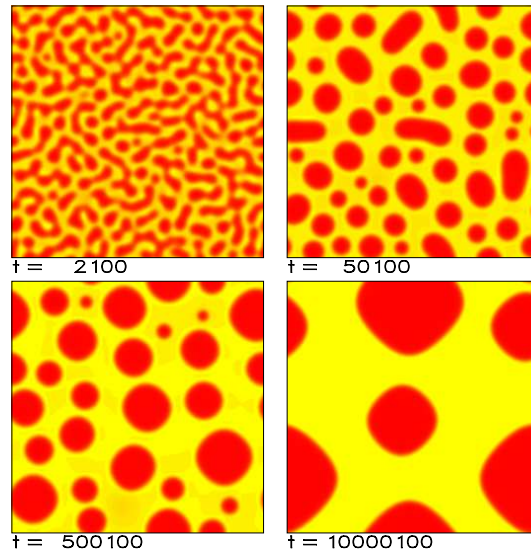


Figure 4.6: *Time series found by numerical integration of Eq. (4.15) in the drop regime $\varepsilon = 0.1$, $\alpha = 0.35$. The numerical resolution is 256×256 mesh points. Dark regions correspond to an elevated surface. Periodic boundary conditions are assumed in the lateral directions.*

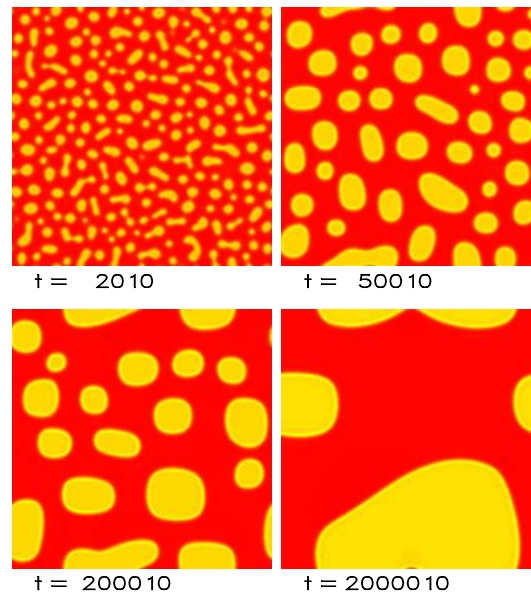


Figure 4.7: *Time series in the hole regime $\varepsilon = 0.1$, $\alpha = 0.05$.*

To show the temporal evolution of the film we present runs for several parameter values in the $\varepsilon - \alpha$ plane. We take the large aspect ratio 500 in units of Eq. (4.15), what corresponds to about 0.5m for the silicon oil of Table 4.1. This, of course is a very large value, expressing the huge scale of the structure, which is due to the small supercriticality of $\varepsilon = 0.1$. Starting with a relatively large value of $\alpha = 0.35$ (rather thin film) drops are expected even at onset. This can be seen in the evolution of Fig. 4.6 where a cascade of larger and larger drops is found. We note that the evolution time is extremely large, also a consequence of the small supercriticality (see also the remarks in Section 4.2.1).

Next we use a smaller value $\alpha = 0.05$, corresponding to a thicker film. Holes are formed now from the beginning (Fig. 4.7). As can also be seen a rim is formed along the border of each hole. The long time behavior can be compared with that of drops. Eventually all drops have merged to a single one. However, again this process may take a very long time, depending on the several fluid parameters and the geometry of the layer.

4.2.6 The horizontal film

To examine the temporal behavior, we compute the mean value of the wave vector according to

$$\langle k \rangle = - \frac{\int d^2k |u_k| |\mathbf{k}|}{\int d^2k |u_k|}$$

From Fig. 4.8 a scaling law of the form

$$\langle k \rangle = ct^{-\beta} \tag{4.22}$$

can be clearly extracted. It is remarkable that the exponent for both series is almost the same. We found it to be $\beta \approx 0.21$

Finally, we present a parameter pair directly on the critical line of Fig. 4.5. As expected, the decision between drops and holes is not clear and a kind of maze structure remains for long times (Fig. 4.9). But also these mazes show the typical dynamics to longer and longer horizontal scales with the same exponent $\beta \approx 0.21$ as shown in Fig. 4.10.

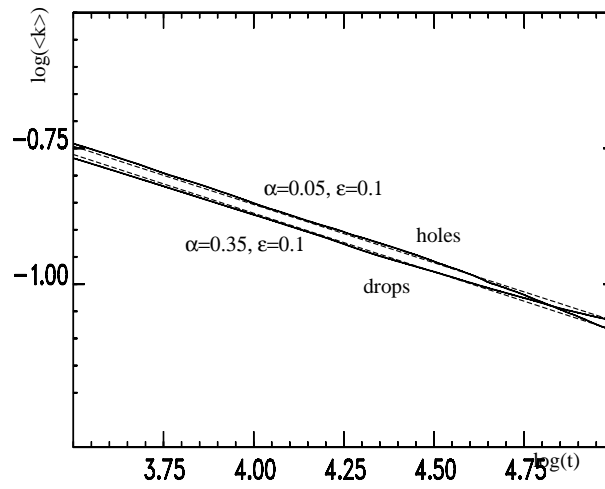


Figure 4.8: The solid lines show the typical scaling of the mean modulus of the wave vector in the temporal evolution for parameters as in Figs. 4.6,4.7. The scaling exponent for both series is the same, $\beta \approx 0.21$ as indicated by the dashed lines. For this computation, we used twice the system size of Figs. 4.6,4.7, and a numerical resolution of 512×512 points.

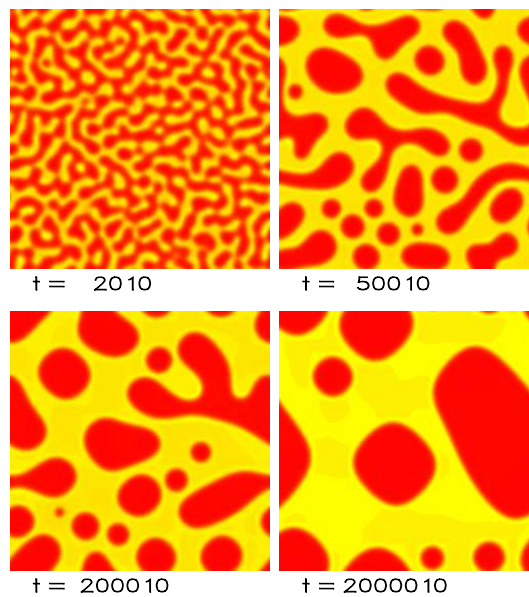


Figure 4.9: Time series in the maze regime at the codimension-one line of Fig. 4.5, $\varepsilon = 0.1$, $\alpha = 0.28$.

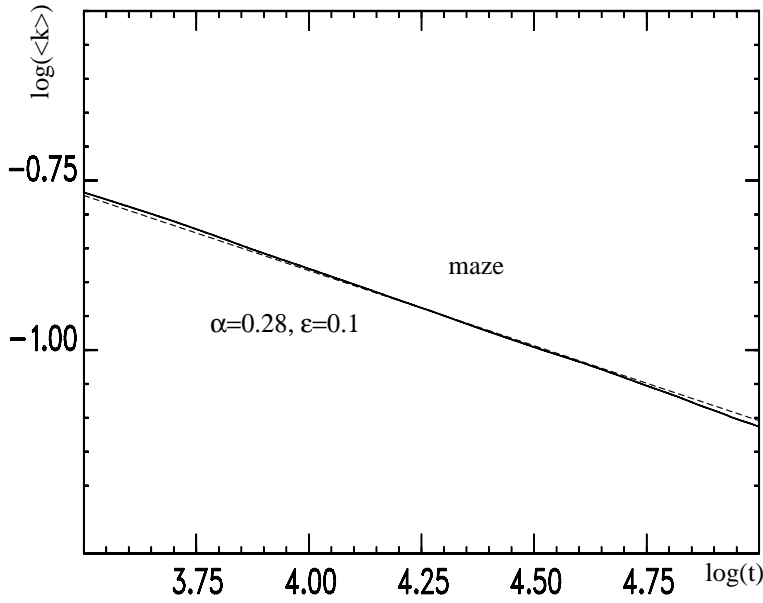


Figure 4.10: *Dynamical scaling of the maze pattern Fig. 4.9. The scaling exponent is again, $\beta \approx 0.21$ (dashed line).*

4.2.7 The inclined film

In this section, we study the influence of a constant external force in a certain horizontal direction. This can be either due to an inclination of the layer by an angle φ , or to an additional horizontal temperature gradient. Here, we shall concentrate on the first case. A constant body force gives an additional term of the form (small $\varphi \approx \sin \varphi$)

$$B_o \varphi \mathbf{n} \cdot \nabla (h^3)$$

on the right hand side of Eq. (4.2). Here, \mathbf{n} is the direction of inclination.

The inclination even by a very small angle φ changes pattern morphology in the long time limit completely. This is shown in Fig. 4.11 where all parameters are equal to that of Fig. 4.6 but the plane was inclined by an angle of order 0.1° (for a silicone film of thickness 1 mm). In the beginning both evolutions seem to be similar but after $t \approx 100.000$ in the inclined film coarsening is retarded and finally a certain wave length is stabilized. The stripes orientate more and more along the direction of inclination, forming

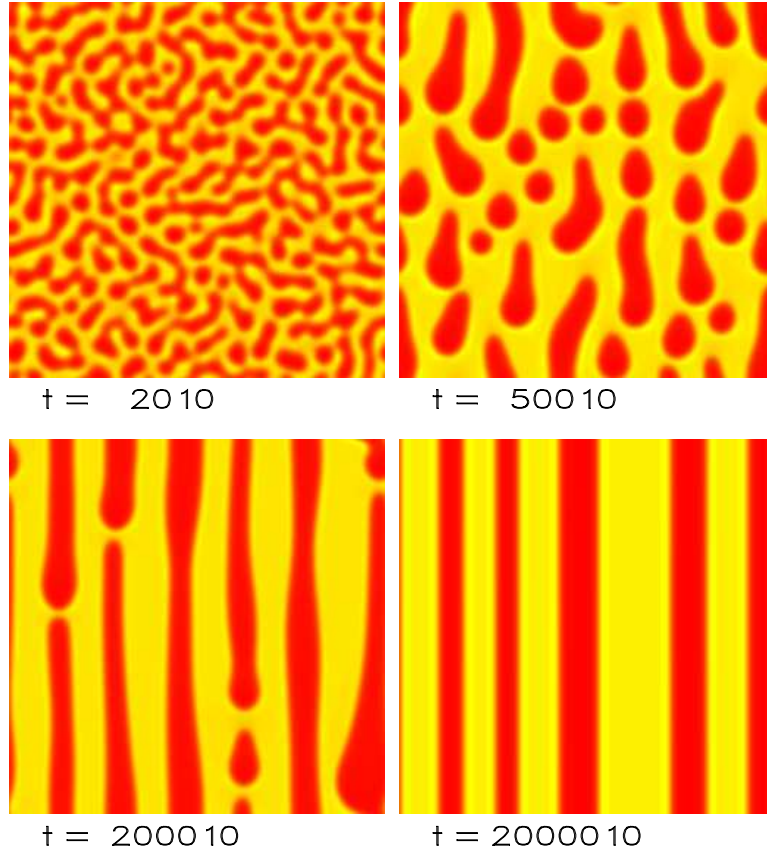


Figure 4.11: *Pattern formation in the inclined film. Parameters are those of Fig. 4.6 but the fluid is very slightly inclined in vertical direction. After the linear stage, the pattern gets anisotropic and finally a periodic structure of parallel fluid pipes with a certain wave length is stabilized.*

a structure of more or less equally spaced pipes where the fluid flows down inside. The effect of inclination on the dynamical scaling law Eq. (4.22) can be seen from Fig. 4.12.

Finally we study the influence of a constant force perpendicular to a channel of depressed liquid. To this end we start the numerical integration with the initial condition

$$u(x, y, t = 0) = \begin{cases} -0.77 & \text{for } 0 \leq y \leq L/8 \\ 0.11 & \text{for } L/8 < y < L \end{cases}$$

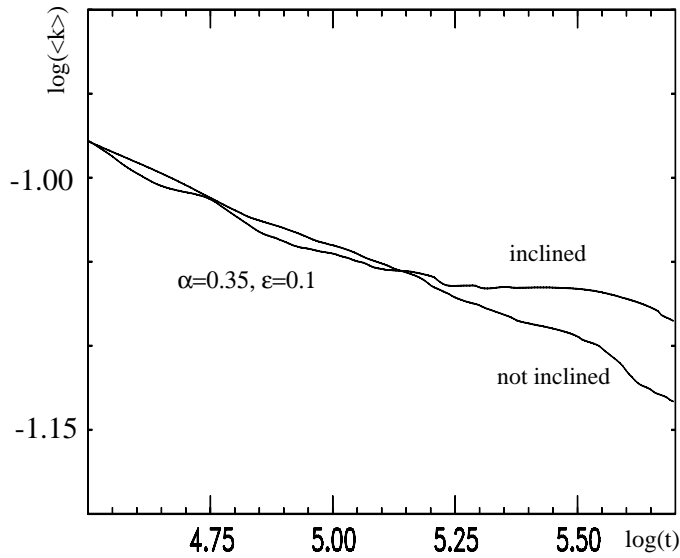


Figure 4.12: Comparison of the dynamical scaling of inclined and plane case. After $t \approx 100.000$ the stabilization of the wave length in the inclined case can be clearly seen.

where L is the total length of the layer. Both heights, the elevated as well as the depressed lay outside the spinodal region, i.e. the flat film in this parts is stable. To avoid the unphysical homogeneity in x -direction of the initial condition we add small fluctuations of about 1 per cent. The layer in this numerical experiment is inclined by about 1° (if the fluid is a silicone oil film with depth 1mm). Then the channel moves with the average velocity of $\approx 1\text{mm/sec}$. After about $t = 10.000$ (corresponding to about 300 sec) a phase instability of the back front of the channel (or the leading front of the elevated part) can be clearly observed (Fig. 4.12). Later on, the opposite front gets unstable with a smaller wave length, as studied for a liquid ridge on an inclined isothermal plate in [122]. At this stage, both fronts are well separated and can be considered as independent from each other. This changes if the front instabilities evolve further. The channel gets more and more constricted and finally breaks into several isolated holes. The final situation after a rather long evolution resembles that of Fig. 4.11.

For horizontal films the extracted scaling law $k \sim t^{-\beta}$ with $\beta = 0.21 \pm 0.01$ indicates that the coarsening is slower than in spinodal decomposition, where

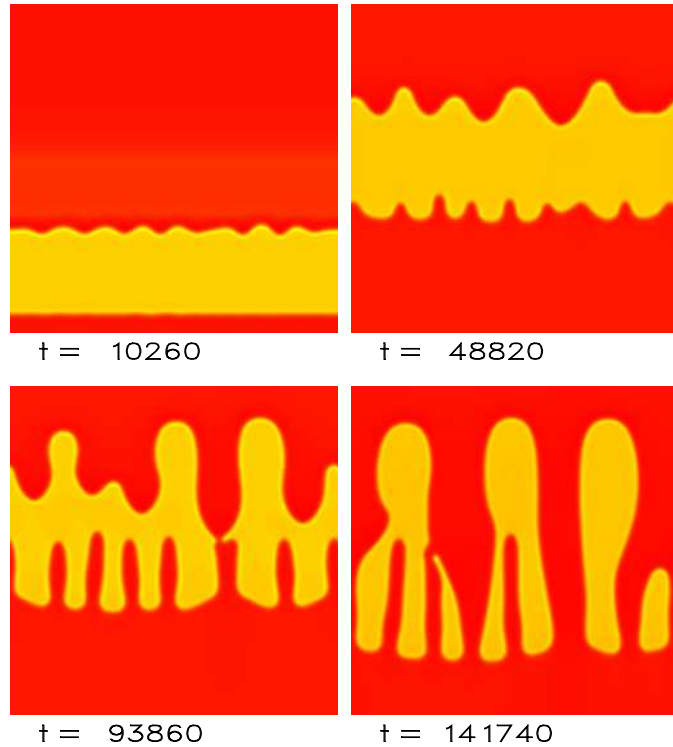


Figure 4.13: *Evolution of a channel on an inclined plane. Parameters are those of Fig. 4.7 in the hole regime. Both edges of the channel get unstable on different time scales. The trailing edge is disturbed faster with a larger wave length. Finally the two edges meet on several points and the channel separates.*

$\beta = 1/3$ as given by the Lifshitz-Slyozov-Wagner theory (see for example [59]). The inclusion of hydrodynamic effects in the description of spinodal decomposition gives even larger exponents for the long time limit (in 2D case: $\beta = 1/2$ viscosity controlled, $\beta = 2/3$ inertia controlled [90]).

However, the exponent found in Section 4.2.6 is similar to $\beta = 0.22$ found in numerical simulations for spinodal decomposition with a mobility that depends strongly on concentration implying the prevalence of surface diffusion over bulk diffusion [56]. A scaling argument for this case yields $\beta = 1/4$ [56]. To our knowledge for spinodal dewetting there exist no analytic or numeric results for the scaling exponent in two dimensions (for one dimension see [40]). We also mention that to our knowledge there exists no theory for the

mechanism of nonlinear wavelength selection and stabilization of a periodic structure in the inclined case, which can be clearly seen from our numerical simulations.

4.3 Influence of external disturbances

Here we investigate the influence of a time- and space-periodic pressure term on thin film evolution [93]. Practically this can be realized in different ways. (i) One can irradiate the free film surface with ultra sound that leads to a time modulation of the pressure at the liquid-gas interface. (ii) A time-periodic disjoining pressure appears in the co-moving frame for a liquid film, sliding down an inclined substrate with a periodic heterogeneity [105]. (iii) The use of time- and space-periodic electric fields and electrowetting [49] can give rise to a time-periodic term in the total energy of the system.

The main idea behind (i), (ii) and (iii) is to create a non-uniform mean flow in a certain direction. As was shown in Section 4.2, large scale mean flow may suppress coarsening and stabilize certain periodic surface structures in the long-time limit.

In the first part of this section focus on the most simple time- and space-periodic pressure term, not coupled to the film thickness which appears in case (i). Notice that a 'similar' method has been proposed in [44] and tested in [39] using light and surface tension gradients instead of sound pressure gradients on the liquid-gas interface. The second part is devoted to inhomogeneous wetting [25].

For ultrathin films on a solid substrate the function $\partial_h f(h)$ in Eq. (4.1) can also be specified by the combination of a disjoining pressure derived from diffuse interface theory [88, 129] and a hydrostatic pressure

$$\partial_h f(h) = \frac{2\kappa}{a} e^{-h/l} \left(1 - \frac{1}{a} e^{-h/l}\right) + \rho g h, \quad (4.23)$$

where ρ is the density of the liquid, g is the gravitational acceleration, κ has the dimension of a spreading coefficient per length, a is a small dimensionless positive parameter describing the wetting properties in the regime of partial wetting, l is the length scale of the diffuse interface [88, 129]. However, note that the main results for this model will not qualitatively differ from results for other disjoining pressures combining a short-range destabilizing and a long-range stabilizing component as, for example, used in [112]. This has been shown for homogeneous substrates in Refs. [127, 129, 126].

4.3.1 Ultrasound

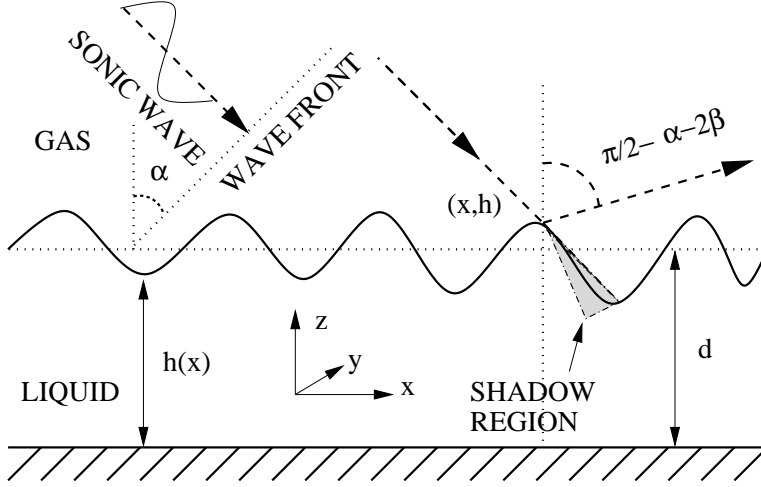


Figure 4.14: Sketch of the geometry. The sonic wave is irradiated under an angle α onto the film of mean thickness d . If α is smaller than the inclination $\beta^{inc} = \arctan(dh/dx)$ of the surface at some point shadow regions may exist.

To cover the driving mechanism (i), outlined above, we regard additionally an external sonic disturbance hitting the surface under an angle α as sketched in Fig. 4.14. The sonic wave breaks the isotropy of the system and is characterized by its wave length, $\lambda_s = 2\pi/k_s$, frequency, $\omega = k_s c$, wave number, k_s , and the velocity of sound in the ambient gas, c . The liquid may be considered to be incompressible if the sonic wave length is much larger than the characteristic size of the system, here the film thickness d . The pressure oscillates in the ambient gas with the sound frequency. Assuming complete reflection of the sound wave at the film surface the resulting time- and position-dependent pressure field at the film surface can be accounted for by adding to P_0 in the equation Eq. (4.1) the term

$$P_s(x, t) = p \cos(\omega t - \phi), \quad (4.24)$$

where p stands for the pressure amplitude in the sonic wave. The phase ϕ (defined with respect to an arbitrary wave front) at the film surface is given by

$$\phi(x, h(x)) = k_x x - k_z (h(x) - d), \quad (4.25)$$

where d denotes the mean film thickness and k_x and k_z are projections of the wave vector onto the x - and z - direction, respectively. The pressure distribution Eq. (4.24) is correct if (i) the sonic wave can reach the film surface freely, i.e. if there are no shadow regions (see Fig. 4.14) and (ii) if reflected waves do not fall onto the film surface elsewhere. Condition (i) is fulfilled if the angle α is larger than the maximal surface inclination of the film, β_{\max} , whereas (ii) holds if $\alpha > 3\beta_{\max}$ is satisfied. To be able to use lubrication approximation β_{\max} has to be small. This implies that both problems are avoided if α is of order one. Then k_x and k_z are of the same order and the second term in Eq. (4.25) can be neglected because $d \ll L$, with L the typical scale parallel to the substrate.

Using $k_x = k_s \sin \alpha$ the pressure Eq. (4.24) finally writes

$$\Delta P_s(x, t) = p \cos(\omega t - k_s x \sin \alpha) \quad (4.26)$$

The system Eq. (4.1) and Eq. (4.26) will now be used to illustrate the evolution of ultrathin films below 100 nm thickness that are unstable due to their wetting properties [80].

For $p = 0$ the linearized equation Eq. (4.1) predicts the onset of a type- II_s [7] instability at $\partial_{hh}f(d) = 0$. In the short-time regime one expects isotropic patterns with the typical wave length $\lambda_0 = 2\pi\sqrt{2\sigma/|\partial_{hh}f(d)|}$ and characteristic growth time $\tau = 12\eta\rho\sigma/d^3(\partial_{hh}f(d))^2$.

To non-dimensionalize we scale the (x, y) coordinates with $\lambda_0/2\pi$, film thickness with the mean film thickness d and time with characteristic growth time τ . Incorporating P_s , and using the same symbols now for non-dimensional variables the film evolution equation Eq. (4.1) becomes

$$\partial_t h = -\nabla [h^3 \nabla (\Delta h - g(h))] + \partial_x [h^3 \delta \sin(\Omega t - K_s x)], \quad (4.27)$$

with

$$g(h) = 2 \frac{\partial_h f(dh)}{d|\partial_{hh}f(d)|} = 2 \frac{e^{-\gamma h}(1 - \frac{1}{a}e^{-\gamma h}) + \gamma Gh}{\gamma|G + \frac{2}{a}e^{-2\gamma} - e^{-\gamma}|}, \quad (4.28)$$

and the dimensionless parameters: $G = \frac{\rho g a l}{2\kappa}$ and $\gamma = \frac{d}{l}$. The sonic wave is characterized by the dimensionless wave vector $K_s = \frac{\lambda_0}{\lambda_s} \sin \alpha$, amplitude $\delta = K_s \frac{p}{\sigma d} (\frac{\lambda_0}{2\pi})^2$, and frequency $\Omega = \frac{2\pi\tau}{T}$.

The non-dimensionalization we use is suitable for the estimation of K_s and Ω . The period of the sonic wave T is much smaller than the characteristic growth time τ , so that Ω is a large number. The sonic wave length λ_s may be either much bigger than λ_0 or may have the same size, yielding K_s to be either rather small or of order one.

Linear behavior

For $\delta \neq 0$ a flat film is not anymore a solution of the equation Eq. (4.27). But one can still use linear analysis to study the initial stage of evolution. Introducing the small deviation $u(x, y, t) = h(x, y, t) - h_0$ and linearizing Eq. (4.27) in u gives

$$\partial_t u = -2\Delta u - \Delta^2 u + \delta \partial_x [(1 + 3u) \sin(\Omega t - K_s x)], \quad (4.29)$$

For $\delta \neq 0$ equation Eq. (4.29) is inhomogeneous due to the term $\delta \partial_x \sin(\Omega t - K_s x)$. Its general solution is a sum of the solution u^H of the corresponding homogeneous problem and a partial solution u^I of the inhomogeneous equation.

Using the ansatz $u(x, y, t) = \tilde{u}(x, t) \exp(i\chi y)$ we transform Eq. (4.29) to

$$\begin{aligned} \partial_t \tilde{u} = & -\partial_x^4 \tilde{u} - (2 - 2\chi^2) \partial_x^2 \tilde{u} + (2\chi^2 - \chi^4) \tilde{u} + 3\delta \sin(\Omega t - K_s x) \partial_x \tilde{u} \\ & - 3\delta K_s \cos(\Omega t - K_s x) \tilde{u} - \delta K_s \cos(\Omega t - K_s x) \end{aligned} \quad (4.30)$$

First we wish to find the solution \tilde{u}^I of the inhomogeneous equation Eq. (4.30). To do that we use $\frac{1}{\Omega}$ as a small parameter and set $\tilde{u}^I = U_I^1 + U_I^2 + \dots$, where $U_I^k \sim \Omega^{-k}$. In the first step we neglect all terms in the r.h.s. of Eq. (4.30) as compared with $\delta K_s \cos(\Omega t - K_s x)$. Integrating both sides over time we find $U_I^1 = -\frac{\delta K_s}{\Omega} \sin(\Omega t - K_s x)$. To find U_I^2 we set $\tilde{u}^I = U_I^1 + U_I^2$ and neglect U_I^2 as compared with U_I^1 in the r.h.s. of Eq. (4.30). Integration in time yields: $U_I^2 = \frac{\delta K_s}{\Omega^2} [-K_s^4 + (2 - 2\chi^2)K_s^2 + (2\chi^2 - \chi^4)] \cos(\Omega t - K_s x)$. The amplitude of the solution \tilde{u}^I remains small if $\frac{\delta K_s}{\Omega}$ is a small number.

The solution of the homogeneous equation Eq. (4.30) may also be represented as a sum $U_h^1 + U_h^2 + \dots$, where $U_h^1 = \varepsilon e^{\beta t + ikx}$ is a small-amplitude solution ($\varepsilon \sim 1/\Omega$) of Eq. (4.30) in the case $\delta = 0$. The next order correction U_h^2

may be easily calculated by assuming that $e^{\beta t}$ varies slowly in time T : $U_h^2 = -\frac{3\delta}{\Omega}[\cos(\Omega t - K_s x)\partial_x U_h^1 + K_s \sin(\Omega t - K_s x)U_h^1]$. The amplitude of U_h^2 is of order $\frac{\varepsilon}{\Omega} = \frac{1}{\Omega^2}$.

Summarizing we may write the general solution of the equation Eq. (4.29) up to terms Ω^{-2} :

$$\tilde{u} = \varepsilon \exp(\beta t + ikx + i\chi y) - \frac{\delta K_s}{\Omega} \sin(\Omega t - K_s x) + O(\Omega^{-2}) \quad (4.31)$$

In the linear stage of evolution one finds a plane traveling surface wave with small amplitude, described by the second term in Eq. (4.31). Any infinitesimal perturbation to this plane wave (first term in Eq. (4.31)) has a growth rate β equal to that in the case without sonic disturbance.

As we have seen, the general solution Eq. (4.31) is a sum of two functions. The first one varies slowly in time, the second one is periodic with period T . The coupling between these two functions is of order $\frac{1}{\Omega^2}$.

Non-linear behavior

Considering high-frequency sound one may use the averaging method [106] to derive an effective evolution equation, starting from Eq. (4.27). According to this method we assume the general solution of the equation Eq. (4.27) to be a sum of two functions $h = \bar{h} + h'$, where \bar{h} varies slowly in time and h' is some periodic function with small amplitude. Linearizing Eq. (4.27) with respect to h' and keeping the leading oscillating terms, we find after integration in time:

$$h' = -\frac{\delta}{\Omega} [(\partial_x \bar{h}^3) \cos(\Omega t - K_s x) + K_s \bar{h}^3 \sin(\Omega t - K_s x)] \quad (4.32)$$

Integrating now both sides of Eq. (4.27) over one period T , and keeping only the first non-vanishing term proportional to h' , we obtain (after replacing \bar{h} by h):

$$\partial_t h = -\nabla[h^3 \nabla(\Delta h - g(h))] - \frac{3}{2} \frac{\delta^2 K_s}{\Omega} \partial_x h^5, \quad (4.33)$$

Here it is necessary to mention that the linearization and the averaging procedures do not commute. Applying the averaging method to Eq. (4.29)

one finds that the effective evolution equation coincides with that for $\delta = 0$. So the equation Eq. (4.33) is only correct in the non-linear stage.

Numerical results

Examining Eq. (4.33), we recognize a similarity to the equation which de-

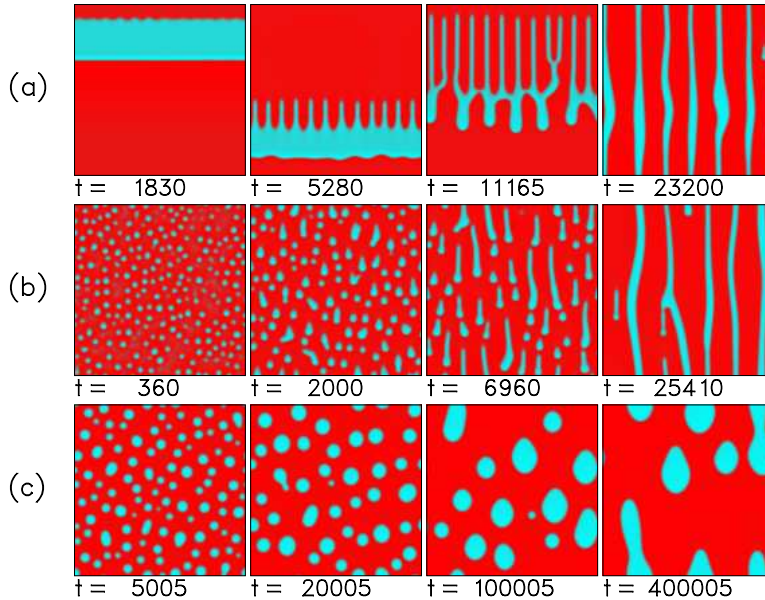


Figure 4.15: *Three time series found by numerical integration of Eq. (4.33) using different initial conditions and sound amplitudes. The direction of the sound wave is vertical. The grey scale indicates the thickness of the film, bright regions correspond to elevated parts of the surface. (a) Instability of a front, $\tilde{\alpha} = 0.002$. In the long-time limit, coarsening is terminated and parallel stripes are stabilized. (b) The same as (a) but with a random initial condition. Now small drops are formed which merge to bigger ones and then to rivulets. Finally, the same structure as in (a) is found. (c) Drop evolution for a smaller value of the sound amplitude $\tilde{\alpha} = 0.0004$. Also here, coarsening is suppressed in the long time limit and big drops result.*

scribes thin liquid films on an inclined substrate [7, 128]. The only quantitative difference between these two cases is the mobility factor for the driving term, which is here $Q_s(h) = h^5$ and $Q_{inc}(h) = h^3$ for films on an inclined substrate. Therefore we expect the same qualitative spatiotemporal behavior: fronts and randomly distributed initial conditions may get unstable and begin to travel, driven by the sound wave. Figs. 4.15(a),(b) show nu-

merical solutions which indeed demonstrate this effect. We solved equation Eq. (4.33) in a two-dimensional periodic domain using pseudo-spectral code.

Note, that in the initial stage of the movement of the liquid ridge in Fig. 4.15(a) front and back become unstable independently of each other with clearly different transversal wavelength. This corresponds very nicely to the same effect found for liquid ridges on inclined plates [7, 125, 122]. Therefore, it is to expect that also here with increasing driving force the transversal instability changes from an asymmetric varicose mode to an asymmetric zigzag mode and further to decoupled front and back instability [122].

It is remarkable that in both situations - Fig. 4.15(a) and Fig. 4.15(b) - coarsening is interrupted at a certain time and a structure of parallel stripes is stabilized, independent on the particular form of the initial conditions. Its final period depends on the force of the driving, here the square of the amplitude of the sound wave. For rather small values of the driving force, there seems to be a continuous transition to the non-driven case. Fig. 4.15(c) shows the evolution of drops as in Fig. 4.15(b), but for $\alpha = 0.0004$. Also here, coarsening is suppressed in the long time limit and big but still isolated drops result.

The drift velocity of the whole pattern strongly depends on the amplitude of the surface deflections. The drops with large amplitude drift faster than the drops on the inclined substrate due to the much stronger dependence of the mobility factor $Q_s(h)$ on the film thickness.

For practical application the plane sonic wave, irradiated to the film surface, may be of greater interest than the very slow drift on an inclined substrate. Furthermore, one can move selected parts of a pattern by using sonic waves with a spatially inhomogeneous intensity distribution (a beam of sound) For example, one may move a single drop in a desired direction.

To simulate this we consider the strength of the sonic wave to be a slow function of spatial coordinates $\delta = \delta(x, y)$. Then the last term in Eq. (4.33) modifies to

$$\frac{3}{2} \frac{K_s}{\Omega} \partial_x (\delta^2(x, y) h^5). \quad (4.34)$$

The result of a simulation is presented in Fig. 4.16. We chose the parame-

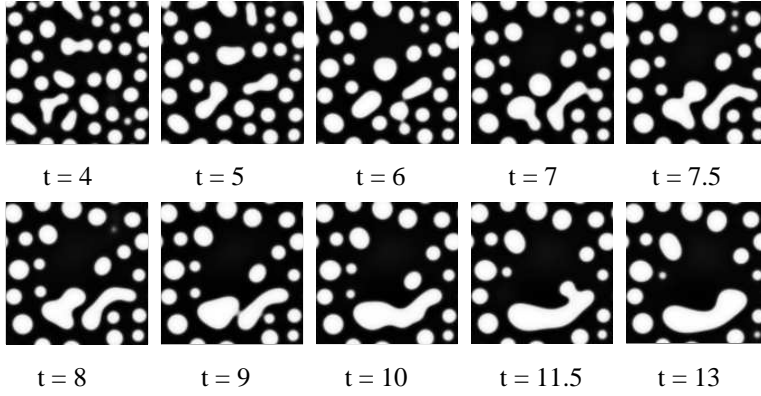


Figure 4.16: *Evolution of the system under the influence of a sonic disturbance with spatially inhomogeneous strength $\tilde{\alpha} = \tilde{\alpha}_0 \exp \left[-b \left(\left(\frac{x-L/2}{L} \right)^2 + \left(\frac{y-L/2}{L} \right)^2 \right) \right]$, where $\tilde{\alpha}_0 = 0.5$ is the strength of the sonic wave in the center of the system and $b = 25$ stands for the size of the active region. The control parameters $a = 0.1$, $\gamma = 3.5$, $G = 0.01$ correspond to the drop solution.*

ters (a , G , γ) corresponding to the drop regime [7] and wait until drops are formed before we switch on the sound beam, which has a maximal amplitude at the center of the system. Its strength falls exponentially in radial direction. A drop in the center is moved towards a region where the strength of the sonic wave is weak (non-active region). After the collision of the moved drop with a drop which is in the non-active region, a curved long drop is formed. The center of the system is now free of drops.

4.3.2 Inhomogeneous wetting

Here we show the influence of periodic inhomogeneities on surface pattern formation. The reason for these inhomogeneities can be different, depending on the particular system under consideration. As inhomogeneously wettable substrates [25] we only mention chemically patterned substrates or space dependent heating in the case of Marangoni convection.

Cahn-Hilliard equation

Since we wish to discuss the influence of inhomogeneous controlling from a

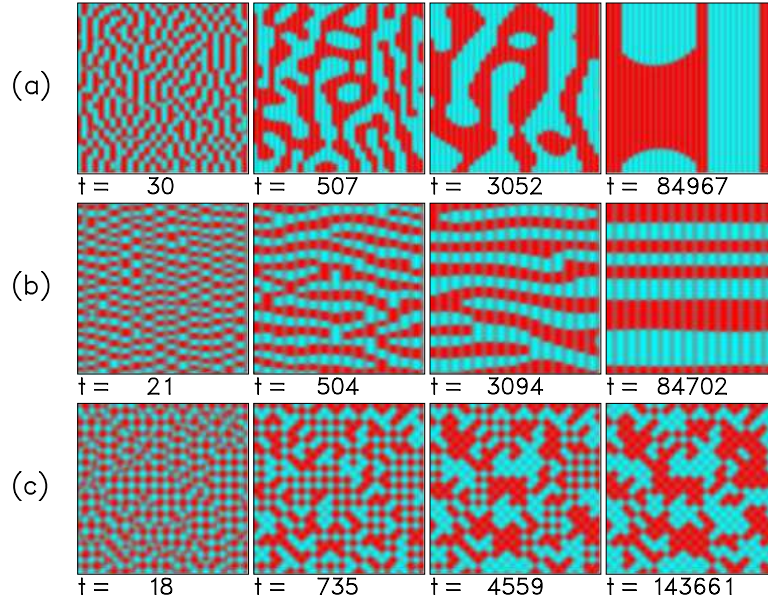


Figure 4.17: Numerical solutions of the modulated Cahn-Hilliard equation Eq. (4.38) for different inhomogeneities in form of stripes (a,b) or squares (c). If the modulation wave length is much shorter than the spinodal one, coarsening dominates (a). For $k_I \approx k_c$, patterns are aligned perpendicular. Pinning on a square grid is shown in (c). The steady state consists of filled or empty boxes.

more general point of view, we simplify our model Eq. (4.27) by assuming the system is close to its critical point [127, 120, 129]. We set the mobility to $Q(h) = 1$, leading to

$$\partial_t h = -\Delta(\Delta h - g(h)) \quad (4.35)$$

and use for g the general Taylor expansion

$$g(h) = a_0 + a_1 h + a_2 h^2 + a_3 h^3 \quad (4.36)$$

with the restriction for global stability $a_3 > 0$. Since only derivatives of h occur, we may shift h by a constant and rescale the coefficients in Eq. (4.36) to obtain $a_2 = 0$. Additional rescaling of height, time and space may lead to $a_1 = -1$ and $a_3 = 1$ if the condition for instability of the flat film is fulfilled.

The most simple way to include a multiplicative modulation is to allow for spatial variation of the linear coefficient a_1 . Thus we find

$$g(h) = a'_0 - (1 + \varepsilon f(x, y))h + h^3 \quad (4.37)$$

Inserting this into Eq. (4.35), we obtain the space dependent Cahn-Hilliard equation

$$\partial_t h = -\Delta h - \Delta^2 h + \Delta h^3 - \varepsilon \Delta(fh). \quad (4.38)$$

Without modulation, a type-II instability occurs with critical wave number $k_c = 1/\sqrt{2}$ and the cut-off wave number $k_m = \sqrt{2}$ [17].

Numerical results on inhomogeneous wetting

We present time series for different harmonic inhomogeneities f . First, we use

$$f(x) = \sin(k_I x)$$

and examine its influence with respect to the wave number k_I of the modulation. From two dimensional computations [121] it is known that for wave numbers much larger than the critical one ($k_I \gg k_c$) coarsening takes place just as for the homogeneous situation. Fig. 4.17(a) shows an evolution where $k_I = 2k_c$. Pinning is observed in the early stages, but finally coarsening dominates as for a homogeneous substrate. However, pinning is reminiscent during the whole evolution and patterns align *parallel* to the prescribed stripes.

A quite different situation occurs for a smaller wave number of the modulation. In the 2D case, pinning is expected to be dominant, which is also clearly seen in 3D. For $k_I = k_c$ the pattern organizes itself in stripes *perpendicular* to the inhomogeneity (Fig. 4.17b). It is also remarkable that coarsening is terminated after a certain time and a steady state with a finite wave vector results, just as in the driven systems from the previous section.

We conclude this paragraph showing the evolution on a square-like inhomogeneity of the form

$$f(x, y) = \sin(k_I x) \sin(k_I y)$$

with $k_I = k_c$ (Fig. 4.17c). Although coarsening still exists, pinning is dominant and the fluid forms filled or empty cells on the square grid prescribed by $f(x, y)$. Such a device could store information and may be used as a “liquid memory”.

Although both mechanisms of controlling the surface patterns (non-contact method using irradiation of the liquid surface with ultra sound and inhomogeneous wetting) are completely different, the resulting patterns show certain common features. In both systems, the rotational symmetry in the horizontal plane is broken by the external modulation. This lack of symmetry expresses itself in the form of the final stable surface pattern, which turns out to be periodic in both cases. Interestingly, in both cases the surface pattern can be organized in stripes perpendicular to the external force or modulation. Coarsening, obtained always in the early stages of temporal evolution, is interrupted at a certain time and periodic patterns stabilize. The periodicity length depends thereby mainly on the strength of the external modulation.

Chapter 5

Two-layer liquid films

5.1 Coupled evolution equations

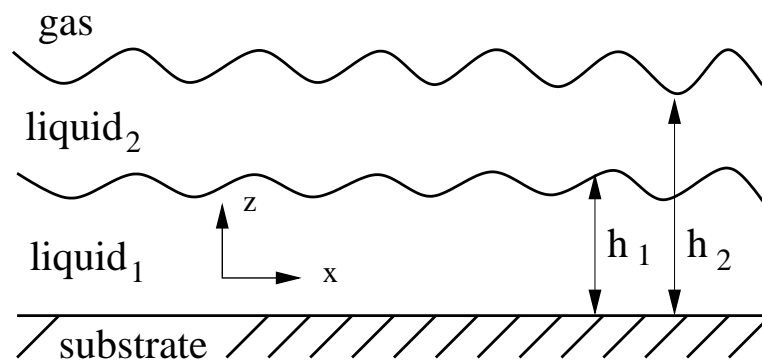


Figure 5.1: Sketch of the two-layer system in two dimensions. The local thickness of the lower layer is h_1 , the total local film thickness is h_2 .

In this chapter we consider a two-layer liquid film, which is obtained by superposing two immiscible liquids, as sketched in Fig. 5.1. First, we derive coupled evolution equations for the profiles of the liquid-liquid interface $h_1(x, y)$ and the liquid-gas interface $h_2(x, y)$. Considering a two-dimensional geometry the respective Stokes equations for the two layers are

$$\nabla(p_i + \phi_i) = \mu_i \Delta \vec{v}_i, \quad (5.1)$$

where $i = 1, 2$ denotes the respective layer. For each layer $\vec{v}_i = (u_i, w_i)$

is the velocity field, p_i the pressure, ϕ_i the potential of the bulk forces and μ_i the viscosity. The constant mean film thicknesses are denoted by $d_1 = (\int_0^L h_1 dx)/L$ and $d_2 = (\int_0^L h_2 dx)/L$ where L is the lateral system size. A lubrication approximation [80] is applied assuming the ratio of vertical and horizontal length scales to be small. As smallness parameter we use the ratio $\epsilon = d_1/\lambda$ where λ is the characteristic lateral length scale of the film instability. In zeroth order in ϵ the Stokes equations Eq. (5.1) simplify to

$$\mu_2 \partial_z^2 u_2 = \partial_x \bar{p}_2 \quad (5.2)$$

$$\partial_z \bar{p}_2 = 0 \quad (5.3)$$

$$\mu_1 \partial_z^2 u_1 = \partial_x \bar{p}_1 \quad (5.4)$$

$$\partial_z \bar{p}_1 = 0, \quad (5.5)$$

where the \bar{p}_i stand for $p_i + \phi_i$. At the substrate ($z = 0$) we use a Navier slip and a no-penetration condition, i.e.

$$u_1 = \beta \partial_z u_1 \quad \text{and} \quad w_1 = 0, \quad (5.6)$$

respectively. The slip length is denoted by β . At the liquid-liquid interface ($z = h_1$) we use the continuity of the velocity field, the kinematic condition and the continuity of the tangential component of the liquid stress tensor

$$u_1 = u_2, \quad w_1 = w_2, \quad (5.7)$$

$$w_1 = \partial_t h_1 + u_1 \partial_x h_1, \quad (5.8)$$

$$(5.9)$$

and

$$\mu_1 \partial_z u_1 - \mu_2 \partial_z u_2 = \partial_x \sigma_{12}, \quad (5.10)$$

respectively. The normal stress condition is discussed below. At the liquid-gas interface ($z = h_2$) only the kinematic condition and the continuity of the tangential component of the liquid stress tensor apply, i.e.

$$w_2 = \partial_t h_2 + u_2 \partial_x h_2, \quad (5.11)$$

$$\mu_2 \partial_z u_2 = \partial_x \sigma_2. \quad (5.12)$$

The σ_{12} and σ_2 stand for the interfacial tensions of the liquid-liquid and of the liquid-gas interface, respectively. The boundary conditions for the normal component of the stress tensor are written incorporating the disjoining pressures at the liquid-liquid $\Pi_1(h_1, h_2)$ and at the liquid-gas $\Pi_2(h_1, h_2)$ interface, respectively. They represent effective molecular interactions between the interfaces that result, for instance, from Van der Waals interactions [47]. They are discussed in detail below. For the liquid-gas interface ($z = h_2$) we obtain

$$p_2(h_2) - p_0 = -\sigma_2 \partial_x^2 h_2 + \Pi_2(h_1, h_2)$$

and for the liquid-liquid interface ($z = h_1$)

$$p_1(h_1) - p_2(h_1) = -\sigma_{12} \partial_x^2 h_1 + \Pi_1(h_1, h_2), \quad (5.13)$$

where p_0 is the constant pressure in the gas atmosphere. Equations Eqs. (5.13) can be written in terms of variations of an energy functional $F[h_1, h_2]$

$$\begin{aligned} p_1(h_1) - p_2(h_1) &= \frac{\delta F}{\delta h_1} \\ p_2(h_2) - p_0 &= \frac{\delta F}{\delta h_2}, \end{aligned} \quad (5.14)$$

with

$$F = \int \left(\sigma_1 \frac{(\partial_x h_1)^2}{2} + \sigma_2 \frac{(\partial_x h_2)^2}{2} + f(h_1, h_2) \right) dx, \quad (5.15)$$

and $f(h_1, h_2)$ being the free energy of the flat films per unit area.

Equations Eq. (5.2) and Eq. (5.4) are integrated three times with respect to z to obtain the stream functions Ψ_i , defined by ($w_i = -\partial_x \Psi_i$, $u_i = \partial_z \Psi_i$). The six x -dependent integration constants are determined using the boundary conditions Eq. (5.6), Eq. (5.7), Eq. (5.10), and Eq. (5.12). Thus the velocity fields in the two layers are given by

$$\begin{aligned} u_1 &= \frac{1}{\mu_1} (\partial_x \bar{p}_1) \frac{z^2}{2} + \frac{1}{\mu_1} (z + \beta) K_1 \\ u_2 &= \frac{1}{\mu_2} (\partial_x \bar{p}_2) \frac{z^2}{2} + \frac{1}{\mu_2} K_2 (z - h_1) - \frac{\partial_x \bar{p}_2}{\mu_2} \frac{h_1^2}{2} + u_1(h_1), \end{aligned} \quad (5.16)$$

with $K_1 = K_2 + \partial_x \sigma_{12} + [(\partial_x \bar{p}_2) - (\partial_x \bar{p}_1)] h_1$ and $K_2 = \partial_x \sigma_2 - (\partial_x \bar{p}_2) h_2$.

The stream functions Ψ_i are related to the flow in the lower layer $\Gamma_1 = \int_0^{h_1} u_1 dz$ and to the one in the upper layer $\Gamma_2 = \int_{h_1}^{h_2} u_2 dz$ by $\Gamma_1 = \Psi_1(h_1)$, $\Gamma_1 + \Gamma_2 = \Psi_2(h_2)$. Using the Ψ_i we rewrite equations Eq. (5.8) and Eq. (5.11) to obtain the evolution equations for the two interface profiles

$$\partial_t h_1 + \partial_x [\Psi_1(h_1)] = 0, \quad (5.17)$$

$$\partial_t h_2 + \partial_x [\Psi_2(h_2)] = 0. \quad (5.18)$$

Written in terms of the energy functional they read

$$\begin{aligned} \partial_t h_1 &= \partial_x \left[Q_{11} \partial_x \frac{\delta F}{\delta h_1} + Q_{12} \partial_x \frac{\delta F}{\delta h_2} - D_{11} \partial_x \sigma_{12} - D_{12} \partial_x \sigma_2 \right] \\ \partial_t h_2 &= \partial_x \left[Q_{21} \partial_x \frac{\delta F}{\delta h_1} + Q_{22} \partial_x \frac{\delta F}{\delta h_2} - D_{21} \partial_x \sigma_{12} - D_{22} \partial_x \sigma_2 \right], \end{aligned} \quad (5.19)$$

with the mobility matrices of the pressure terms

$$\mathbf{Q} = \frac{1}{\mu_1} \begin{pmatrix} \frac{h_1^3}{3} + \beta h_1^2 & \frac{h_1^2}{2} (h_2 - \frac{h_1}{3}) + \beta h_1 h_2 \\ \frac{h_1^2}{2} (h_2 - \frac{h_1}{3}) + \beta h_1 h_2 & \frac{h_1^2}{2} (h_2 - \frac{h_1}{3}) + \beta h_1 h_2 \end{pmatrix} \quad (5.20)$$

and of the tangential stress terms

$$\mathbf{D} = \frac{1}{\mu_1} \begin{pmatrix} \frac{h_1^2}{2} + \beta h_1 & \frac{h_1^2}{2} + \beta h_1 \\ h_1 (h_2 - \frac{h_1}{2}) + \beta h_2 & \frac{\mu_1 (h_2 - h_1)^2}{2\mu_2} + h_1 (h_2 - \frac{h_1}{2}) + \beta h_2 \end{pmatrix} \quad (5.21)$$

respectively. Note, that the mobility matrix \mathbf{Q} is symmetric and all mobilities Q_{ik} and D_{ik} are positive. Dropping the terms representing the effective molecular interactions, equations Eqs. (5.19) represent the fully nonlinear equivalent for the weakly nonlinear equations derived in Ref. [73, 74]. Assuming that the interfacial tensions are influenced by thermocapillarity only, one can express the derivatives $\partial_x \sigma_{12}$ and $\partial_x \sigma_2$ in terms of gradients of local thicknesses $\partial_x h_i$. This is done in the Appendix.

For isothermal ultrathin liquid films one has ($\partial_x \sigma_{12} = \partial_x \sigma_2 = 0$). The situation is then relaxational (or variational), i.e. equations Eqs. (5.19) possess a Lyapunov functional, namely the energy functional F , which decreases

monotonically in time as shown next. The total time derivative of the Lyapunov functional is $dF/dt = \int \left(\frac{\delta F}{\delta h_1} \partial_t h_1 + \frac{\delta F}{\delta h_2} \partial_t h_2 \right) dx$. Expressing $\partial_t h_i$ by Eqs. (5.19) and using partial integration with periodic boundary conditions, one obtains

$$\frac{dF}{dt} = - \int \sum_{i,k} Q_{ik} \left(\partial_x \frac{\delta F}{\delta h_i} \right) \left(\partial_x \frac{\delta F}{\delta h_k} \right) dx. \quad (5.22)$$

Because

$$\begin{aligned} \det \mathbf{Q} = & \frac{(h_2 - h_1)^3 h_1^3}{9\mu_1\mu_2} + \frac{1}{12\mu_1^2} h_1^4 (h_2 - h_1)^2 + \\ & \beta \left(\frac{h_1^3}{3\mu_1^2} (h_2 - h_1)^2 + h_1^2 \frac{(h_2 - h_1)^3}{3\mu_1\mu_2} \right) > 0 \end{aligned} \quad (5.23)$$

and $Q_{ii} > 0$, the quadratic form in Eq. (5.22) is positive definite implying $dF/dt < 0$. The existence of F allows to identify the stationary solutions of Eqs. (5.19) with the extrema of F . This will be used below in Section 5.5.2.

5.2 The disjoining pressures

In many important cases, as for instance, for polymer films on apolar substrates [107, 97], the interaction energy is mainly determined by its long-range apolar dispersion part. However, if the model only takes into account a destabilizing long-range interaction the time evolution definitively leads to rupture of the upper or lower layer, as will be shown in Section 5.4, making it impossible to study the long-time coarsening behavior. To be able to study the long-time evolution one has to include stabilizing short-range interactions, introduced in Section 3.2. into the model. Although these are normally not included for films of thicknesses above 10 nm because they do not change the stability of flat films, also for such films they become important in the non-linear stage of evolution when the local thicknesses become comparable to their interaction length.

As detailed in Section 3.2, the long-range part of the interaction energy for each pair of interfaces (see Fig. 5.1) resulting from dispersive Van der Waals interactions is given by $A_{ijkl}/12\pi h^2$, where A_{ijkl} is a (four-indices) Hamaker

constant which corresponds to the interaction between the interfaces $(i - j)$ and $(k - l)$. Each index in A_{ijkl} can be one out of $g, 1, 2$ and s , denoting gas, liquid 1, liquid 2 and substrate, respectively.

The short-range forces which can be of an electrostatic or structural nature [118, 27] decay exponentially with h (see Section 3.2). The corresponding interaction energy between the interfaces $(s - 1)$ and $(1 - 2)$ is given by $S_1 \exp[(l_0 - h_1)/l_1]$ and between the interfaces $(1 - 2)$ and $(2 - g)$ by $S_2 \exp[(l_0 - (h_2 - h_1))/l_2]$, where $l_0 = 0.158$ nm is the Born repulsion length, and $l_1, l_2 \sim 1..10$ nm are the interaction lengths of the short-range interactions [111]. Further on we consider the two correlation lengths l_1 and l_2 to be equal and denote them by l . $S_1 > 0$ and $S_2 > 0$ are the short-range components of the total spreading coefficients. They are related to the lower layer on the substrate below a bulk of the upper liquid and to the upper layer on the lower film as substrate below the ambient gas, respectively. We do not take into account short-range interactions between interfaces $(s - 1)$ and $(2 - g)$.

Collecting the long-range and the short-range forces the disjoining pressures $\Pi_1(h_1, h_2)$ and $\Pi_2(h_1, h_2)$ are specified as

$$\begin{aligned} \Pi_1(h_1, h_2) &= \frac{A_{21s}}{6\pi h_1^3} - \frac{A_{12g}}{6\pi(h_2 - h_1)^3} - \frac{S_1}{l} \exp\left[\frac{l_0 - h_1}{l}\right] + \\ &\quad \frac{S_2}{l} \exp\left[\frac{l_0 - (h_2 - h_1)}{l}\right] \\ \Pi_2(h_1, h_2) &= \frac{A_{12g}}{6\pi(h_2 - h_1)^3} + \frac{A_{g21s}}{6\pi h_2^3} - \frac{S_2}{l} \exp\left[\frac{l_0 - (h_2 - h_1)}{l}\right] \end{aligned} \quad (5.24)$$

Then the energy functional

$$\begin{aligned} F &= \int \left[\sigma_{12} \frac{1}{2} (\partial_x h_1)^2 + \sigma_2 \frac{1}{2} (\partial_x h_2)^2 - \frac{A_{12g}}{6(h_2 - h_1)^2} - \frac{A_{21s}}{6h_1^2} - \frac{A_{g21s}}{6h_2^2} \right. \\ &\quad \left. + c_1(h_1 - d_1) + c_2(h_2 - d_2) + S_1 \exp(-h_1) + S_2 \exp(h_1 - h_2) \right] dx, \end{aligned} \quad (5.25)$$

where c_i are the Lagrange multipliers that ensure mass conservation for the two liquids. d_1 and d_2 denote the mean film thickness of the lower film and the total mean film thickness, respectively.

Further on we will separately consider the action of the long-range interaction only as well as the simultaneous action of short-range and long-range terms on the evolution of two-layer films.

5.3 General stability of flat films

We start the analysis of our model for two-layer films by discussing the linear stability of flat films with $h_1(x) = d_1$ and $h_2(x) = d_2$. Equations Eqs. (5.19) are linearized in $\epsilon \ll 1$ for small amplitude disturbances $\epsilon \chi_i \exp(\gamma t) \exp(kx)$ for $i = 1, 2$ where k , γ and $\chi = (\chi_1, \chi_2)$ are the wave number, growth rate and amplitudes of the disturbance, respectively. The dispersion relation $\gamma(k)$ is obtained by solving the resulting eigenvalue problem $(\mathbf{J} - \gamma \mathbf{I})\chi = 0$.

For the isothermal case ($\partial_x \sigma_{12} = \partial_x \sigma_2 = 0$ in Eqs. (5.19)), the corresponding *non*-symmetric Jacobi matrix \mathbf{J} is given by $\mathbf{J} = -k^2 \mathbf{Q} \cdot \mathbf{E}$, where \mathbf{Q} is the mobility matrix. \mathbf{E} is the energy matrix

$$\mathbf{E} = \begin{pmatrix} \frac{\partial^2 f}{\partial h_1^2} + \sigma_{12} k^2 & \frac{\partial^2 f}{\partial h_1 \partial h_2} \\ \frac{\partial^2 f}{\partial h_1 \partial h_2} & \frac{\partial^2 f}{\partial h_2^2} + \sigma_2 k^2 \end{pmatrix}, \quad (5.26)$$

where $f(h_1, h_2)$ is the local part of the energy density from Eq. (5.25). This yields

$$\gamma = \frac{\text{Tr}}{2} \pm \sqrt{\frac{\text{Tr}^2}{4} - \text{Det}}, \quad (5.27)$$

where $\text{Tr} = -k^2[2Q_{12}E_{12} + Q_{11}E_{11} + Q_{22}E_{22}]$ and $\text{Det} = k^4 \det \mathbf{Q} \det \mathbf{E}$ are the trace and the determinant of \mathbf{J} . Since $\det \mathbf{Q} \neq 0$ the eigenvalue problem can be written as the generalized eigenvalue problem $(k^2 \mathbf{E} + \gamma \mathbf{Q}^{-1})\chi = 0$. Because \mathbf{E} and \mathbf{Q}^{-1} are both symmetric and \mathbf{Q}^{-1} is positive definite one can deduce that all eigenvalues γ are real [65] as expected for a variational problem. In the non-isothermal case, the Jacobi matrix is given by $\mathbf{J} = -k^2(\mathbf{Q} \cdot \mathbf{E} - \mathbf{D} \cdot \mathbf{\Gamma})$, where $\mathbf{\Gamma}$ is a matrix of coefficients for the Marangoni

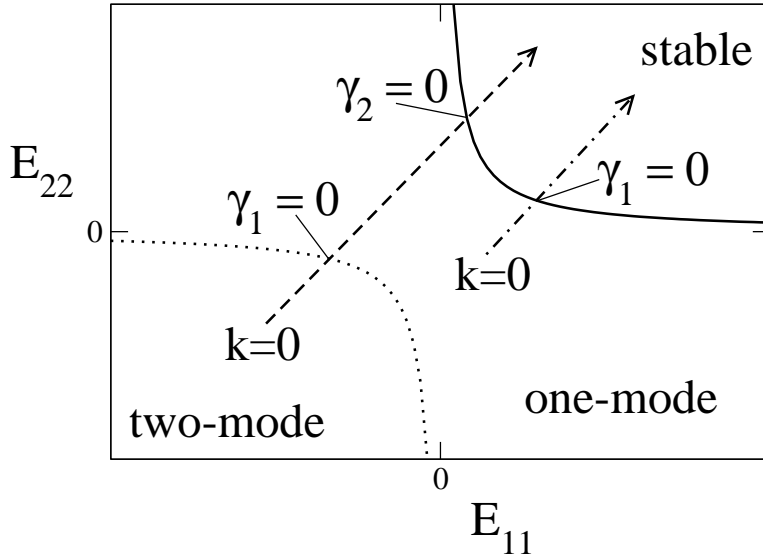


Figure 5.2: The schematic stability diagram for fixed coupling E_{12} . Shown are the stability threshold (solid line) and the boundary between the one-mode and the two-mode region (dotted line). Both are given by $\det \mathbf{E} = 0$ for increasing wave number k . Dashed and dot-dashed arrows represent parametric lines given by $(E_{11}(k)$ and $E_{22}(k)$). The dashed (dot-dashed) line starts at $k = 0$ in the two-mode (one-mode) region. At an intersection of a line $\det \mathbf{E}(k = 0)$ and a parametric line one of the growth rates changes its sign.

terms. It is defined in the Appendix. Neither the matrix \mathbf{D} nor $\mathbf{\Gamma}$ are symmetric. This leads to (in general) complex eigenvalues indicating the possibility of oscillating motion in the non-isothermal case [73, 74].

Going back to the isothermal case, inspection of the generalized eigenvalue problem shows that the stability threshold is completely determined by the eigenvalues of \mathbf{E} . Since the surface tension terms are always positive, the onset of the instability is always found for $k = 0$, i.e. the system is linearly stable, independently of the wavelength of the disturbance, for

$$\det \mathbf{E} > 0 \quad \text{and} \quad E_{11} > 0 \quad \text{at} \quad k = 0. \quad (5.28)$$

An instability sets in if at least one of the conditions Eq. (5.28) is violated. Then the flat two-layer film is unstable to disturbances with k larger zero

and smaller than a cutoff wavenumber

$$k_c^2 = -\frac{\eta}{2} \pm \sqrt{\frac{\eta^2}{4} + \frac{1}{\sigma_{12}\sigma_2} \left(\frac{\partial^2 f}{\partial h_1 \partial h_2} \right)^2}, \quad (5.29)$$

with $\eta = \left(\frac{1}{\sigma_{12}} \frac{\partial^2 f}{\partial h_1^2} + \frac{1}{\sigma_2} \frac{\partial^2 f}{\partial h_2^2} \right)$. The k_c are determined by the condition $\det \mathbf{E}(k_c) = 0$.

Fig. 5.2 shows a schematic stability diagram in the plane (E_{11}, E_{22}) . The stability threshold $E_{11}E_{22} = E_{12}^2$, $E_{11} > 0$ is a hyperbola, represented by the solid line. The unstable region below and left of that line is divided by a second hyperbola into a two-mode and a one-mode region. In the two-mode region both growth rates given by Eq. (5.27) are positive for k smaller than the respective cut-off k_c . In the one-mode region only one γ is positive for $k < k_c$. Fixing all other system parameters, $\det \mathbf{E}(k)$ is determined by k . If at $k = 0$ the system is in the two-mode region, then by increasing k one passes two times a line $\det \mathbf{E} = 0$, as indicated by the dashed arrow in Fig. 5.2. At each crossing a growth rates (equation Eq. (5.27)) becomes negative, i.e. a mode is stabilized. If at $k = 0$ the system is in the one-mode region the line $\det \mathbf{E} = 0$ is crossed only once (dot-dashed line).

5.4 Long-range interaction only

5.4.1 Scaling and flat film stability

As detailed above the stabilizing short-range interaction only becomes important if at least one layer thickness is locally comparable to the interaction length l , i.e. if a layer becomes thinner than about 10 nm. Therefore, to study the linear stability of thicker layers one can neglect the short-range terms in Eq. (5.25).

In this section we non-dimensionalize Eq. (5.19) using scales derived from the upper layer as an effective one-layer system. This is done to compare to the well understood one-layer systems. We scale \mathbf{x} with $\lambda_{\text{up}} = 4\pi(d_2 - d_1)^2 \sqrt{\pi\sigma_2/|A_{12g}|}$, h_i with $d_2 - d_1$ and t with $\tau_{\text{up}} = 48\pi^2\mu_2\sigma_2(d_2 - d_1)^5/A_{12g}^2$. The corresponding energy scale is $|A_{12g}|/16\pi^3(d_2 - d_1)^2$. The ratios of the mean thicknesses, surface tensions and viscosities are $d = d_2/d_1$, $\sigma = \sigma_2/\sigma_{12}$ and $\mu = \mu_2/\mu_1$, respectively. To compare with the lower layer as effective one-layer system one introduces in an analogous way the length scale λ_{low} and time scale τ_{low} .

In this case, equation Eq. (5.28) is used to study the role of the Hamaker constants Eq. (3.11) in the linear evolution of the system. First we note that the Hamaker constants are coupled through the refractive indices of the media n_i . This allows only for selected combinations of signs of the A_{ijk} and A_{ijkl} as given in Table 5.1.

For fixed Hamaker constants, i.e. fixed combination of materials, $\det \mathbf{E}_0 = \det \mathbf{E}(k=0)$ is a function of the ratio d of the layer thicknesses only. Using Table 5.1 one can show that for positive $\partial^2 f/\partial h_i^2$ the equation $\det \mathbf{E}_0(d) = 0$ can only have the solution $d = 1$, i.e. $d_2 - d_1 = 0$. This means that only for vanishing upper layer the system can be on the stability threshold. In consequence the stability threshold can *not* be crossed by solely changing the ratio of layer thicknesses.

The stability threshold shown as solid line in Fig. 5.3 is determined by \mathbf{E} for disturbances of infinite wavelength, i.e. $k = 0$. Changing d one finds a

refractive indices	A_{12g}	A_{21s}	A_{g21s}
$n_s > n_1, n_1 < n_2, n_2 > n_g$	+	+	-
$n_s < n_1, n_1 < n_2, n_2 > n_g$	+	-	+
$n_s < n_1, n_1 > n_2, n_2 > n_g$	-	+	+
$n_s > n_1, n_1 > n_2, n_2 > n_g$	-	-	-

Table 5.1: Possible combinations of signs of the different Hamaker constants for given order of the refractive indices of the involved medias.

line (trajectory) in the stability diagram Fig. 5.3 as shown for a variety of experimentally studied systems. Each trajectory lies entirely either in the stable or in the unstable region. For instance, for the Si/PMMA/PS/air system the second condition in Eq. (5.28) is violated for all d and the system is always unstable. At $d = 1$, i.e. for vanishing upper layer, the system is on the boundary between the one- and the two-mode regions (dashed line).

5.4.2 Flat film stability: one-layer vs. two-layer films

To compare the stability behavior of two-layer and one-layer films we introduce two effective one-layer films as follows. In (1) we assume the lower layer to be solid, i.e. we regard the upper layer as a one-layer film on a coated substrate. In (2) we assume the upper layer to be rigid but deformable by bending. The lower liquid layer corresponds then to a one-layer film on a solid bulk substrate. In case (1) the one-layer liquid film is unstable if the second derivative of the energy with respect to the film thickness h_2 is negative, $\partial^2 f/h_2^2 < 0$. The stability threshold at $\partial^2 f/h_2^2 = 0$ can be crossed by changing the layer thickness $h_2 - h_1$ or the thickness of the coating layer h_1 . This was demonstrated in Refs. [71] and [107] for a PS film on Si wafers covered with a 1.6 nm thick SiO layer. In case (2) the one-layer liquid film is unstable for $\partial^2 f/h_1^2 < 0$. It can also be destabilized by changing the layer thicknesses, as was shown in Ref. [26] for a rigid PS layer on top of a liquid PDMS layer on a Si substrate.

Comparing the stability thresholds for the two effective one-layer systems

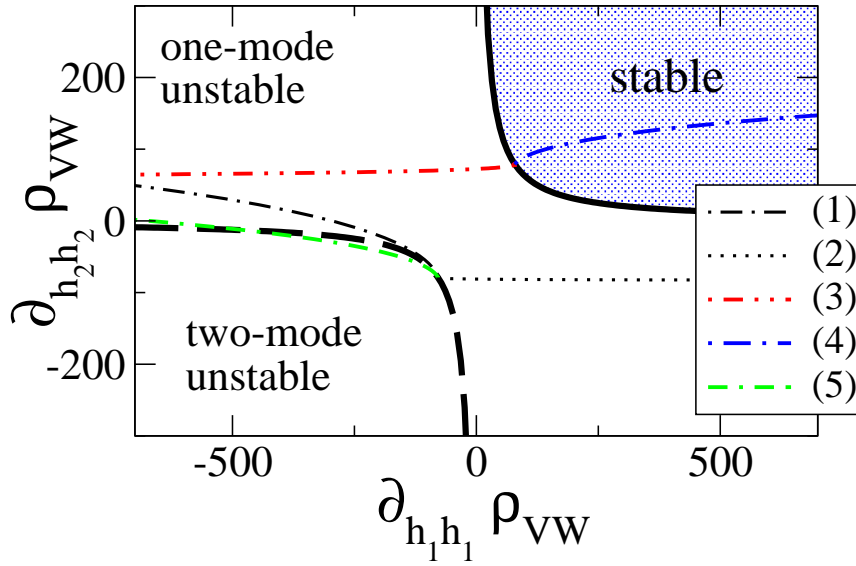


Figure 5.3: *Stability diagram for fixed scaled coupling $\partial_{h_1 h_2} \rho_{VW} = 8\pi^2 A_{12g}/|A_{12g}|$. Shown are the the stability threshold (solid line) and the boundary between unstable one-mode and two-mode regions (dashed line). The thin lines represent the trajectories for commonly studied systems: (1) Si/PMMA/PS/air, (2) SiO/PMMA/PS/air, (3) SiO/PS/PDMS/air, (4) Si/PS/PDMS/air, and (5) Si/PDMS/PS/air.*

to the stability diagram in Fig. 5.2 shows that the stability threshold of the two-layer system lies in the region where both effective one-layer systems are stable. This indicates that a two-layer system is always less stable than corresponding effective one-layer systems.

5.4.3 Different instability modes

The stability threshold can be studied in rather general terms as was done above because its main features do not depend on surface tensions or viscosities. However, this is not the case for the characteristics of the instability like mode type, growth rates or dominant wave length. To discuss these we focus in the following on selected two-layer films studied experimentally [71, 57, 109]. We consider various combinations of layers of polystyrene (PS), poly(methylmethacrylate) (PMMA) and poly(dimethylsiloxane) (PDMS) on

System	$A_{12g} \times 10^{-20}\text{J}$	$A_{21s} \times 10^{-20}\text{J}$	$A_{g21s} \times 10^{-20}\text{J}$
Si/PMMA/PS/air	1.49	3.8	-23.02
SiO/PMMA/PS/air	1.49	-0.024	0.15
SiO/PS/PDMS/air	-1.83	0.42	1.25

Table 5.2: Hamaker constants for various combinations of polymers.

a silicon (Si) or on a silicon-oxide (SiO) substrate. The Hamaker constants for different combinations are calculated using Eq. (3.11) and given in Table 5.2.

The linear instability of a two-layer film has two different modes. It can be of zigzag or varicose type. For the former the deflections of the two interfaces are in phase whereas for the latter they are in anti-phase. For special parameter values one can also find a mixed type, where the both modes are present because they have equal fastest growth rates.

The model studied in Ref. [13] assumes a thick lower layer thereby neglecting the interaction between the substrate and the liquid-liquid and the liquid-gas interface. In this case only the varicose mode can be unstable. In the general case, however, also the zigzag mode can become unstable. Both modes are normally asymmetric, i.e. the deflection amplitudes of the two interfaces differ. We characterize this asymmetry by $\phi = \chi_1\chi_2/(\chi_1^2 + \chi_2^2)$. Negative (positive) ϕ corresponds to varicose (zigzag) modes. The value $|\phi| = \pm 1/2$ represents the symmetric case, whereas $\phi = 0$ corresponds to maximal asymmetry, i.e. one of the interfaces is flat. The asymmetry increases with the ratio of the surface tensions σ . Note, that the dispersion relation and the type of the dominant mode depend on σ and μ , whereas the stability diagram Fig. 5.2 *does not*.

The two mode types are plotted in Fig. 5.4 for a Si/PMMA/PS/air and a SiO/PMMA/PS/air systems for different ratios of mean film thicknesses d and surface tensions σ . The dispersion relations $\gamma(k)$ are shown together with the corresponding ϕ . We show here that the type of the dominant mode can be changed by varying d or σ . Small values of d correspond to a varicose mode (Fig. 5.4(a)), whereas large values of d correspond to

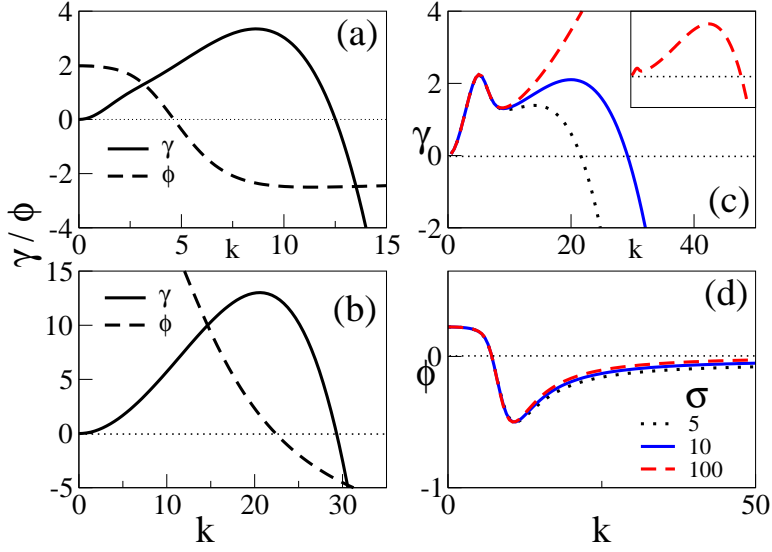


Figure 5.4: Shown are the growth rate γ and the corresponding angle ϕ for the leading eigenmode. Panel (a) shows 5ϕ and γ for the one-mode varicose region at $d = 1.4$. Panel (b) shows 50ϕ and γ for the one-mode zigzag region at $d = 2.4$. In (a) and (b) the symmetrical case is considered: $\sigma = \mu = 1$. Panels (c) and (d) give γ and ϕ , respectively, for a SiO/PMMA/PS/air system at $d = 2.16$ for $\mu = 1$ and different σ as given in the inset of (d).

a zigzag mode (Fig. 5.4(b)). When increasing σ for fixed d , the dominant mode type changes from the zigzag mode to the varicose one (Fig. 5.4(c) and Fig. 5.4(d)).

Strictly speaking, the concept of the mode type characterized by ϕ is only valid in the linear stage of the evolution. However, to discuss morphology changes we generalize this concept to nonlinear thickness profiles $h_i(x)$. We define a generalized mode or solution type by the integral

$$\phi_{\text{int}} = \frac{1}{L} \int \frac{(h_1 - d_1)(h_2 - d_2)}{[(h_1 - d_1)^2 + (h_2 - d_2)^2]} dx, \quad (5.30)$$

taken over the domain length L . In many cases the sign of the product $(h_1 - d_1)(h_2 - d_2)$ does not depend on x allowing to 'read' the mode type directly from the plots of the layer profiles. For small deflection amplitudes Eq. (5.30) gives again the linear mode type defined above. In the following we use the notion 'mode-type' in the linear and in the nonlinear regime.

5.4.4 Rupture acceleration

We simulate the coupled time evolution of h_1 and h_2 , Eq. (5.19), in an one-dimensional domain using a semi-implicit time integration scheme and periodic boundary conditions. Initial conditions consist of flat layers with an imposed noise of amplitude 0.001. Alternative pathways of dewetting that occur for different thickness ratios d are presented in Fig. 5.5 using a Si/PMMA/PS/air system as an example. Fig. 5.5 (a) shows that for a relatively small $d = 1.4$ the two interfaces start to evolve deflections that are in anti-phase indicating the dominance of a varicose mode. When the liquid-gas interface approaches the liquid-liquid interface the latter starts to move downwards due to dynamical effects. This pathway leads to rupture of the upper layer, i.e. at the liquid-gas interface. On the contrary, Fig. 5.5 (b) shows that for a larger $d = 2.4$ the growing deflections of the two interfaces are in phase indicating the dominance of a zigzag mode. As a consequence, here the lower layer ruptures, i.e. rupture occurs at the substrate. Note, that in both, Fig. 5.5 (a) and (b), at the moment of rupture the respective non-ruptured layer is also in an advanced stage of its evolution leading to subsequent rupture. This is remarkable because their time scales as effective one-layer systems are 15 times (Fig. 5.5 (a)) and 35 times (Fig. 5.5 (b)) slower than the time scales for the respective fast layer. The ratio of the time scales $\tau_{\text{up}}/\tau_{\text{low}}$ is proportional to $(d - 1)^5$, i.e. for a lower layer ten times thicker than the upper one the rupture time of the lower layer is about five orders of magnitude larger than the one of the upper layer. However, a simulation for a Si/PMMA/PS/air system with $d_1 = 10$ and $d_2 - d_1 = 1$ shows that at rupture of the upper layer at $t = 0.61\tau_{\text{up}} = 3.99 \times 10^{-5}\tau_{\text{low}}$ the lower layer already evolved a depression of one fourth of its thickness. If the lower layer is the fast one, the effect also exists but is less pronounced.

In both cases, the acceleration of the rupture of the slower layer is caused by the direct coupling of the layers via the liquid-liquid interface. The fast evolution of the thinner layer deforms the interface and brings the thicker layer beyond the slow linear stage of its evolution. If the upper layer is the driving layer the process is in addition dynamically enforced because the

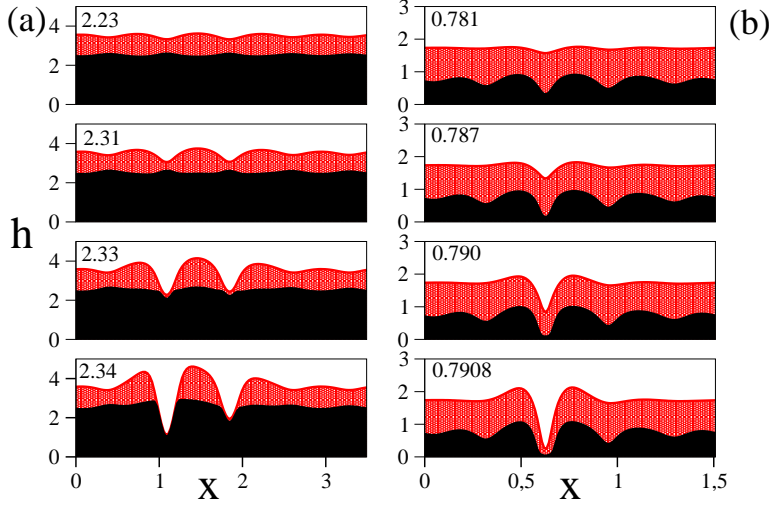


Figure 5.5: Snapshots from time evolutions of a two-layer film for a Si/PMMA/PS/air system at dimensionless times (in units of τ_{up}) as shown in the insets. (a) At $d = 1.4$ a varicose mode evolves leading to rupture of the upper layer at the liquid-liquid interface. The ratio of the time scales derived from upper and lower effective one-layer system is $\tau_{up}/\tau_{low} = 0.066$. (b) At $d = 2.4$ a zigzag mode evolves and rupture of the lower layer occurs at the substrate ($\tau_{up}/\tau_{low} = 34.98$). The domain lengths are 5 times the corresponding fastest unstable wave length and $\mu = \sigma = 1$.

liquid-liquid interface is 'pushed away' by the advancing liquid-gas interface.

5.4.5 Two-mode behavior

Further on, the simultaneous action of the van-der-Waals forces between the three interfaces allows for dispersion relations with two maxima. An experimental system showing this unusual form of $\gamma(k)$ can be realized with a substrate that is less polarizable than both layers. This is the case for the SiO/PMMA/PS/air system. A dispersion relation showing maxima of equal height is given for $d = 2.16$ and $\sigma = 10$ in Fig. 5.4(c). The maxima at small and large k correspond to strongly asymmetric zigzag and varicose modes, respectively. This implies that the larger (smaller) wavelength will predominantly be seen at the liquid-gas (liquid-liquid) interface (Fig. 5.6 (a)). In-

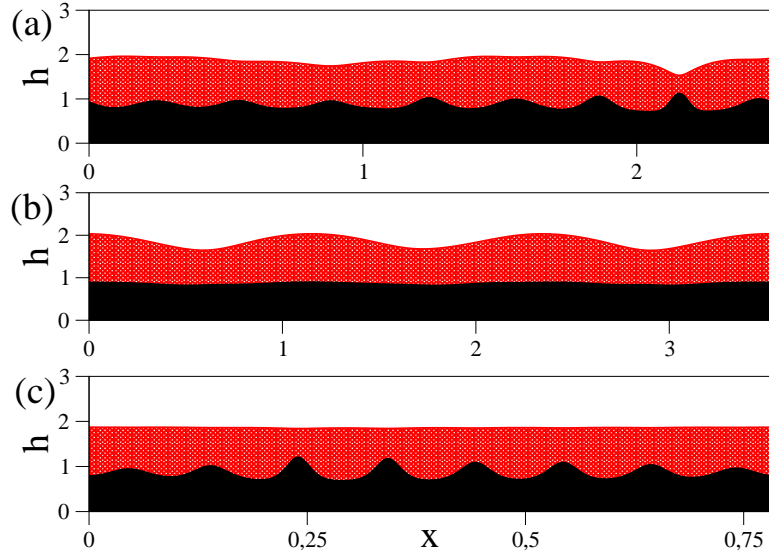


Figure 5.6: *Single snapshots from time evolutions of a SiO/PMMA/PS/air system for $d = 2.16, \mu = 1$ and different σ . (a) The respective evolutions of the two interfaces are dominated by modes of different wavelength ($\sigma = 10, t = 3.83$). In (b) and (c) the evolution is dominated by the liquid-gas and the liquid-liquid interface, respectively ($\sigma = 5, t = 3.9$ and $\sigma = 100, t = 0.52$).*

creasing (decreasing) the ratio of the surface tensions strengthens the smaller (larger) wavelength. This implies that solely changing σ by adding an otherwise passive surfactant one can switch from an evolution entirely dominated by the liquid-liquid interface to one dominated by the liquid-gas interface. This illustrates Fig. 5.6 by single snapshots from the non-linear time evolutions for different σ .

5.4.6 Limiting cases

For general d_i the radical in Eq. (5.27) does not allow to give an analytic expression for the wave number k_m and the characteristic growth time $\tau_m = 1/\gamma_m$ of the fastest growing mode. Nevertheless, one can derive asymptotic expressions for k_m and τ_m in the two important limiting cases of (1) small thickness of the upper layer $d_2 - d_1 \ll d_2$ and (2) small thickness of the lower layer $d_1 \ll d_2$. First consider case (1), which corresponds to a liquid film (the upper layer) on a liquid substrate (the very thick lower layer). The dimensional k_m and τ_m are then given by

$$\begin{aligned} k_m &= \frac{1}{(d_2 - d_1)^2} \sqrt{\frac{|A_{12g}|}{4\pi\sigma_{\text{eff}}}} \\ \tau_m &= \frac{16(2\pi)^2 \sigma_{\text{eff}} \mu_1 (d_2 - d_1)^6}{d_1 A_{12g}^2}, \end{aligned} \quad (5.31)$$

with $\sigma_{\text{eff}} = \sigma_1 \sigma_2 / (\sigma_1 + \sigma_2)$. Note that all variables are in their dimensional form.

Interestingly, the growth time τ_m depends only on the viscosity of the lower layer μ_1 and does not depend on μ_2 . This can be explained by the fact that the flow in the lower layer which is related to μ_1 , is much larger than that in the upper one [13]. At constant thickness of the lower layer, τ_m is proportional to $(d_2 - d_1)^6$, i.e. a liquid film on a bulk liquid substrate evolves faster than the same film on a solid substrate (growth time $\sim (d_2 - d_1)^5$) and even faster than the same film on a solid substrate with slippage (growth time $\sim (d_2 - d_1)^5 / [1 + 3\beta / (d_2 - d_1)]$).

In case (2), which corresponds to a liquid film (the lower layer) on a solid substrate below the other liquid (the very thick upper layer), the dimensional k_m and τ_m are given by

$$\begin{aligned} k_m &= \frac{1}{d_1^2} \sqrt{\frac{A_{21s}}{4\pi\sigma_1}} \\ \tau_m &= \frac{12(2\pi)^2 \sigma_1 \mu_1 d_1^5}{A_{21s}^2}. \end{aligned} \quad (5.32)$$

Note that in case (2) k_m and τ_m coincide with k_{low} and τ_{low} , respectively,

the characteristics of the dominant mode of the instability of a liquid film below a bulk liquid calculated using one-layer theory. A discussion of this geometry for a Rayleigh-Taylor instability can be found in Refs. [135] and [136].

5.5 Long-range and short-range interactions

From now on, we will take into account the stabilizing short-range terms in the Lyapunov functional. These terms provide the natural scaling for the vertical coordinate, given by the correlation length of the polar liquids l . To non-dimensionalize Eqs. (5.19) we scale the thicknesses with l , the lateral coordinate x with $\lambda = l(d_2 - d_1)\sqrt{2\pi\sigma_1/|A_{12g}|}$, and time t with $\tau = (2\pi)^2\sigma_1\mu_1l(d_2 - d_1)^4/A_{12g}^2$. Then the scaled energy functional

$$\begin{aligned}
 F = & \int \left[\frac{1}{2}(\partial_x h_1)^2 + \frac{\sigma}{2}(\partial_x h_2)^2 - \frac{\bar{A}_{12g}}{6(h_2 - h_1)^2} - \frac{\bar{A}_{21s}}{6h_1^2} - \frac{\bar{A}_{g21s}}{6h_2^2} \right. \\
 & \left. + c_1(h_1 - \bar{d}_1) + c_2(h_2 - \bar{d}_2) + \bar{S}_1 \exp(-h_1) + \bar{S}_2 \exp(h_1 - h_2) \right] dx,
 \end{aligned}
 \tag{5.33}$$

involves the scaled Hamaker constants $\bar{A}_{ijkl} = [(d_2 - d_1)/l]^2 A_{ijkl}/|A_{12g}|$, spreading coefficients $\bar{S}_i = 2\pi [(d_2 - d_1)]^2 S_i \exp(d_0/l)/|A_{12g}|$, and mean layer thicknesses $\bar{d}_i = d_i/l$. The c_i are Lagrange multipliers that ensure mass conservation for the two liquids. The corresponding energy scale is $|A_{12g}|/2\pi(d_2 - d_1)^2$ and the ratios of the mean layer thicknesses, surface tensions and viscosities are $d = d_2/d_1$, $\sigma = \sigma_2/\sigma_1$ and $\mu = \mu_2/\mu_1$, respectively. Further on, we denote the scaled variables using the same symbols as before, i.e. the scaled mean thicknesses are given by d_i and the local thicknesses by h_i . The non-dimensional mobility matrices are obtained from Eq. (5.20) and Eq. (5.21) by dropping the factor $1/\mu_1$ and replacing β by β/l .

5.5.1 Flat film stability

The stability analysis based only on long-range interactions becomes incorrect for layer thicknesses in the range of the interaction length l of

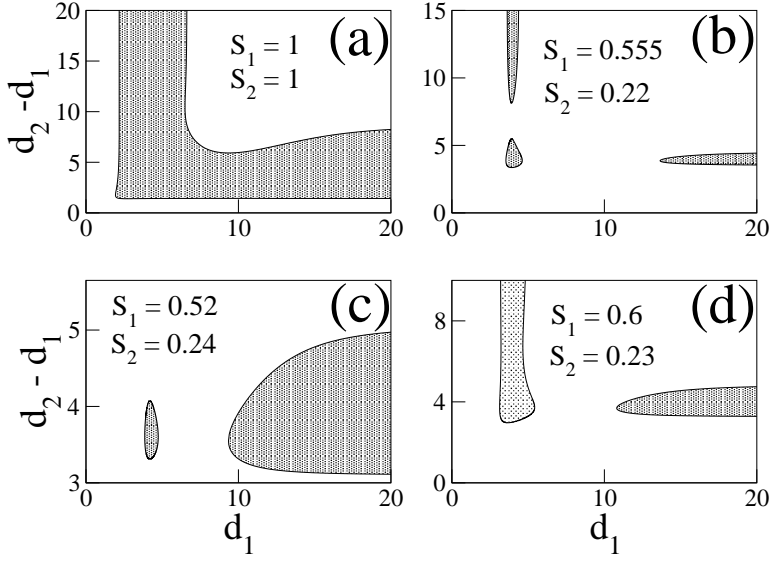


Figure 5.7: Different types of stability diagrams in the plane of the layer thicknesses $(d_1, d_2 - d_1)$, shown for different strength of the short-range interactions S_1 and S_2 as given in the legends. The shaded parts represent linearly stable regions. The Hamaker constants are $A_{12g} = 1.49$, $A_{21s} = 3.8$, $A_{g21s} = -23.02$, corresponding to the Si/PMMA/PS/air system. Panels (a), (b), (c) and (d) correspond to ranges I, III, IV and II in Fig. 5.8, respectively.

short-range interactions. Practically, the latter become important (well) below 10 nm layer thickness. In contrast to the result for the exclusive action of long-range van der Waals forces, in the regime where both, short- and long-range interactions, are important the stability threshold can be crossed by changing the layer thicknesses d_i . Fig. 5.7 presents a selection of qualitatively different stability diagrams in the plane spanned by the layer thicknesses obtained when varying the strength of the short-range interaction for a fixed long-range interaction. By changing the short-range part of the spreading coefficient S_1 and S_2 one finds seven topologically different types of such diagrams. These types correspond to regions in the (S_1, S_2) plane as indicated in Fig. 5.8. In the absolute unstable region bounded on the right by $(S_1)_{\min} = (e/4)^4 A_{21s}/|A_{12g}|$ and above by $(S_2)_{\min} = (e/4)^4$ the system can not be stabilized by changing d_1 or d_2 . Only if at least one of the two S_i is larger than the corresponding criti-

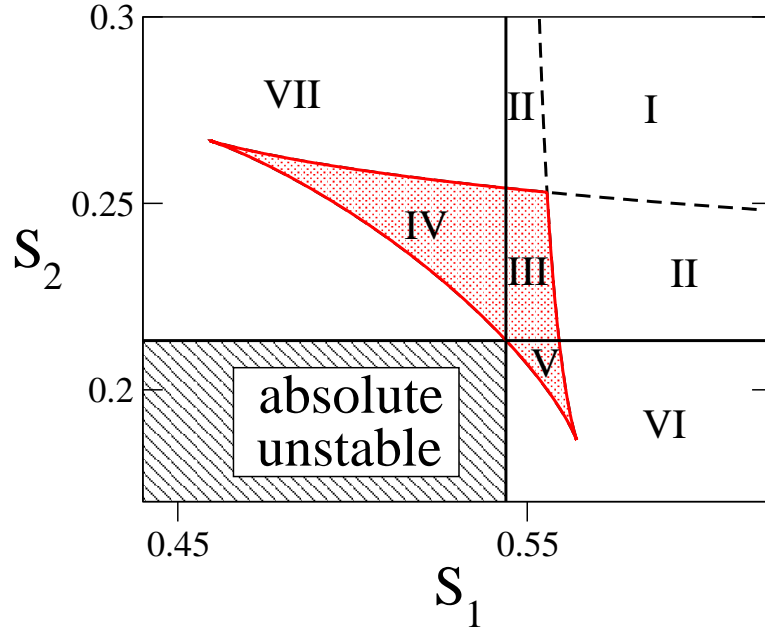


Figure 5.8: Phase diagram in the plane (S_1, S_2) for the $Si/PMMA/PS/air$ system. The absolute stable region (hatched rectangle in the lower left corner) is bounded by $(S_1)_{\min} = (e/4)^4 A_{21s}/|A_{12g}|$ from the right and by $(S_2)_{\min} = (e/4)^4$ from above. The unstable region is divided into seven qualitatively different subregions, described in the main text.

cal value (a) stable region(s) can be found in the $(d_1, d_2 - d_1)$ plane (see Fig. 5.7). For $S_1 > (S_1)_{\min}$ a stable region exists that extends towards infinite $(d_2 - d_1)$, as shown in Figs. 5.7(a), (b) and (d). Thereby, for large $(d_2 - d_1)$ the system is stable for $(d_1)_{\min} < d_1 < (d_1)_{\max}$, where $(d_1)_{\max}$ and $(d_1)_{\min}$ are the solutions of the equation $A_{21s}/|A_{12g}| = S_1 x^4 \exp(-x)$. Similarly, for $S_2 > (S_2)_{\min}$ a stable region exists that extends towards infinite d_1 , as in Figs. 5.7(a) to (d). For large d_1 the system is stable for $(d_2 - d_1)_{\min} < d_2 < (d_2 - d_1)_{\max}$, where $(d_2 - d_1)_{\max}$ and $(d_2 - d_1)_{\min}$ are the solutions of the equation $1 = S_2 x^4 \exp(-x)$. In the gray shaded triangle at the center of Fig. 5.8 an additional bounded stable region exists in the $(d_1, d_2 - d_1)$ plane (see Figs. 5.7(b) and (c)).

Combining the different conditions gives the following seven types of stability diagrams.

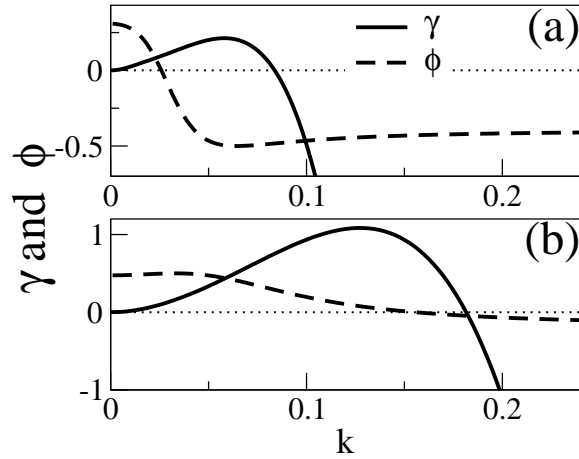


Figure 5.9: Shown are the growth rate γ (solid lines) and the mode type ϕ (dashed lines) of the leading eigenmode. (a) A varicose mode from the one-mode region at $d_1 = 30$, $d_2 = 47$ and $\sigma = \mu = 1$, (b) a zigzag mode from the one-mode region at $d_1 = 15$, $d_2 = 40$ and $\sigma = \mu = 1$.

- I:** The stable region is continuous and extends in respective stripes towards infinite d_1 and $d_2 - d_1$ (Fig. 5.7(a)).
- II:** There exist two separated stable regions, one extending towards infinite d_1 and the other one towards infinite $d_2 - d_1$ (Fig. 5.7(d)).
- III:** Similar to Type II but with an additional bounded stable region (Fig. 5.7(b)).
- IV:** A bounded stable region exists together with an unbounded region extending towards infinite d_1 (Fig. 5.7(c)).
- V:** Similar to type IV but with the unbounded region extending towards infinite $(d_2 - d_1)$ (not shown).
- VI:** Only one stable region exists extending towards infinite d_1 (not shown).
- VII:** Similar to type VI but with the unbounded region extending towards infinite $(d_2 - d_1)$ (not shown).

Further on we will focus our attention on the stability diagram of type I.

5.5.2 Non-uniform stationary solutions

To find periodic stationary solutions of the scaled equations Eqs. (5.19), the time derivatives $\partial_t h_i$ are set to zero. Integration yields

$$\begin{aligned} Q_{11} \partial_x \left(\frac{\delta F}{\delta h_1} \right) + Q_{12} \partial_x \left(\frac{\delta F}{\delta h_2} \right) &= C_1 \\ Q_{21} \partial_x \left(\frac{\delta F}{\delta h_1} \right) + Q_{22} \partial_x \left(\frac{\delta F}{\delta h_2} \right) &= C_2, \end{aligned} \quad (5.34)$$

where the C_i are constants and F is given by Eq. (5.33). Note that the left hand sides of Eq. (5.34) represent the flow in the lower layer and the total flow, respectively. For a stationary state both flows are zero, i.e. the $C_1 = C_2 = 0$. Because the mobility matrix \mathbf{Q} is non-singular, one concludes from Eq. (5.34) that the stationary states of the equations Eqs. (5.19) are the extrema of the Lyapunov functional F , i.e. they are solutions of

$$\begin{aligned} -\partial_{xx} h_1 + \frac{\partial f}{\partial h_1} &= c_1 \\ -\sigma \partial_{xx} h_2 + \frac{\partial f}{\partial h_2} &= c_2, \end{aligned} \quad (5.35)$$

where f denotes the local part of Eq. (5.33) and the constants c_i correspond to the Lagrangian multipliers introduced in Section 5.5. To obtain a finite amplitude solution for given mean thicknesses we use continuation techniques [33, 34, 32]. We start with analytically known stationary periodic small-amplitude profiles, which correspond to the linear eigenfunctions for the critical wave number k_c . By continuation we follow the family of solutions changing the period L . We characterize the solutions by the deflection amplitudes A_1 and A_2 , the energy E , the norm $L_2 = (1/L) \int [(h_1 - d_1)^2 + (h_2 - d_2)^2] dx$ and the integral mode type ϕ_{int} . To determine the stability of the stationary solutions $h_i(x)$, we add small perturbations $\delta h_i(x) \sim \exp(\beta t)$ to both interfaces $h_i(x)$, linearize the full time-dependent evolution equations Eqs. (5.19) around $h_i(x)$ and solve the obtained eigenvalue problem $\mathbf{L}(h_i, \partial_x h_i, \partial_x) \delta \mathbf{h}(x) = \beta \delta \mathbf{h}(x)$ for the linear operator \mathbf{L} after discretizing it in space. The sign of the largest eigenvalue β determines the stability of the stationary solution. Note that due to the

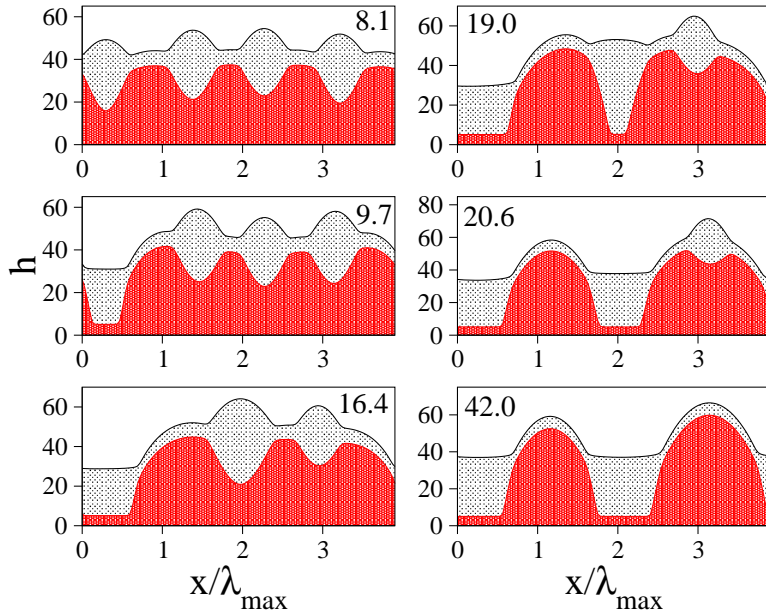


Figure 5.10: *Snapshots of the time evolution of a Si/PMMA/PS/air system for $d_1 = 30, d_2 = 47, S_1 = S_2 = 1, \sigma = 1$ and $\mu = 1$ at times as given in the legends. The domain length is $L = 4\lambda_m$ and time is in units of $1/\gamma_m$.*

translational invariance of the evolution equations Eqs. (5.19), there exists always a symmetry mode $\delta h_i(x) = \partial_x h_i(x)$ with the eigenvalue $\beta = 0$.

5.5.3 Mode-type transitions

The type of the dominant instability mode calculated above by linear stability may not persist in the course of the nonlinear evolution. Possible mode type changes may have a dramatic effect on the (observable) overall morphology of the film. We investigate these changes by studying both, the evolution in time of the film profiles and the stationary solutions obtained by continuation.

The evolution in time is obtained by numerical simulations of the scaled coupled evolution equations Eqs. (5.19) in a one-dimensional periodic domain. Both, semi-implicit pseudo-spectral and explicit time integration schemes are used. Initial conditions consist of flat layers with an imposed noise of

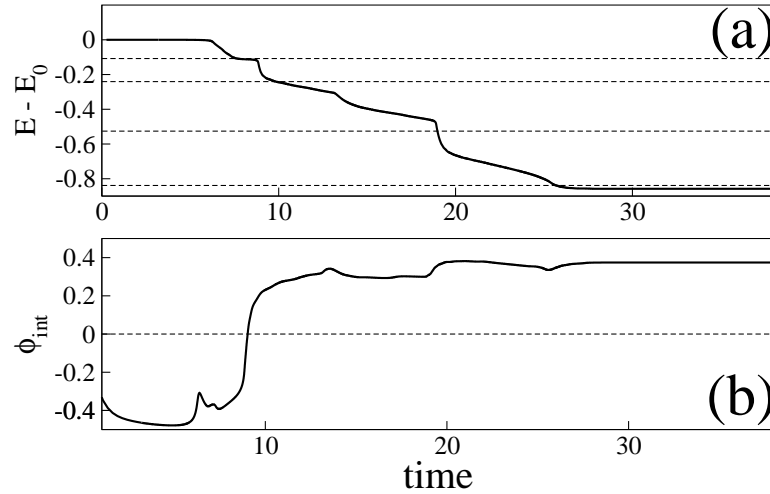


Figure 5.11: Evolution in time of (a) the relative energy $E - E_0$ and (b) the integral mode-type ϕ_{int} Eq. (5.30) for parameters as in Fig. 5.10. Time is in units of $1/\gamma_m$. In (a) the dashed lines denote the energy levels which correspond to the stationary solutions with periods $L = \lambda_m$ (first and second line from above), $L = 4/3\lambda_m$ (third line from above) and $L = 2\lambda_m$ (the lowest line), taken from Fig. 5.12(b).

amplitude 0.001.

Transition via branch switching.

First the time evolution of an initially flat film is studied for parameters as in Fig. 5.9(a) using a domain size equal to four times the fastest growing wave length λ_m . A time sequence of snap shots is shown in Fig. 5.10. In the early stage of the evolution a varicose mode develops ($t = 8.1$) as expected from the linear analysis. Then in a sub-domain of size λ_m the deflection amplitudes increase dramatically accompanied by a morphological change towards a zigzag type profile ($t = 9.7$). This is further illustrated by the dependence of the integral mode-type Eq. (5.30) on time given in Fig. 5.11(b). Further on, the length of the zigzag part increases slightly, and coarsening sets in resulting in the disappearance of one varicose-type drop ($t = 16.4$). Next one of the remaining drops increases its amplitude and flips to a zigzag type hole ($t = 20.6$). Finally the last remaining varicose-type drop disappears ($t \approx 28$), and the system approaches a stationary (but not stable) state. The evolution of the relative energy of the profile in time is given in

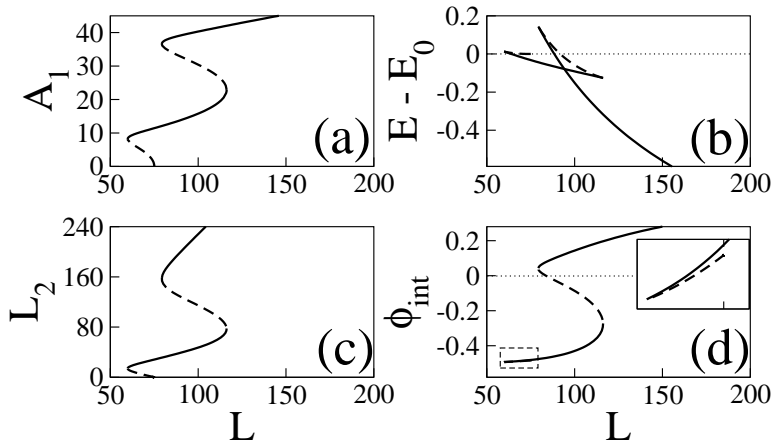


Figure 5.12: *Characterization of the stationary periodic solutions for the system of Fig. 5.11. Shown are (a) the amplitude of the lower layer A_1 , (b) the relative energy $E - E_0$, (c) the norm L_2 , and (d) the integral mode type ϕ_{int} in their dependence on the period L . In (d) the inset shows a zoom of the region marked by the dashed box.*

Fig. 5.11(a). It is seen very clearly that the phases of very slow evolution correspond to solutions that are close to stationary solutions. This results from the fact that the (unstable) stationary solutions form saddle points in function space that are approached along their stable manifolds and subsequently repel the system along their unstable manifolds (for a discussion see Ref. [121]) The evolution stops after a further coarsening step, when the period becomes equal to the system size (not shown).

To explain the observed mode-type change, we study the stationary solutions of the evolution equations Eqs. (5.19). We find a family of solutions starting at the subcritical primary bifurcation, then turning three times at saddle-node bifurcations (folds) and going towards infinite periods (see Fig. 5.12(a)). A stability analysis using the solution period as the period of the disturbance (thereby excluding coarsening modes) shows that two branches are stable (solid lines) and two are unstable (dashed lines). Along the first unstable branch, which starts at L_c and ends at the first fold at $L \approx 60$ the energy E is always larger than the one of the flat film E_0 (Fig. 5.12(b)), and it increases with decreasing period. This subcritical branch corresponds to nucleation

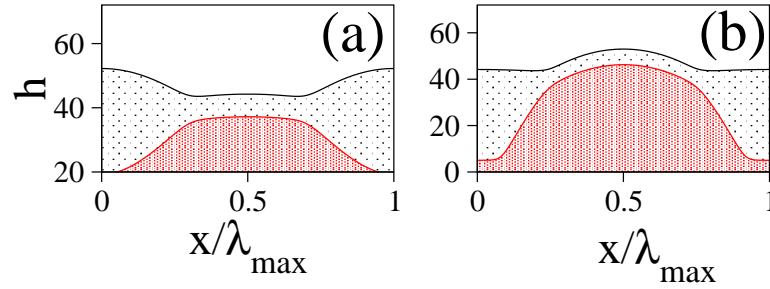


Figure 5.13: *The two stationary solutions with period $L = 108.28$ (cp. Fig. 5.12) corresponding to the wave length of the relevant dominant linear mode λ_{max} . Shown are (a) the varicose type and (b) the zigzag type solution from the first and second stable branch, respectively.*

solutions that have to be overcome to break the film in parts smaller than L_c (see Ref. [126] for a discussion of this type of solutions for a one-layer system). The first stable branch starts at the first fold at $L \approx 59$ and ends at the second fold at $L \approx 116$. Its relative energy decreases monotonically with increasing period. Mostly it is energetically preferable to the flat film. The second unstable branch (between the second fold at $L \approx 116$ and the third fold at $L \approx 79$) turns back towards smaller periods. The second stable branch starts at the third fold and goes towards infinite periods. Its energy decreases rapidly from values even above the flat film to values below the ones of the first stable branch. The energy of the second unstable branch is always larger than the energies of both stable branches. This indicates that it corresponds to nucleation solutions, or critical solutions that have to be overcome to switch between the two stable branches. Along the second unstable branch, the mode-type changes from varicose to zigzag (Fig. 5.12 (d)) explaining the non-trivial behavior observed in the time evolution shown in Fig. 5.10. There are two stable solutions with a period equal to the dominant linear wave length ($\lambda_m \approx 108$) (see Fig. 5.13). The one of higher energy that is approached first in the time evolution is of varicose type whereas the one of lower energy that the system switches to is of zigzag type (cp. Fig. 5.12(b)). A transition between the two solutions is accompanied by a strong increase of the amplitude A_1 (see Fig. 5.12(a)).

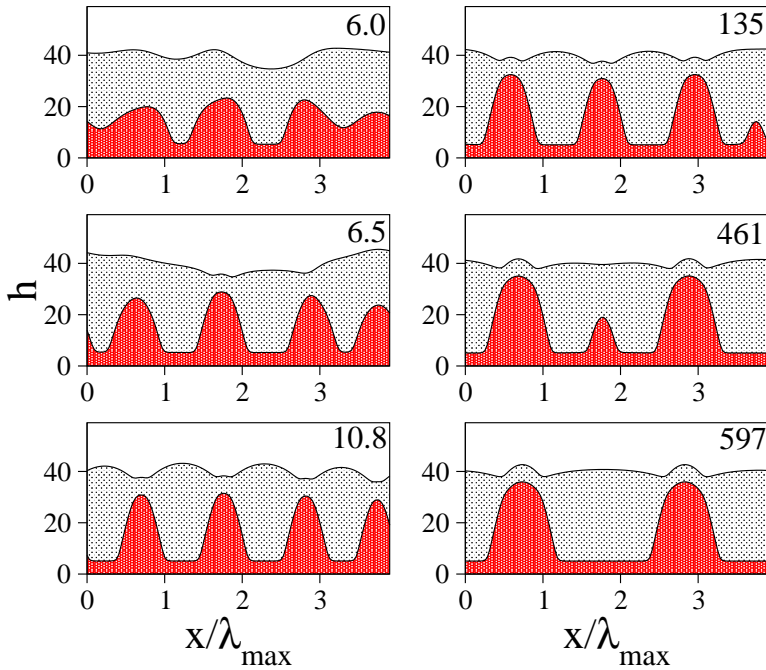


Figure 5.14: Snapshots of the time evolution of a Si/PMMA/PS/air system for $d_1 = 15$, $d_2 = 40$, $S_1 = S_2 = 1$, $\sigma = 1$ and $\mu = 1$ at times as given in the legends. The domain length is $L = 4\lambda_m$ and time is in units of $1/\gamma_m$.

Transition via coarsening.

A mode-type change is not always connected to a transition between different branches of stationary solutions. Also coarsening along one branch may lead to such a change if the mode-type varies along the branch. To demonstrate this, we simulate the time evolution using parameters as in Fig. 5.9(b). A time sequence of profiles and the corresponding evolution of the relative energy and the integral mode-type are shown in Figs. 5.14 and 5.15, respectively. Early in the evolution the layer profiles represent a zigzag mode ($t = 6.0$) corresponding to the linear results (Fig. 5.9(b)). Then, within the very short period of time from $t = 6.0$ to 10.8, nonlinear effects result in a first change towards a varicose type profile, as shown in the inset of Fig. 5.15(b). Then the system approaches the branch of stationary solutions. As a result the evolution slows down and the pattern begins to coarsen. With ongoing coarsening ($t > 10.8$) the size of the droplets increases

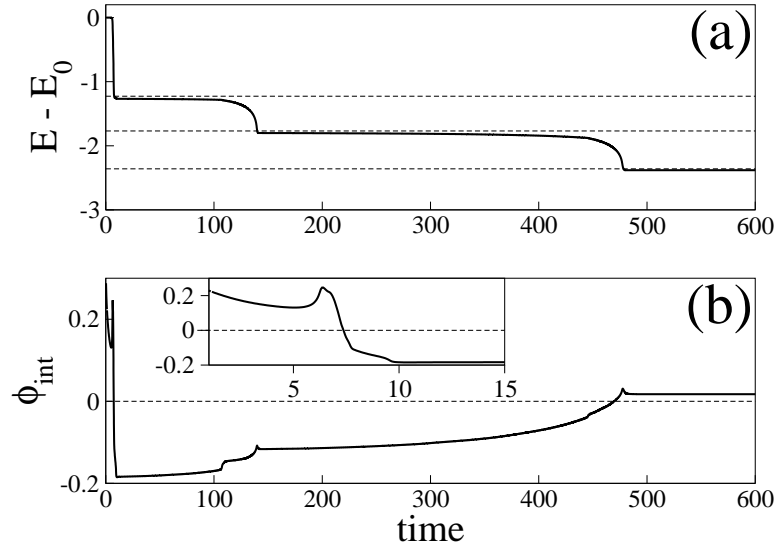


Figure 5.15: *Evolution in time of (a) the relative energy $E - E_0$ and (b) the integral mode-type ϕ_{int} (Eq. 5.30) for parameters as in Fig. 5.14. The inset in (b) shows the early-time behaviour of the mode-type. Time is in units of $1/\gamma_m$. In (a) the dashed lines denote the energy levels which correspond to the stationary solutions with periods $L = \lambda_m$, $L = 4/3\lambda_m$ and $L = 2\lambda_m$, taken from Fig. 5.16(b).*

($t = 135$, $t = 461$) and at very late times ($t > 490$) the mode type changes back to zigzag type (Fig. 5.15(b)). Here, the amplitudes of the interfaces do not change dramatically, as was the case for the transition via branch switching. In this sense the transition is continuous.

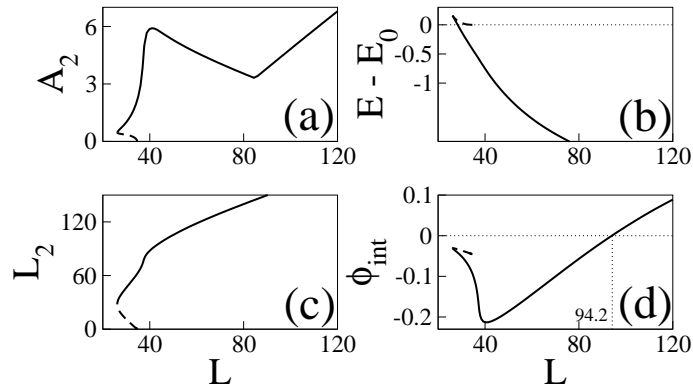


Figure 5.16: Characterization of the stationary periodic solutions, for the system of Fig. 5.14. Shown are (a) the amplitude of the upper layer A_2 , (b) the relative energy $E - E_0$, (c) the norm L_2 and (d) the integral mode type ϕ_{int} in their dependence on the period L .

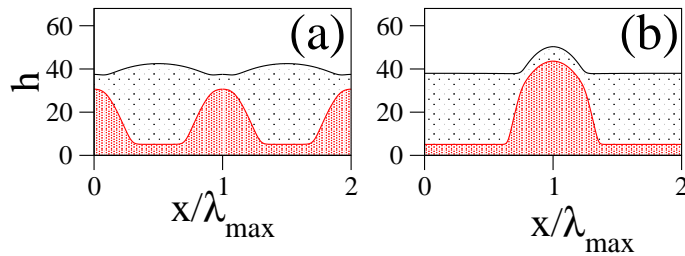


Figure 5.17: The two stationary solutions with period $L = 50.8$ and $L = 101.6$ (cp. Fig. 5.16) corresponding to once and twice the wave length of the dominant linear mode λ_{max} , respectively. To symbolize the coarsening process we show in (a) and (b) two and one period(s), respectively. The x coordinate is in units of λ_{max} .

The characteristics of the corresponding stationary solutions are shown in Fig. 5.16. The primary bifurcation is again subcritical (Fig. 5.16(a)) the solution family continues towards smaller periods until turning at a saddle-node bifurcation (fold) and heading towards infinite periods. The subcritical branch is unstable with energies higher than the energy of the flat film (Fig. 5.16(b)). The second branch starting at the fold ($L \approx 26$) consists of solutions whose energy decreases monotonically with increasing period. They are stable to disturbances of identical period but unstable to coarsening modes. Fig. 5.16 (d) shows that the solution with the period equal to $\lambda_m = 50.81$ is of varicose type. The corresponding layer profile is shown in Fig. 5.17(a) together with the profile after the first coarsening step. When the period becomes larger than 94.2, the solution changes to zigzag type (Fig. 5.16(d)) as shown in Fig. 5.17(b). This explains the mode-type change found in the time evolution (Fig. 5.14).

Here we have restricted our attention to a parameter set corresponding to region I of Fig. 5.8, i.e. corresponding to the stability diagram shown in Fig. 5.7 (a). The existence of a stable branch of stationary solutions which continues towards infinite period implies that the rupture of the two layers is completely avoided by the short-range repulsion. However, this may not be the case for parameter ranges belonging to the other types of stability diagrams. A detailed analysis of the stationary solutions for all types will be done elsewhere.

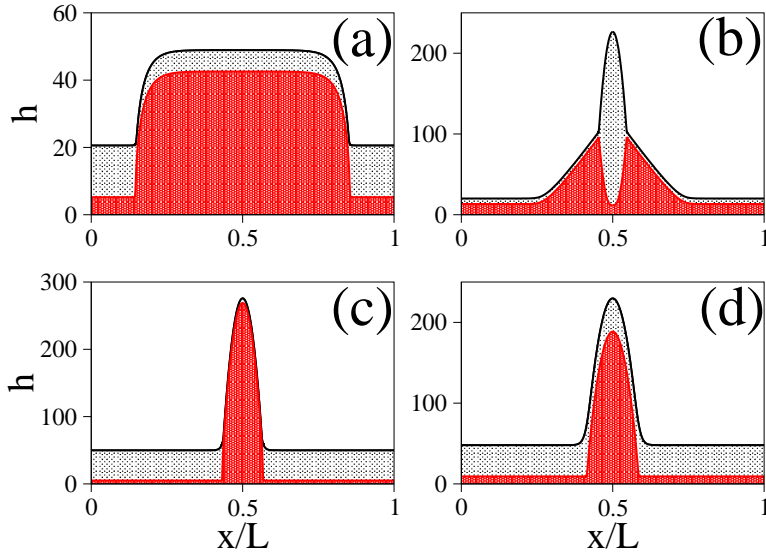


Figure 5.18: Large-period (long-time) stationary profiles for (a) a Si/PMMA/PS/air system with $d_1 = 30$, $d_2 = 39$, $\lambda_m = 132$ and period $L = 26 \times \lambda_m$, (b) a SiO/PMMA/PS/air with $d_1 = 30$, $d_2 = 50$, $\lambda_m = 246$ and period $L = 20 \times \lambda_m$, (c) a Si/PMMA/PS/air system with $d_1 = 30$, $d_2 = 70$, $\lambda_m = 118$ and $L = 21 \times \lambda_m$ and (d) a SiO/PS/PDMS/air with $d_1 = 30$, $d_2 = 70$, $\lambda_m = 557$ and $L = 10 \times \lambda_m$. The remaining parameters are $\sigma = 1$, $\mu = 1$, and $S_1 = S_2 = 1$.

5.5.4 Large-period stationary solutions

The stability of the numerical code, used to solve the evolution equations Eq. (5.19), requires a very small time step $t = 0.00001$. As a result it takes very long even to reach the final stationary solution in a system of size $4\lambda_m$ using 256 grid points. It is not feasible at the moment to study many coarsening steps in this way. However, one can rely on continuation techniques that use an adaptive spatial grid along the continuation path [32] to obtain stationary solutions of arbitrarily large periods that correspond to solutions that would be obtained in a time evolution at very late times. We show in Fig. 5.18 possible large-period stationary solutions for different physical systems that are investigated experimentally. One finds qualitatively different morphologies like a drop of the lower liquid 'looking through' a nearly flat

film of the upper layer for a Si/PMMA/PS/air system. Note however that also the upper layer is continuous (due to the stabilizing short-range interaction), i.e. also the drop is covered by a very thin layer of the upper liquid. This is more pronounced for a SiO/PS/PDMS/air system. In contrast, for a SiO/PMMA/PS/air system one finds a drop of the upper liquid 'swimming' on the lower liquid that however is attracted towards the base of the drop. These equilibrium solutions are equivalents of drop configurations studied in Ref. [64] for macroscopic (but smaller than the capillary length) drops. However, here the mesoscopic contact angles are not given explicitly but result from the underlying effective molecular interactions, i.e. the short- and long-range forces used.

Speaking about further development of the two-layer films theory, the Marangoni effect should be taken into account. This will give rise to even more complex behavior accompanied by the appearance of the oscillatory modes. Besides, the 3D simulations of the time evolution of both ultra thin and Marangoni films should be performed. The 3D time evolution will show the coupling of the mode type to the 3D surface morphology. Speculating on the mode type change, one can suppose that it could be related to the drop-hole or hole-drop transition.

Chapter 6

Conclusion

Here we summarize all the results obtained in the previous chapters. To be consequent, we start with one-layer films.

One-layer films: large-scale Marangoni convection. In Section 4.2 we have studied a thin liquid with a free surface heated from below. We have considered the case where the fluid is unstable due to the Marangoni effect against large scale surface deformation but small scale convection cannot occur. To describe pattern formation under this circumstances, we have used the lubrication approximation and concentrated on the properties and solutions of the thin film equation, derived from the basic set of hydrodynamic equations. In addition to previous work our description includes a repelling van der Waals term as disjoining pressure which accounts for stabilization of extremely thin fluid layers of 10 to 100 nm height. Rupture of the film corresponding to a finite time singularity of the thin film equation without disjoining pressure [81, 82, 79] is now avoided and the spatio-temporal evolution of surface patterns can be studied in the long time domain. Instead of forming completely dry regions, the substrate remains now always covered with such a thin fluid layer or the precursor film.

The linearized problem and the energy method allows for computation of the stability regions of (circular) drops, holes, or fronts with respect to the vertically applied temperature gradient and the mean film thickness. We

have shown that on very thin films drops always evolve at onset. For thicker films, we predict the formation of holes at onset which then, upon increasing the Marangoni number, give way to drops. We note that drops, or at least one big drop on a rather thick film was found in the experiments by VAN HOOK ET AL. [131] for an air layer, instead of holes for an helium gas layer above a silicone oil film. The thermal properties of the gas layer influences the Biot number and also the Marangoni number. It seems possible that the Helium experiment was performed closer to threshold than the one with the air layer. According to our stability analysis this explains the patterns observed.

We have also studied the film behavior in three spatial dimensions, solving the two-dimensional film equation numerically. We have found holes, drops and mazes for several parameter settings. An exponential scaling law of the wavelength has been extracted from the numerical runs. We found an independent scaling factor with respect to the Hamaker constant close to threshold. The scaling law $k \sim t^{-\beta}$ with $\beta = 0.21 \pm 0.01$ indicates that the coarsening is slower than in spinodal decomposition, where $\beta = 1/3$ as given by the Lifshitz-Slyozov-Wagner theory (see for example [59]). The inclusion of hydrodynamic effects in the description of spinodal decomposition gives even larger exponents for the long time limit (in 2D case: $\beta = 1/2$ viscosity controlled, $\beta = 2/3$ inertia controlled [90]).

The exponent found here is similar to $\beta = 0.22$ found in numerical simulations for spinodal decomposition with a mobility that depends strongly on concentration implying the prevalence of surface diffusion over bulk diffusion [56]. A scaling argument for this case yields $\beta = 1/4$ [56]. To our knowledge for spinodal dewetting there exist no analytical or numerical results for the scaling exponent in two dimensions (for one dimension see [40]).

Finally we have turned to the case of a slightly inclined layer under gravitation. Here we have demonstrated the influence of inclination on the dynamical scaling as well as on the formation of front instabilities and fingers. The found transversal instabilities of leading and trailing edges of elevated regions or liquid ridges show behavior reminiscent of the front and back

instabilities of liquid ridges on an inclined plane studied in [122, 125]. Especially, it should be noted that the instabilities at the trailing and leading edge are seemingly independent corresponding to the decoupled regime in [122]. The wavenumber at the back is also nearly twice as large as the one at the front. The studied system could be especially suited to investigate the fingering at the back experimentally, because following the analogy with the results of [122] the destabilizing influence for the transversal instability is given by the heating. The heating can be exactly controlled and changed experimentally and so its influence on the characteristics of the instability can be investigated directly. On the contrary the destabilizing influence in [122] is the long-range part of the disjoining pressure that is difficult to control.

Finally we mention that to our knowledge there exists no theory for the mechanism of nonlinear wavelength selection and stabilization of a periodic structure in the inclined case, which can be clearly seen from our numerical simulations.

One-layer films: external disturbance, inhomogeneous wetting. The influence of external modulation on pattern formation in thin liquid films has been discussed in Section 4.3. Two different mechanisms have been studied: a non-contact method using irradiation of the liquid surface with ultrasound allows for manipulation of drops, holes or fronts in a prescribed way. Moreover, spatially periodic surface structures with desired wave length may be generated in the long-time limit. The second mechanism is based on inhomogeneous wetting properties of the solid substrate. Here, beneath the amplitude of the modulation the ratio between the two intrinsic length scales, namely the spinodal wave length and the wave length of the modulation, plays a crucial role. We showed by direct numerical integration of a model that, depending on that ratio, pinning or coarsening is the dominant dynamical behavior. The alignment of the eventually stable surface structures is also strongly influenced by this ratio.

Although both mechanisms are completely different, the resulting patterns show certain common features which have to be explored in more detail

in future work. In both systems, the rotational symmetry in the horizontal plane is broken by the external modulation. This lack of symmetry expresses itself in the form of the final stable surface pattern, which has turned out to be periodic in both cases. Interestingly, in both cases the surface pattern can be organized in stripes perpendicular to the external force or modulation. Coarsening, obtained always in the early stages of temporal evolution, is interrupted at a certain time and periodic patterns stabilize. The periodicity length depends thereby mainly on the strength of the external modulation.

Two-layer films. We proceed now with the concluding remarks on two-layer films. In Chapter 5, we have derived coupled non-linear evolution equations for the profiles of the liquid-liquid and the liquid-gas interface of a thin two-layer liquid film heated from below allowing for slip at the substrate. We have shown that in the isothermal case the evolution equations can be written in terms of variations of an appropriate Lyapunov functional F which monotonically decreases in time. The stability conditions for flat layers have been given in terms of F . We have shown that a two-layer film is less stable than related effective one-layer films introduced in Section 5.4.2. Even if both effective one-layer films are stable the two-layer film may be unstable if the determinant of the energy matrix \mathbf{E} is negative.

We have shown that if the Hamaker constants are given by the usual expression (equation Eq. (3.11)), i.e. they are coupled through the refractive indices, and no other forces are present, the stability of the flat films with thicknesses of (~ 100 nm) can not be changed by solely changing the layer thicknesses. Incorporating a stabilizing short-range interaction the stability can be changed in this way. We have classified the resulting possible types of stability diagrams in the space of the layer thicknesses and given a 'phase diagram' in terms of the short-range parts of the spreading coefficients for the occurrence of the different types of stability diagrams.

In general, the linear stability analysis of the flat film has shown that both, varicose or zigzag mode, may be unstable depending on the ratios of the layer thicknesses, viscosities and surface tensions. If the driving forces are represented by long-range interaction only, the two instability modes lead

to rupture at the substrate or the liquid-liquid interface. This seems to be in contrast to Ref. [13]. However, the difference arises because there it is assumed that the lower layer is thick compared to the upper layer neglecting thereby all interactions with the substrate. Then the zigzag mode is always stable. Remarkably, the faster layer accelerates the evolution of the slower layer even if the latter is rather thick implying that its rupture time may be shortened by orders of magnitude.

The introduction of the stabilizing short-range interaction has allowed to study the long-time evolution and stationary layer profiles. Possible stationary states have then been determined as extrema of the Lyapunov functional F . The resulting bifurcation diagrams show a rich branch structure that depends strongly on parameter values. We have focused on one type of stability diagram where a stable branch going towards infinite period always exists. This implies the existence of a non-ruptured stationary state in the long-time limit also in the time evolution.

We have found that the mode type of a profile may change during the evolution of an instability in three different ways. First, the profile type may change in the course of the short-time evolution. This is related to different mode types found for the dominant linear flat film mode and for the stationary solution of equal period on the solution branch approached first in the time evolution. It seems that this behavior is more probable for a subcritical primary bifurcation. In the case studied here this change is from zigzag to varicose type. In the nonlinear regime the profile can change its type by (i) jumping from one to another stable branch and by (ii) coarsening along a single stable branch. Combinations of the different ways may also be possible. We have found that for the parameters considered here both nonlinear transitions go from varicose towards zigzag type. In case (i) the transition occurs without change of the period, but with a dramatic increase in amplitude of the profile. In the case (ii) the transition occurs continuously without amplitude jump because mediated by coarsening a small-period varicose mode turns into a large-period zigzag one.

In all examples considered here (except the SiO/PMMA/PS/air system with

$d_1 = 30, d_2 = 50$) we have found a zigzag-type solution at large periods. For the future it would be very interesting to further analyze the stationary solutions for a broader range of experimentally interesting systems like the ones studied in Refs. [71, 84]. This should clarify under which conditions the long-time (or large-period) solutions are energetically preferable and determine how 'late' the transition may occur. A systematic analysis of all types of stability diagrams would also discuss metastability and absolute stability of the flat two-layer films. Furthermore, we are very optimistic that the evolution equations presented here will serve to study the questions of hole growth and possible front instabilities in the dewetting of a liquid layer on a liquid substrate of finite thickness [37, 84].

Bibliography

- [1] D. Bandyopadhyay. Stability and dynamics of bilayers, 2001. Master-thesis, Dep. Chem. Eng., Ind. Inst. Tech. Kanpur.
- [2] D. Bandyopadhyay, R. Gulabani, and A. Sharma. Instability and dynamics of thin liquid bilayers. *Ind. Eng. Chem. Res.*, 44:1259–1272, 2005.
- [3] A. L. Bertozzi, G. Grün, and T. P. Witelski. Dewetting films: Bifurcations and concentrations. *Nonlinearity*, 14:1569–1592, 2001.
- [4] A. L. Bertozzi, A. Münch, X. Fanton, and A. M. Cazabat. Contact line stability and "undercompressive shocks" in driven thin film flow. *Phys. Rev. Lett.*, 81:5169–5173, 1998.
- [5] M. Bestehorn. Phase and amplitude instabilities for Bénard-Marangoni convection in fluid layers with large aspect ratio. *Phys. Rev. E*, 48:3622–3634, 1993.
- [6] M. Bestehorn. Square patterns in Bénard-Marangoni convection. *Phys. Rev. Lett.*, 76(1):46–49, 1996.
- [7] M. Bestehorn and K. Neuffer. Surface patterns of laterally extended thin liquid films in three dimensions. *Phys. Rev. Lett.*, 87:046101,1–4, 2001.
- [8] M. Bestehorn and Pérez-García. Coexistence of patterns with different symmetries in Bénard-Marangoni-convection. *Europhys. Lett.*, 4:1365, 1987.

- [9] M. Bestehorn, A. Pototsky, and U. Thiele. 3D large scale Marangoni convection in liquid films. *Eur. Phys. J. B*, 33:457–467, 2003.
- [10] J. Bischof, D. Scherer, S. Herminghaus, and P. Leiderer. Dewetting modes of thin metallic films: Nucleation of holes and spinodal dewetting. *Phys. Rev. Lett.*, 77:1536–1539, 1996.
- [11] W. Boos and A. Thess. Cascade of structures in long-wavelength Marangoni instability. *Phys. Fluids*, 11:1484–1494, 1999.
- [12] F. Brochard-Wyart and P.-G. de Gennes. Dewetting of a water film between a solid and a rubber. *J. Phys.: Cond. Mat*, 6:A9–12, 1993.
- [13] F. Brochard-Wyart, P. Martin, and C. Redon. Liquid/liquid dewetting. *Langmuir*, 9:3682–3690, 1993.
- [14] L. Bruschi, H. Kühne, U. Thiele, and M. Bär. Dewetting of thin films on heterogeneous substrates: Pinning vs. coarsening. *Phys. Rev. E*, 66:011602, 1–5, 2002.
- [15] J. P. Burelbach, S. G. Bankoff, and S. H. Davis. Nonlinear stability of evaporating/condensing liquid films. *J. Fluid Mech.*, 195:463–494, 1988.
- [16] J. W. Cahn. Phase separation by spinodal decomposition in isotropic systems. *J. Chem. Phys.*, 42:93–99, 1965.
- [17] J. W. Cahn and J. E. Hilliard. Free energy of a nonuniform system. 1. Interfacial free energy. *J. Chem. Phys.*, 28:258–267, 1958.
- [18] H. B. G. Casimir. *Proc. Kon. Ned. Akad. Wetensch. B51*, 793, 1948.
- [19] A. M. Cazabat, F. Heslot, S. M. Troian, and P. Carles. Fingering instability of thin spreading films driven by temperature gradients. *Nature*, 346:824–826, 1990.
- [20] D. R. Clarke and M. L. Gee. *Material Interfaces, Chap.8: Wetting of surfaces and grain boundaries*. London, 1992.

- [21] R. V. Craster and O. K. Matar. Surfactant transport on mucus films. *J. Fluid Mech.*, 425:235–258, 2000.
- [22] M. C. Cross and P. C. Hohenberg. Pattern formation out of equilibrium. *Rev. Mod. Phys.*, 65:851–1112, 1993.
- [23] K. D. Danov, V. N. Paunov, N. Alleborn, H. Raszillier, and F. Durst. Stability of evaporating two-layered liquid film in the presence of surfactant - I. The equations of lubrication approximation. *Chem. Eng. Sci.*, 53:2809–2822, 1998.
- [24] K. D. Danov, V. N. Paunov, S. D. Stoyanov, N. Alleborn, H. Raszillier, and F. Durst. Stability of evaporating two-layered liquid film in the presence of surfactant - ii. linear analysis. *Chem. Eng. Sci.*, 53:2823–2837, 1998.
- [25] A. A. Darhuber, S. M. Troian, and W. W. Reisner. Dynamics of capillary spreading along hydrophilic microstripes. *Phys. Rev. E*, 6403:031603, 2001.
- [26] M. O. David, G. Reiter, T. Sitthai, and J. Schultz. Deformation of a glassy polymer film by long-range intermolecular forces. *Langmuir*, 14:5667–5672, 1998.
- [27] P.-G. de Gennes. Wetting: Statistics and dynamics. *Rev. Mod. Phys.*, 57:827–863, 1985.
- [28] P. J. W. Debye. Die van der Waalsschen Kohäsionkräfte. *Phys. Z*, 21:178–187, 1920.
- [29] R. J. Deissler and A. Oron. Stable localized patterns in thin liquid films. *Phys. Rev. Lett.*, 68:2948–2951, 1992.
- [30] B. V. Derjaguin and L. D. Landau. Theory of the stability of strongly charged lyophobic sols and of the adhesion of strongly charged particles in solutions of electrolytes. *Acta Physicochim. U.R.S.S.*, 14:633–662, 1941.

- [31] J. A. Diez and L. Kondic. Contact line instabilities of thin liquid films. *Phys. Rev. Lett.*, 86:632–635, 2001.
- [32] E. Doedel, A. Champneys, T. Fairfrieve, Y. Kusnetzov, B. Sandstede, and X. Wang. *Continuation and Bifurcation Software for Ordinary Differential Equations*. Concordia University, Montreal, 1997.
- [33] E. Doedel, H. B. Keller, and J. P. Kernevez. Numerical analysis and control of bifurcation problems (I) Bifurcation in finite dimensions. *Int. J. Bif. Chaos*, 1:493–520, 1991.
- [34] E. Doedel, H. B. Keller, and J. P. Kernevez. Numerical analysis and control of bifurcation problems (II) Bifurcation in infinite dimensions. *Int. J. Bif. Chaos*, 1:745–72, 1991.
- [35] I. E. Dzyaloshinskii, E. M. Lifshitz, and L. P. Pitaevskii. *Adv. Phys.*, 10:165, 1961.
- [36] L. Euler. *Foundations of Differential Calculus*. Springer-Verlag, New York, translation of first nine chapters of *institutiones calculi differentialis*, published in 1755 edition, 2000.
- [37] A. Faldi, R. J. Composto, and K. I. Winey. Unstable polymer bilayers. 1. Morphology of dewetting. *Langmuir*, 11:4855, 1995.
- [38] L. S. Fisher and A. A. Golovin. Nonlinear stability analysis of a two-layer thin liquid film: Dewetting and autophobic behavior. *J. Colloid Interface Sci.*, 291 (2):515–528, 2005.
- [39] N. Garnier, R. O. Grigoriev, and Schatz M. F. Optical manipulation of microscale fluid flow. *Phys. Rev. Lett.*, 91:054501, 2003.
- [40] K. B. Glaser and T. P. Witelski. Coarsening dynamics of dewetting films. *Phys. Rev. E*, 67:016302, 2003.
- [41] A. A. Golovin and L. S. Fisher. private communication.
- [42] A. A. Golovin, A. A. Nepomnyashchy, and L. M. Pismen. Interaction between short-scale Marangoni convection and long-scale deformational instability. *Phys. Fluids*, 6:34–48, 1994.

- [43] A. A. Golovin, A. A. Nepomnyashchy, L. M. Pismen, and H. Riecke. Steady and oscillatory side-band instabilities in Marangoni convection with deformable interface. *Physica D*, 106:131–147, 1997.
- [44] R. O. Grigoriev. Contact line instability and pattern selection in thermally driven liquid films. *Phys. Fluids*, 15:1363, 2003.
- [45] R. J. Hunter. *Foundation of Colloid Science*, volume 1. Clarendon Press, Oxford, 1992.
- [46] J. N. Israelachvili. The calculation of Van der Waals dispersion forces between macroscopic bodies. *Proc. R. Soc. Lond. A*, 331:39–55, 1972.
- [47] J. N. Israelachvili. *Intermolecular and Surface Forces*. Academic Press, London, 1992.
- [48] K. Jacobs, R. Seemann, G. Schatz, and S. Herminghaus. Growth of holes in liquid films with partial slippage. *Langmuir*, 14:4961, 1998.
- [49] T. B. Jones and M. P. Perry. Electrodynamic heat pipe experiments. *J. Appl. Phys.*, 45:2129, 1974.
- [50] K. Kargupta, R. Konnur, and A. Sharma. Spontaneous dewetting and ordered patterns in evaporating thin liquid films on homogeneous and heterogeneous substrates. *Langmuir*, 17:1294–1305, 2001.
- [51] K. Kargupta and A. Sharma. Templating of thin films induced by dewetting on patterned surfaces. *Phys. Rev. Lett.*, 86:4536–4539, 2001.
- [52] D. E. Kataoka and S. E. Troian. Patterning liquid flow on the microscopic scale. *Nature*, 402:794, 1999.
- [53] W. H. Keesom. *Proc. R. Acad. Sci. Amsterdam*, 18:636, 1915.
- [54] R. Khanna, A.T. Jameel, and A. Sharma. Stability and breakup of thin polar films on coated substrates: Relationship to macroscopic parameters of wetting. *Ind. Eng. Chem. Res.*, 35:3081–3092, 1996.
- [55] E. Knobloch. Pattern selection in long-wavelength convection. *Physica D*, 41:450–479, 1990.

- [56] A. M. Lacasta, A. Hernández-Machado, J. M. Sancho, and R. Toral. Domain growth in binary mixtures at low temperatures. *Phys. Rev. B*, 45:5276–5281, 1992.
- [57] P. Lambooy, K. C. Phelan, O. Haugg, and G. Krausch. Dewetting at the liquid-liquid interface. *Phys. Rev. Lett.*, 76:1110–1113, 1996.
- [58] L. D. Landau and E. M. Lifshitz. *Hydrodynamik*. Akademie-Verlag, 1979, Berlin.
- [59] J. S. Langer. *An introduction to the kinetics of first-order phase transitions*, chapter 3, pages 297–363. 1992.
- [60] E. M. Lifshitz. *Zh. Eksp. Teor. Fiz.*, 29:894, 1955.
- [61] Z. Q. Lin, T. Kerle, S. M. Baker, D. A. Hoagland, E. Schäffer, U. Steiner, and T. P. Russell. Electric field induced instabilities at liquid/liquid interfaces. *J. Chem. Phys.*, 114:2377–2381, 2001.
- [62] Z. Q. Lin, T. Kerle, T. P. Russell, E. Schäffer, and U. Steiner. Structure formation at the interface of liquid liquid bilayer in electric field. *Macromolecules*, 35:3971–3976, 2002.
- [63] F. London. *Phys. Z*, 63:245, 1930.
- [64] L. Mahadevan, M. Adda-Bedia, and Y. Pomeau. Four-phase merging in sessile compound drops. *J. Fluid Mech.*, 451:411–420, 2002.
- [65] E. S. Manteuffel and K. Vettters. *Lineare Algebra*. Teubner Verlagsgesellschaft, Leipzig, 1972.
- [66] P. Martin, A. Buguin, and F. Brochard-Wyart. *Europhys. Lett.*, 28:421, 1994.
- [67] O. K. Matar, R. V. Craster, and M. R. E. Warner. Surfactant transport on highly viscous surface films. *J. Fluid Mech.*, 466:85–111, 2002.
- [68] A. D. McLachlan. *Proc. R. Soc. London A.*, 271:387, 1963.
- [69] D. Merkt, A. Pototsky, M. Bestehorn, and U. Thiele. *Phys. Fluids*, 2005. (submitted).

- [70] V. S. Mitlin. Dewetting of solid surface: Analogy with spinodal decomposition. *J. Colloid Interface Sci.*, 156:491–497, 1993.
- [71] M. D. Morariu, E. Schäffer, and U. Steiner. Capillary instabilities by actuation induced forces. *Eur. Phys. J. E*, 12:375–381, 2003.
- [72] M. D. Morariu, E. Schäffer, and U. Steiner. Molecular forces caused by the confinement of thermal noise. *Phys. Rev. Lett.*, 92:156102, 2004.
- [73] A. A. Nepomnyashchii and I. B. Simanovskii. Long-wave thermocapillary convection in layers with deformable interfaces. *Pmm-J. Appl. Math. Mech.*, 54:490–496, 1990.
- [74] A. A. Nepomnyashchii and I. B. Simanovskii. New types of long-wave oscillatory Marangoni instabilities in multilayer systems. *Q. J. Mech. Appl. Math.*, 50:149–163, 1997.
- [75] I. Newton. *Opticks*. G. Bell & Sons LTD., London, 1931 (reprinted 4th ed. 1730).
- [76] B. W. Ninham and V. A. Parsegian. Van der Waals forces across triple-layer films. *J. Chem. Phys.*, 52:4578, 1970.
- [77] H. Ohshima. Diffusive double layer interaction between two parallel plates with constant surface charge density in an electrolyte solution. I. Interaction between similar plates. II. Dissimilar plates. *Colloid Polym. Sci.*, 252:158, 257, 1974.
- [78] A. Oron. Nonlinear dynamics of irradiated thin volatile liquid films. *Phys. Fluids*, 12:29–41, 2000.
- [79] A. Oron. Three-dimensional nonlinear dynamics of thin liquid films. *Phys. Rev. Lett.*, 85:2108–2111, 2000.
- [80] A. Oron, S. H. Davis, and S. G. Bankoff. Long-scale evolution of thin liquid films. *Rev. Mod. Phys.*, 69:931–980, 1997.
- [81] A. Oron and P. Rosenau. Formation of patterns induced by thermocapillarity and gravity. *J. Physique II France*, 2:131–146, 1992.

- [82] A. Oron and P. Rosenau. On a nonlinear thermocapillary effect in thin liquid layers. *J. Fluid Mech.*, 273:361–374, 1994.
- [83] C. J. Van Oss, M. K. Chaudhury, and R. J. Good. Interfacial Lifshitz-van der Waals and polar interactions in macroscopic systems. *Chem. Rev.*, 88:927, 1988.
- [84] Q. Pan, K. I. Winey, H. H. Hu, and R. J. Composto. Unstable polymer bilayers. 2. The effect of film thickness. *Langmuir*, 13:1758–1766, 1997.
- [85] R. M. Pasley. DLVO and hydration forces between mica surfaces in Li^+ , Na^+ , K^+ , and Cs^+ electrolyte solutions: A correlation of double-layer and hydration forces with surface cation exchange properties. *J. Colloid Interface Sci.*, 84:531, 1981.
- [86] V. N. Paunov, K. D. Danov, N. Alleborn, H. Raszillier, and F. Durst. Stability of evaporating two-layered liquid film in the presence of surfactant - iii. non-linear stability analysis. *Chem. Eng. Sci.*, 53:2839–2857, 1998.
- [87] J. R. A. Pearson. On convection cells induced by surface tension. *J. Fluid Mech.*, 4:489–500, 1958.
- [88] L. M. Pismen and Y. Pomeau. Disjoining potential and spreading of thin liquid layers in the diffuse interface model coupled to hydrodynamics. *Phys. Rev. E*, 62:2480–2492, 2000.
- [89] J. A. F. Plateau. *Statique Experimentale et Theorique des Liquides Soumis aux Seules Forces Moleculaires*. Gauthier-Villars, 1873, Paris.
- [90] I. Podariu, Z. Y. Shou, and A. Chakrabarti. Viscous flow and coarsening of microdomains in diblock copolymer thin films. *Phys. Rev. E*, 62:R3059–R3062, 2000.
- [91] A. Pototsky, M. Bestehorn, D. Merkt, and U. Thiele. Alternative pathways of dewetting for a thin liquid two-layer film. *Phys. Rev. E*, 70:025201(R), 2004.

- [92] A. Pototsky, M. Bestehorn, D. Merkt, and U. Thiele. Change of the surface morphology in the time evolution of liquid two-layer films. *J. Chem. Phys.*, 402:794, 2005.
- [93] A. Pototsky, M. Bestehorn, and U. Thiele. Control of the structuring of thin soft matter films by means of different types of external disturbance. *Physica D*, 199:138–148, 2004.
- [94] L Prandtl (1904). *Über Flüssigkeitsbewegung bei sehr kleiner Reibung*. Verh. III. Intern. Math. Kongr., Heidelberg, Teubner, Leipzig, 1905.
- [95] B. Ramaswamy, S. Chippada, and S. W. Joo. A full-scale numerical study of interfacial instabilities in thin-film flows. *J. Fluid Mech.*, 325:163–194, 1996.
- [96] N. Rehse, C. Wang, M. Hund, M. Geoghegan, R. Magerle, and G. Krausch. Stability of thin polymer films on a corrugated substrate. *Eur. Phys. J. E*, 4:69–76, 2001.
- [97] G. Reiter. Dewetting of thin polymer films. *Phys. Rev. Lett.*, 68:75–78, 1992.
- [98] G. Reiter. Unstable thin polymer films: Rupture and dewetting. *Langmuir*, 9:1344, 1993.
- [99] C. Renger, P. Müller-Buschbaum, M. Stamm, and G. Hinrichsen. Investigation and retardation of the dewetting on top of highly viscous amorphous substrates. *Macromolecules*, 33:8388–8398, 2000.
- [100] O. Reynolds. An experimental investigation of the circumstances which determine whether the motion of water shall be direct or sinuous, and of the law of resistance in parallel channels. *Phil. Trans. Roy. Soc.*, 174:935–982, 1883.
- [101] O. Reynolds. On the theory of lubrication and its application to Mr. Beauchamp Tower’s experiments, including an experimental determination of the viscosity of olive oil. *Phil. Trans. Roy. Soc.*, 177:157–234, 1886.

- [102] L. Rockford, Y. Liu, P. Mansky, T. P. Russell, M. Yoon, and S. G. J. Mochrie. Polymers on nanopericodic, heterogeneous surfaces. *Phys. Rev. Lett.*, 82:2602–2605, 1999.
- [103] E. Ruckenstein and R. K. Jain. Spontaneous rupture of thin liquid films. *J. Chem. Soc. Faraday Trans. II*, 70:132–147, 1974.
- [104] E. Schäffer and U. Steiner. Acoustic instabilities in thin polymer films. *Eur. Phys. J. E*, 8:347–351, 2002.
- [105] B. Scheid, A. Oron, P. Colinet, U. Thiele, and J. C. Legros. Nonlinear evolution of nonuniformly heated falling liquid films. *Phys. Fluids*, 14:4130–4151, 2002.
- [106] H. Schlichting. *Theory of the boundary layers*. Akademie-Verlag, 1979, Berlin.
- [107] R. Seemann, S. Herminghaus, and K. Jacobs. Dewetting patterns and molecular forces: A reconciliation. *Phys. Rev. Lett.*, 86:5534–5537, 2001.
- [108] R. Seemann, S. Herminghaus, and K. Jacobs. Gaining control of pattern formation of dewetting liquid films. *J. Phys.-Cond. Mat.*, 13:4925–4938, 2001.
- [109] M. Sferrazza, C. Xiao, R. A. L. Jones, D. G. Bucknall, J. Webster, and J. Penfold. Evidence for capillary waves at immiscible polymer/polymer interfaces. *Phys. Rev. Lett.*, 78:3693–3696, 1997.
- [110] A. Sharma. Equilibrium contact angles and film thicknesses in the apolar and polar systems: Role of intermolecular interactions in coexistence of drops with thin films. *Langmuir*, 9:3580, 1993.
- [111] A. Sharma. Relationship of thin film stability and morphology to macroscopic parameters of wetting in the apolar and polar systems. *Langmuir*, 9:861–869, 1993.
- [112] A. Sharma and R. Khanna. Pattern formation in unstable thin liquid films. *Phys. Rev. Lett.*, 81:3463–3466, 1998.

- [113] A. Sharma and R. Khanna. Pattern formation in unstable thin liquid films under the influence of antagonistic short- and long-range forces. *J. Chem. Phys.*, 110:4929–4936, 1999.
- [114] A. Sharma and G. Reiter. Instability of thin polymer films on coated substrates: Rupture, dewetting and drop formation. *J. Colloid Interface Sci.*, 178:383–399, 1996.
- [115] M. K. Smith and S. H. Davis. Instabilities of dynamic thermocapillary liquid layers. I. Convective instabilities. *J. Fluid Mech.*, 132:119–144, 1983.
- [116] A. Sommerfeld. Zur hydrodynamischen Theorie der Schmiermittelreibung. *Z. Math. Phys.*, 50:97–155, 1904.
- [117] M. J. Tan, S. G. Bankoff, and S. H. Davis. Steady thermocapillary flows of thin liquid layers. I. Theory. *Phys. Fluids A*, 2:313–321, 1990.
- [118] G. F. Teletzke, H. T. Davis, and L. E. Scriven. Wetting hydrodynamics. *Rev. Phys. Appl.*, 23:989–1007, 1988.
- [119] A. Thess and M. Bestehorn. Planform selection in Bénard-Marangoni-convection: -hexagons versus g-hexagons. *Phys. Rev. E*, 52:6358, 1995.
- [120] U. Thiele. Open questions and promising new fields in dewetting. *Eur. Phys. J. E*, 12:409–416, 2003.
- [121] U. Thiele, L. Bruschi, M. Bestehorn, and M. Bär. Modelling thin-film dewetting on structured substrates and templates: Bifurcation analysis and numerical simulations. *Eur. Phys. J. E*, 11:255–271, 2003.
- [122] U. Thiele and E. Knobloch. Front and back instability of a liquid film on a slightly inclined plate. *Phys. Fluids*, 15:892–907, 2003.
- [123] U. Thiele and E. Knobloch. Thin liquid films on a slightly inclined heated plate. *Physica D*, 190:213–248, 2004.
- [124] U. Thiele, M. Mertig, and W. Pompe. Dewetting of an evaporating thin liquid film: Heterogeneous nucleation and surface instability. *Phys. Rev. Lett.*, 80:2869–2872, 1998.

- [125] U. Thiele, K. Neuffer, M. Bestehorn, Y. Pomeau, and M. G. Velarde. Sliding drops on an inclined plane. *Colloid Surf. A*, 206:87–104, 2002.
- [126] U. Thiele, K. Neuffer, Y. Pomeau, and M. G. Velarde. On the importance of nucleation solutions for the rupture of thin liquid films. *Colloid Surf. A*, 206:135–155, 2002.
- [127] U. Thiele, M. G. Velarde, and K. Neuffer. Dewetting: Film rupture by nucleation in the spinodal regime. *Phys. Rev. Lett.*, 87:016104, 2001.
- [128] U. Thiele, M. G. Velarde, K. Neuffer, M. Bestehorn, and Y. Pomeau. Sliding drops in the diffuse interface model coupled to hydrodynamics. *Phys. Rev. E*, 64:061601, 1–12, 2001.
- [129] U. Thiele, M. G. Velarde, K. Neuffer, and Y. Pomeau. Film rupture in the diffuse interface model coupled to hydrodynamics. *Phys. Rev. E*, 64:031602, 1–14, 2001.
- [130] S. J. VanHook, M. F. Schatz, W. D. McCormick, J. B. Swift, and H. L. Swinney. Long-wavelength instability in surface-tension-driven Bénard convection. *Phys. Rev. Lett.*, 75:4397–4400, 1995.
- [131] S. J. VanHook, M. F. Schatz, J. B. Swift, W. D. McCormick, and H. L. Swinney. Long-wavelength surface-tension-driven Bénard convection: Experiment and theory. *J. Fluid Mech.*, 345:45–78, 1997.
- [132] E. J. W. Verwey and J. Th. G. Overbeck. *Theory of the Stability of Lyophilic Colloids*. Elsevier, Amsterdam, 1948.
- [133] M. B. Williams and S. H. Davis. Nonlinear theory of film rupture. *J. Colloid Interface Sci.*, 90:220–228, 1982.
- [134] O. Wunnicke, P. Müller-Buschbaum, M. Wolkenhauer, C. Lorenz-Haas, R. Cubitt, V. Leiner, and M. Stamm. Stabilization of thin polymeric bilayer films on top of semiconductor surfaces. *Langmuir*, 19:8511–8520, 2003.
- [135] S. G. Yiantsios and B. G. Higgins. Rayleigh-Taylor instability in thin viscous films. *Phys. Fluids A*, 1:1484–1501, Sept. 1989.

-
- [136] S. G. Yiantsios and B. G. Higgins. Rupture of thin films: Nonlinear stability analysis. *J. Colloid Interface Sci.*, 147:341–350, 1991.
- [137] Y. L. Zhang, O. K. Matar, and R. V. Craster. Analysis of tear film rupture: effect of non-Newtonian rheology. *J. Colloid Interface Sci.*, 262:130–148, 2003.

Appendix A

Thermocapillary terms in nonisothermal liquid films

Here we specify the thermocapillary part of Eqs. (5.19) and Eq. (4.1) for the case of non-isothermal films. For generality we consider the case of two-layer films and then simplify the obtained results for one-layer films.

We rewrite the derivatives $\partial_x \sigma_{12}$ and $\partial_x \sigma_2$ in terms of the gradients of the local thicknesses $\partial_x h_i$. In the long-wave approximation [80] the temperature field is in both layers a linear function of the vertical coordinate z , i.e. $T_i = a_i z + b_i$. To determine the coefficients we consider a three-layer geometry (Fig. A.1), i.e. we take into account the heat conduction in a gas layer of finite thickness $d_g = d_t - d_2$, where d_t is the distance between the substrate and an upper plate. The temperature in the gas layer is $T_g = a_g z + b_g$. The boundary conditions at both interfaces are continuity of the temperature field and continuity of the heat flux $\kappa_i \partial_z T_i = \kappa_k \partial_z T_k$, where κ_i is the thermal conductivity of the i -th layer. The temperatures at the substrate T_0 and at the upper plate T_t are constant. The coefficients a_i and b_i depend on the local thicknesses h_i and are given by

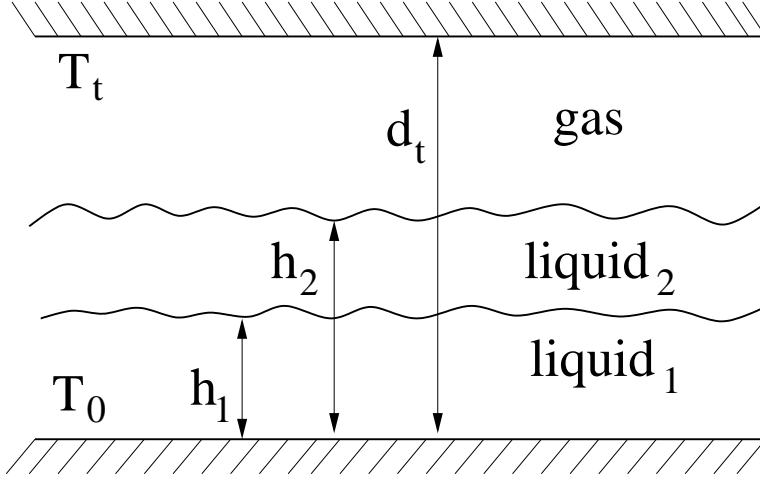


Figure A.1: Sketch of the system with a gas layer of finite thickness.

$$a_g = \frac{\alpha \Delta T}{d_t - h_2 + \frac{\kappa_g}{\kappa_1} h_1 + \frac{\kappa_g}{\kappa_2} (h_2 - h_1)}$$

$$a_2 = \frac{a_g \kappa_g}{\kappa_2}, \quad a_1 = \frac{a_g \kappa_g}{\kappa_1}$$

$$b_1 = T_0, \quad b_g = T_t - a_g d_t$$

$$b_2 = a_g \kappa_g h_1 \left(\frac{1}{\kappa_1} - \frac{1}{\kappa_2} \right) + T_0,$$

where $\Delta T = T_0 - T_2$ and

$$\alpha = \frac{d_2 - d_t - \kappa_g h_1 / \kappa_1 - \kappa_g (d_2 - d_1) / \kappa_2}{-\kappa_g h_1 / \kappa_1 - \kappa_g (d_2 - d_1) / \kappa_2}.$$

Here T_2 is the temperature of the liquid-gas interface, when both interfaces are undeformed, i.e. for $h_i = d_i$. The above formulas allow to determine the derivatives

$$\partial_x \sigma_{12} = \Gamma_{11} \partial_x h_1 + \Gamma_{12} \partial_x h_2 \quad (\text{A.1})$$

$$\partial_x \sigma_2 = \Gamma_{21} \partial_x h_1 + \Gamma_{22} \partial_x h_2,$$

where the matrix $\mathbf{\Gamma}$ is determined as follows

$$\mathbf{\Gamma} = a \begin{pmatrix} \frac{\kappa_g}{\kappa_1} \frac{d\sigma_1}{dT} b & -\frac{\kappa_g}{\kappa_1} \frac{d\sigma_1}{dT} h_1 \left(\frac{\kappa_g}{\kappa_2} - 1 \right) \\ \frac{d\sigma_2}{dT} \left(bc - \frac{\kappa_g}{\kappa_2} h_2 b \right) & \frac{d\sigma_2}{dT} \left\{ \frac{\kappa_g}{\kappa_2} (d_t + h_1 b) - b h_1 \left(\frac{\kappa_g}{\kappa_2} - 1 \right) \right\} \end{pmatrix}. \quad (\text{A.2})$$

Here $a = (\alpha \Delta T) / \left[d_t - h_2 + \frac{\kappa_g}{\kappa_1} h_1 + \frac{\kappa_g}{\kappa_2} (h_2 - h_1) \right]^2$, $b = \kappa_g (1/\kappa_1 - 1/\kappa_2)$ and $c = \left\{ d_t - h_2 \left(1 - \frac{\kappa_g}{\kappa_2} \right) \right\}$. For the linear normal Marangoni effect $d\sigma_{12}/dT$ and $d\sigma_2/dT$ are negative and constant. The Eqs. (A.2) are used in Eqs. (5.19) to obtain a closed system of equations for h_1 and h_2 .

Using above results one can now obtain the dependence of $\partial_x \sigma_2$ on h and on $\partial_x h$ for the case of one-layer films. For this purpose one makes the following simplifications: (i) the liquid-liquid interface is not deformed, so that $h_1 = d_1$, (ii) the thermal properties of both liquids are equal: $\kappa_1 = \kappa_2$. Further on, the thickness of the gas layer $d_t - d_2$ is considered to be much larger than d_2 . Accounting for all these simplifications, the local temperature of the liquid-gas interface T_h becomes

$$T_h = -\frac{(1+B)\Delta T}{(d_2 + B h_2)} h_2 + T_0,$$

where $B = \kappa_g d_2 / (\kappa_2 d_t)$ is the Biot number and d_t can be seen as the thickness of the gas layer d_g : $d_g = d_t - d_2 \sim d_t$.

Thus, the shear stress term $\partial_x \sigma_2$ reads

$$\partial_x \sigma_2 = \frac{d\sigma_2}{dT} \frac{(1+B)\Delta T d_2}{(d_2 + B h_2)^2} \partial_x h_2$$

After substituting σ_2 with σ , h_2 with h and d_2 with d , the term $\partial_x \sigma$ is used in the one-layer equation (4.1).

Acknowledgments

First of all I thank Michael Bestehorn who accepted me without hesitating as a PhD student at his chair and created a very pleasant and friendly working atmosphere. I also thank him because under his supervision I started working on non-linear dynamics and pattern formation, where I probably will stay in for the rest of my life.

I thank Uwe Thiele for the critical discussions throughout the period of our collaboration, for his constructive approach to every single question that arose during the preparation of our common papers and for the critical reading of this thesis.

I also thank Alexander Golovin for helpful discussions of the physical concepts of the two-layer film dynamics, for inviting me to participate in the workshop on Self-Assembly, he organized in France in August 2004 and for his agreement to be one of my referees.

My special thank goes to my colleague Domnic Merkt, who helped me to understand the principles of numerical simulations and for his attendance to debate not only on physics.

I also thank my colleagues Rodica and Ion Borcia, Michaela Enculescu, Katrin Gregor, Falk Günther, Martin Ohlrich, Paul and Roxana Racec, Dieter Robaschik, Götz Seibold, Sergej and Olga Varlamov, Ulrich Wulf for their friendship and readiness to help.

I am very grateful to all my friends who make it clear that world consists not only of work and research.

Last but not least I thank my very close friend Nadiya Kosytsina for her everyday's support and understanding, for sincereness and her joie de vivre.